UNIVERSITA' DEGLI STUDI DI PADOVA

Dipartimento di Ingegneria Industriale DII

Dipartimento di Tecnica e Gestione dei Sistemi Industriali

Corso di Laurea in Ingegneria Meccanica

MECHANICAL BEHAVIOR OF GAS METAL ARC AA6082-T6 WELDMENTS

Relatore

Ch.mo Prof. Paolo Ferro

Ch.mo Prof. Filippo Berto

Francesco Leoni 1141301

Anno Accademico 2017/2018

1 Abstract

The purpose of this work is to determine the mechanical properties of AA6082-T6 plates which have been welded with the Gas Metal Arc technique, which is one of the most common welding technology used in industrial applications. To determine the mechanical properties some tests have been carried out: hardness Vickers test, bend test, tensile test, fatigue test, Charpy V-notch test. In addition, both optical microstructure analysis of the weld and scanning electron microscope examination of selected fracture surfaces have been carried out. The tests have been carried out in both longitudinal and transversal direction with respect to the welding direction.

From the tests carried out it is concluded that HAZ softening is the main problem in the GMA weldments. This brings to a reduction in strength equal to 44% with respect to the parent material. The softening can be observed both in the tensile and hardness test. In the tensile test, it has been observed that the yield strength of the welded specimens is much lower compared to the parent material one (both considering the longitudinal and the transverse direction). In the hardness test it has been observed the hardness profile along the plate section. It has been noticed that there is a minimum value of hardness in the heat affected zone, that correspond to the weakest part of the component. This has been proved with the tensile test: all the welded tensile specimens broke in the HAZ approximately at the same distance where the least hard point has been measured in the hardness test. From the Charpy V-notch impact test it has been observed that the specimens tested in the HAZ have the greatest energy absorption capacity. This result gives an indication of the ductility of the material, that has been also observed in the bend test. The bend test results give an indication of the quality of the welding. From this test it is concluded that the quality of the weld is high: no crack was detected during the bend. From the micrography carried out with the confocal microscope it has been measured the porosity ratio of the weld. Pores are present, but with a low density: much lower than the 3% given as an indication of the maximum value for this kind of welding technology.

Sommario

L’obiettivo di questo lavoro di tesi è la determinazione delle proprietà meccaniche di componenti di alluminio del tipo AA6082-T6 saldati mediante la tecnologia GMA. Questo tipo di saldatura è uno dei più usati e diffusi nel campo della saldatura di componenti in alluminio a livello industriale. Per determinare le caratteristiche meccaniche conseguenti a questo tipo di saldatura, sono stati preparati provini a partire da piastre saldate e non, sui quali sono stati effettuati diversi tipi di test. I test condotti sono: test di durezza Vickers, prova di piegatura, test di trazione, test di fatica, test di impatto Charpy. Oltre a questi, è stato osservato il materiale al microscopio, sia usando il microscopio ottico per la metallografia della saldatura, sia al microscopio SEM per osservare alcune superfici di frattura di campioni selezionati dai vari test.

Dai test condotti, è stato osservato che uno dei maggiori svantaggi che questa tecnologia comporta è la perdita di resistenza a causa dell’alterazione termica dovuta alle alte temperature raggiunte durante l’apporto del materiale fuso. A causa dell’elevata conducibilità termica dell’alluminio la perdita di caratteristiche meccaniche riguarda un’ampia zona nell’intorno della saldatura. La perdita di resistenza è stata osservata sia nel test di trazione, nel quale tutti i provini saldati si sono rotti nella ZTA, sia nel test di durezza, in cui è stato osservato che il profilo di durezza presenta un minimo appunto in questa zona. Dal test di impatto Charpy, sono stati misurati i valori di energia che il materiale è in grado di assorbire. È stato osservato che il maggior assorbimento avviene da parte dei provini provenienti dalla ZTA. La prova di piegatura è utile per osservare la qualità della saldatura: in generale, se il provino piegato resiste al test, significa che la saldatura è buona e non presenta difetti che ne compromettono l’utilizzo. Nel caso in esame, i provini testati hanno resistito al test senza la comparsa di cricche superficiali apprezzabili. Il test di fatica ha permesso di osservarne il comportamento sotto l’effetto di un carico ciclico. Dai risultati ottenuti si sono potuti costruire i relativi diagrammi S-N, permettendo un confronto con quanto trovato in letteratura. In aggiunta è stata osservata una sezione della saldatura, dalla quale è stata misurata la percentuale di area ricoperta da porosità. Anche da quest’ultima prova si è concluso che la saldatura rispetta le caratteristiche di qualità indicate dagli standard.

Ringraziamenti

Il primo ringraziamento va ai miei genitori, che mi hanno sempre sostenuto e accompagnato nelle mie scelte, rendendo possibile tutto il mio percorso, di vita e di studi. Un grazie di cuore va ai miei amici Giovanni, Francesco e Matteo, con cui ho condiviso ogni singola gioia e dolore negli ultimi cinque anni. Ringrazio il mio amico Luca, che nonostante la distanza mi è sempre stato vicino e aiutato in ogni momento, dandomi la consapevolezza di avere sempre e comunque una persona su cui contare. Ringrazio Diletta per avermi sempre sostenuto. Ringrazio i coinquilini e casa Cavasin, in particolare Marco V. e Marco A., che mi hanno regalato un sacco di risate. Ringrazio anche Martina, Sara, Davide, Luca e Alessio. Ringrazio Matteo, Pietro e Alberto, con cui ho avuto la fortuna di condividere questi ultimi mesi in Norvegia.

Ringrazio particolarmente il Professor Filippo Berto per la disponibilità e saggezza dimostrata nel guidarmi durante il mio lavoro di tesi e per la sua grande umanità. Ringrazio Lise, che mi ha guidato con pazienza nella realizzazione del presente lavoro. Ringrazio Magnus e Borge per la compagnia e l'aiuto che mi hanno dato durante le ore spese in laboratorio. Ringrazio il Professor Paolo Ferro per la disponibilità dimostratami.

Ringrazio inoltre tutte le persone con cui ho avuto modo di condividere momenti di crescita.

Contents

2 List of Figures

3 List of Tables

1 Introduction

Aluminum became one of the most popular materials among builders, engineers and designers for many reasons during the last century. At the beginning of ‘900s aluminum was unused in civil engineering, as the metal was too expensive and not produced in large volumes. In 1920s electrolysis process reduces the cost of Aluminum by 80%. Aluminum offers a combination of valuable properties as it’s one of the lightest metals in the world: it’s almost three times lighter than iron but it’s also very strong, extremely flexible and corrosion resistant because its surface is always covered by an extremely thin and very strong layer of oxide film. Thanks to its specific weight, aluminum structures can be a half or two-thirds the weight of steel structures. The mechanical properties of aluminum can also be improved by adding elements such as magnesium (Mg) and silicon (Si). The addition of these alloying elements increases the aluminum response to heat treatment due to formation of Mg_2Si intermetallic compounds. [1] The improved properties make them more attractive, especially within the transport, as automotive and aerospace industries, because they provide good strength and toughness in engineering applications, while maintaining the low density: it has been calculated that each kilogram of weight costs from three to six dollars considering a family car, from a hundred to five hundred dollars for a civil aircraft and from three thousand to ten thousand dollars considering space vehicle [2].

Serious attention to weight savings in motor vehicles started in the 1970s following steep increases in oil price, more recently impetus has come from legislation in some countries to reduce levels of exhaust emissions through improved fuel economies. In this regard, each 10% reduction in weight is said to correspond to a decrease of 5.5% in fuel consumption. Moreover, each kg of weight saved is estimated to lower CO2 emissions by some 20 kg for a vehicle covering 170 000 km. The two strategies to save weight have been to build smaller vehicles (so-called downsizing) and to use lighter materials (light-weighting).

Material and fabricating costs need to be minimized and the main property requirements for the sheet are:

- sufficient strength for structural stability, fatigue resistance, dent resistance and crash worthiness
- good formability for stretching, bending and deep drawing, as well as the ability to control anisotropy and spring back
- good surface appearance, e.g. freedom from Lüders bands.
- easy joining by welding, clinching, riveting, brazing and adhesive bonding
- high corrosion resistance
- ease of recycling

An optimum combination of strength and formability requires careful control of alloy composition, working and heat treatment. [3]. The Al-Mg-Si alloys (6xxx series) we are going to consider in this work are not as strong as 2xxx and 7xxx alloys, but have good formability, weldability, machinability, and corrosion resistance, with medium strength. Alloys in this heat-treatable group may be formed in T4 temper and strengthened after forming to full T6 properties by precipitation heat treatment [4].

Many aluminum products involve the use of welding. The main characteristics of aluminum, which influence welding, are hydrogen solubility, aluminum oxides, thermal conductivity, thermal expansion and the solidification shrinkage, and non-discolouration. It is a lack of understanding in the cleaning aspect that has kept many fabricators away from the welding of aluminum. As hydrogen is extremely soluble in molten aluminum, when the weld freezes, the hydrogen can get trapped in the weld itself. That is the main source of porosity in aluminum welds [5]. The most common welding technique for aluminum alloys is gas-metal arc welding (GMAW), which offers advantages of high quality welds, high welding speeds and the possibility to be robotized. Even if many improvements have been made in the performance of this process there are many problems associated with fusion welding of the age hardening aluminum alloys. The high coefficient of thermal expansion and solidification shrinkage, combined with a relatively wide solidification-temperature range, makes these alloys susceptible to weld cracking mechanisms like solidification cracking and liquation cracking [6].

It is important to characterize the mechanical properties of the joints obtained by welding process to understand the behavior of them when used in structural application. From this reason comes the general purpose of the present report: obtain a better understanding of the mechanical properties of alloy AA 6082-T6 subsequent to the gas metal arc welding. To obtain a complete overview of the mechanical properties, hardness, bending, tensile, Charpy V-notch, fatigue testing has been carried out. The microstructure of the weldments is studied by optical microscope.

2 Theory

In this chapter an introduction to aluminum and to the properties of extruded and artificially aged Al-Mg-Si alloys is provided. A review on welding of these alloys with respect to GMAW and a short presentation of the different zones in a welded component will be also done.

2.1 Aluminum

Aluminum is a silvery-white metal, the 13th element in the periodic table. One surprising fact about aluminum is that it's the most widespread metal on Earth, making up more than 8% of the Earth's core mass. It's also the third most common chemical element on our planet after oxygen and silicon. At the same time, because it easily binds with other elements, pure aluminum does not occur in nature. This is the reason that people learned about it relatively recently. Common mineral, bauxite, is used today as the primary raw material in aluminum production. Bauxite is a clay mineral comprising various modifications of aluminum hydroxide mixed with iron, silicon, titanium, sulfur, gallium, chromium, vanadium oxides, as well as sulfuric calcium, iron and magnesium carbonates. On average 4-5 ton of bauxite are needed to produce 1 ton of aluminum. In the first stage of aluminum production bauxite is processed into alumina, or aluminum oxide Al_2O_3. Alumina looks like white powder and it is then processed into aluminum at aluminum smelters using electrolytic reduction. Aluminum offers a rare combination of valuable properties. It is one of the lightest metals in the world: it's almost three times lighter than iron but it's also very strong, extremely flexible and corrosion resistant because its surface is always covered in an extremely thin and yet very strong layer of oxide film. It doesn't magnetize, it's a great electricity conductor and forms alloys with practically all other metals. There is another property that is just as significant: aluminum can be reused repeatedly. Both aluminum and its alloys can be melted down and reused without any detriment to its mechanical properties. Scientists have estimated that 1 kg of recycled aluminum cans can save up to 8 kg of bauxite, 4 kg of various fluorides and up to 15 KWH of electricity.
About 75% of aluminum produced in the time that the aluminum industry has existed is still in use today. [7]. The life cycle of aluminum is shown in Figure 2.1.

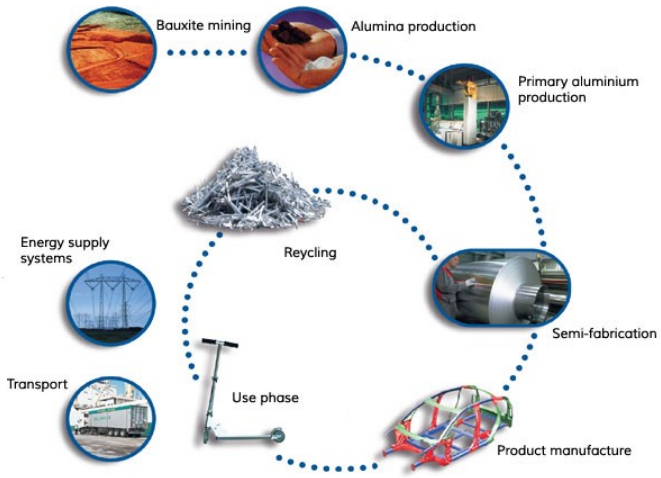

Figure 2.1: Life cycle of aluminum, from bauxite mining to recycling [8].

2.1.1 Aluminum Alloy Categories

It is convenient to divide aluminum alloys into two major categories: wrought compositions and cast compositions. Many alloys respond to thermal treatment based on phase solubility. These treatments include solution heat treatment, quenching, and precipitation, or age, hardening. Cast and wrought alloy nomenclatures have been developed. The Aluminum Association system employs different nomenclatures for wrought and cast alloys but divides alloys into families for simplification. For wrought alloys a four-digit system is used to produce a list of wrought composition families as follows:

- 1xxx: Controlled unalloyed (pure) composition, used primarily in the electrical and chemical industries. The main applications are: packaging and foil, roofing, cladding, low-strength corrosion resistant vessels and tanks.
- 2xxx: Alloys in which copper is the principal alloying element, although other elements, notably magnesium, may be specified. 2xxx-series alloys are widely used in aircraft where their high strength (yield strengths as high as 455 MPa) is valued. The main applications are: highly stressed parts, aerospace structural items, heavy duty forgings, heavy goods vehicle wheels, cylinder heads, pistons.
- 3xxx: Alloys in which manganese is the principal alloying element, used as general-purpose alloys for architectural applications and various products. The main applications are: packaging, roofing and cladding, chemical drums and tanks, process and food handling equipment.

- 4xxx: Alloys in which silicon is the principal alloying element, used in welding rods and brazing sheet. The main applications are: filler metals, cylinder heads, engine blocks, valve bodies, architectural purposes
- 5xxx: Alloys in which magnesium is the principal alloying element, used in boat hulls, gangplanks, and other products exposed to marine environments. The main applications are: cladding, vessel hulls and superstructures, structural members, vessels and tanks, vehicles, rolling stock, architectural purposes
- **6xxx**: Alloys in which magnesium and silicon are the principal alloying elements, commonly used for architectural extrusions and auto-motive components. The main applications are: high-strength structural members, vehicles, rolling stock, marine applications, architectural applications.
- 7xxx: Alloys in which zinc is the principal alloying element (although other elements, such as copper, magnesium, chromium, and zirconium, may be specified), used in aircraft structural components and other high-strength applications. The 7xxx series are the strongest aluminum alloys, with yield strengths ≥500 MPa possible. The main applications are: high strength structural members, heavy section aircraft forgings, military bridging, armour plate, heavy goods vehicle and rolling stock extrusions.
- 8xxx: Alloys characterizing miscellaneous compositions. The 8xxx series alloys may contain appreciable amounts of tin, lithium, and/or iron.
- 9xxx: Reserved for future use [4]

The effects of the alloying element on the mechanical properties are summarized in Figure 2.1.

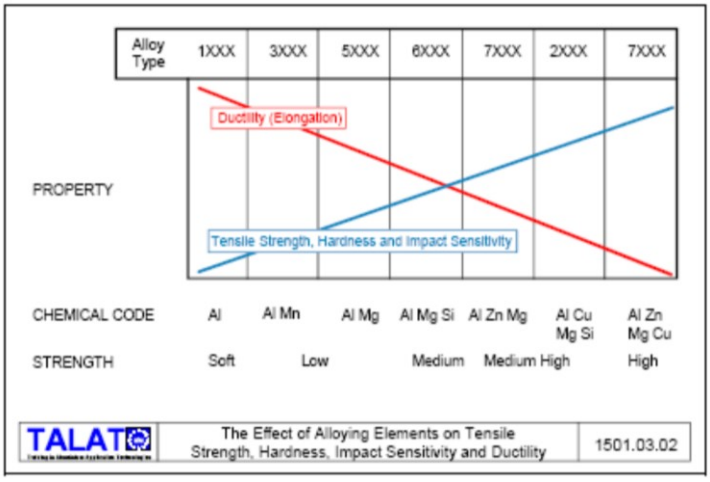

Figure 2.1 Mechanical properties of wrought composition families. [9]

A list of the main alloying elements effects is presented in Table 2.1.

Table 2.1: General effect of several alloying elements in AlMgSi-alloys.

Si	Gives good castability, abrasion resistance, reduces thermal expansion coefficient.
Mg	Increases strength and hardness. Gives good corrosion resistance, increases weldability.
Mn	Increases Yield and Ultimate tensile strength. Improves low-cycle fatigue resistance. Gives corrosion resistance.
Cr	Grain refiner, inhibits recrystallization.
Zn	Increases strength and hardness. Gives heat treatable alloys when combined with Mg.
Fe	Contamination.
Cu	Increases strength and hardness. Reduces corrosion resistance.

The Aluminum alloy we are going to consider in this work is the 6082-T6.

2.1.1.1 Al-Mg-Si Alloys

Alloys in the 6xxx series contain silicon and magnesium approximately in the proportions required for formation of magnesium silicide (Mg_2Si), thus making them heat treatable. The main alloying elements, Mg and Si, have a significant solid solubility in aluminum. And as shown in Figure 2.2, the solubility increases with increasing temperature.

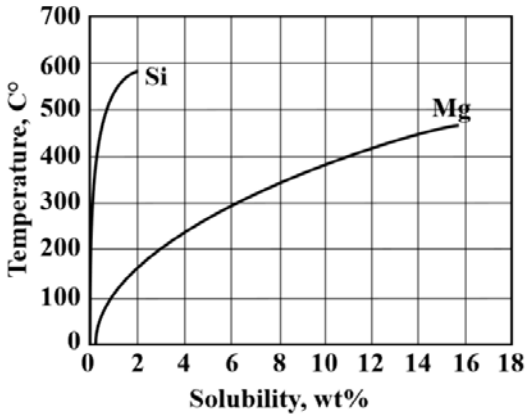

Figure 2.2: Equilibrium binary solid solubility of Mg and Si in aluminium as a function of temperature. [6]

Although not as strong as most 2xxx and 7xxx alloys, 6xxx series alloys have good formability, weldability, machinability, and corrosion resistance, with medium strength. Alloys in this heat-treatable group may be formed in the T4 temper (solution heat treated but not precipitation heat treated) and strengthened after forming to full T6 properties by precipitation heat treatment [4]. The 6xxx-series aluminum alloys are the most widely used alloys in extrusion. Some of the mechanical properties are presented in Table 2.2.

Table 2.2: General mechanical properties for AlMgSi-alloys [10].

Mechanical properties for AlMgSi-alloys	
Yield strength (σ_y)	190-360 MPa
Tensile strength (σ_u)	220-390 MPa
Elongation	17-12%

In general, the 6xxx series alloys are suitable for components that should resist in a strongly corrosive environment: tubular, extruded, structural components. The high mechanical properties of the alloy are due to the formation of precipitates, favored by the T6 heat treatment (Figure 2.3). This heat treatment consists in solubilization at 530°C, air-quenching and aging of the alloy at 175 °C for 8 hours. The complete treatment gives to the alloy an average grain size about 30-40 mm. The excess alloy elements in the solid solution after hardening form precipitates during aging according to the β "-β '-β-Mg_2Si sequence.

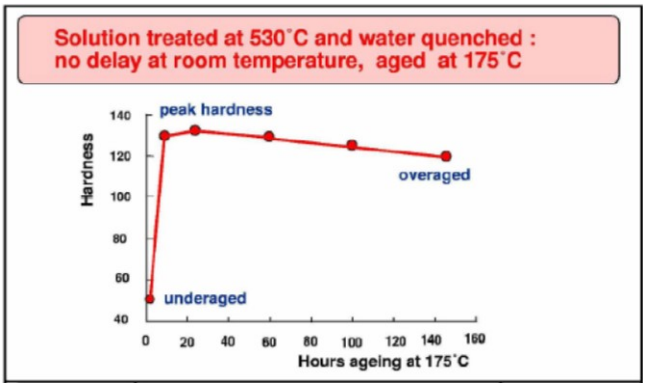

Figure 2.3: Ageing hardening. [9]

In the AlMgSi system, several types of precipitates were observed, depending on the content of alloying elements, on the temperature and period of aging. The distribution of the precipitates in the matrix of Al is homogeneous, there are two types of precipitates, acicular shaped and stick-shaped.

During aging the precipitates increase and the mechanical resistance of the material increases with the increasing of the number and size of precipitates. The resistance reaches a maximum, and a subsequent aging produces coalescence of the precipitates with consequent decrease of the mechanical characteristics.

In the 6xxx alloys a very low level of precipitates produces a fast progression of aging and nucleation and growth of rods of Mg_2Si.

Many alloys exhibit changes in properties even at room temperature after quenching. This phenomenon, called natural aging, can start immediately after hardening or after an incubation period (one or more days). You can speed up the precipitation and changing the mechanical properties by heating these alloys at a higher temperature. This operation is called artificial aging. In some cases, a considerable increase in toughness can be achieved by cold working after quenching. Better results can be achieved with heat treatment after cold working.

The effect of precipitation on mechanical properties is even higher if the material is further processed at a temperature between 95 ° C and 200 ° C. The effects are not only due to the different speeds at which reactions occur, but also to different structural changes. For example, the yield limit increases more than the breaking limit, hardness and ductility decrease. Thus, a hardened T6 alloy is harder, but less ductile than a T4.

Over aging decreases both yield and rupture points, but ductility does not change proportionally. On the other hand, over aging can positively affect other factors. In some cases, over aging increases the "corrosion-stress" properties thanks to greater dimensional stability created in the over aging.

2.1.2 Processing and thermal history of aluminum.

Processing of the primary aluminum includes casting, homogenization, extrusion and artificial ageing. A scheme of the thermal history of these steps is shown in Figure 2.4.

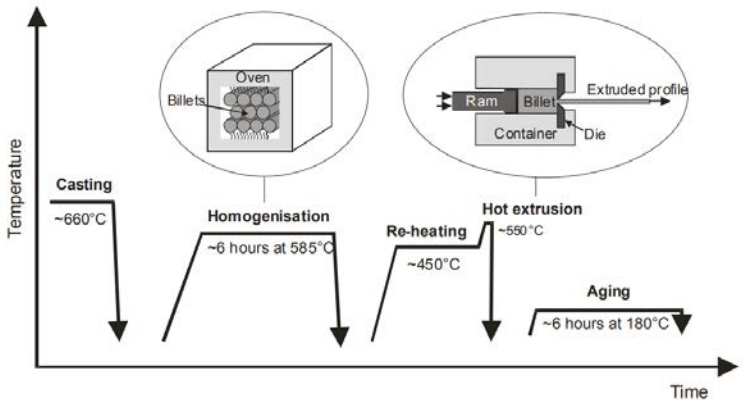

Figure 2.4: Thermal history of AlMgSi aluminum alloy. Copied from [11]

Before the extrusion process, Mg and Si are added in the melt together with eventually others alloying elements. The main alloying elements are partly dissolved in the primary α-Al matrix, and partly present in the form of intermetallic phases. The relationship between these alloying elements, as shown in Figure 2.5, has a large influence on the amount of Mg_2Si formed during the solidification process.

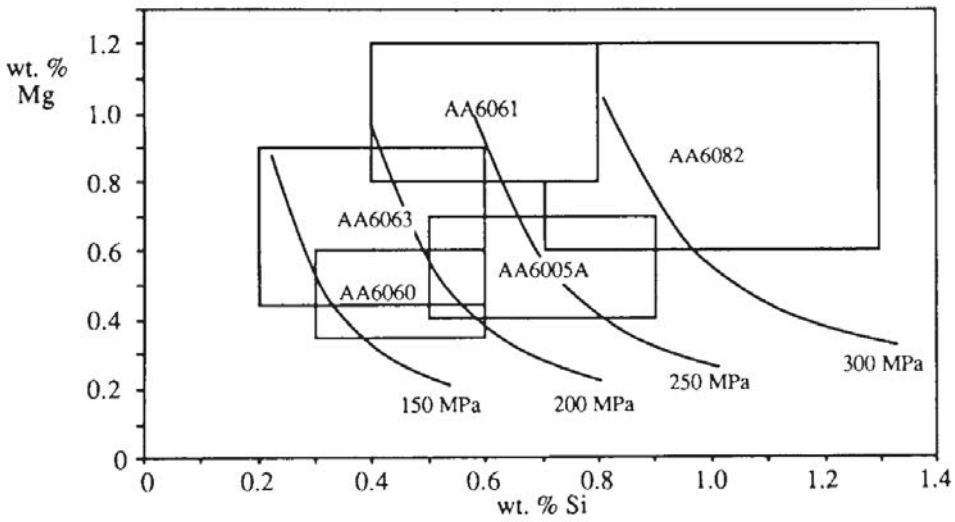

Figure 2.5: The compositional limits of some common 6xxx alloys, together with contours representing common peak aged (T6) values of yield strength [3].

The amounts of alloying elements also influence the mechanical properties of the metal. Fe is present as an impurity in all commercial alloys and forms a variety of Al–Fe and Al–Fe–Si intermetallic phases during solidification. Any Si which is not incorporated in the α-Al matrix or the Al–Fe–Si intermetallic phases combines with Mg to form Mg_2Si at a later stage in the solidification process. The type, size, morphology and distribution of the intermetallic particles are very important in determining the subsequent material properties. The nature of the intermetallic particle population in the final product will be determined not only by the as-cast state, but also by subsequent ingot homogenization and thermomechanical processing [12].

2.1.3 Structural modifications of aluminum alloys

Aluminum would have very limited structural uses if it was not possible to obtain its alloys. Through the addition of elements like Cu, Si, Mg, Mn, improvements, with respect to pure metal, in the mechanical, physical and technological properties are possible.

The cooling speed, during solidification, acts directly on the coalescence of the constituents and determines the occurrence or absence of any secondary reactions between solidified crystals and surrounding liquid.

The cooling speed of the solid-state alloy has crucial importance in relation to the phenomenon of supersaturation of the solution.

The structure of an alloy is susceptible to modifications, as known, also through appropriate deformations in the plastic field. For alloys in general and for those of aluminum, it is possible to affirm that the structural characteristics (and therefore the mechanical, physical properties, etc.) are linked to the chemical composition of the alloy (alloying element and its percentage), from which depend structural balances, and the possible modifications of these balances.

The modification of equilibrium state, as seen above, can be obtained acting on the liquid or on the solid state: the following modes of structural modification are possible:

Acting on the liquid:

- Modification treatments;

Acting on the solid:

- mechanically (plastic processing);

-thermally (heat treatments).

For the modification treatments, the increase of the cooling speed of a cast, is responsible for a refinement of the structure, as it determines the formation of a greater number of crystallization germs and, consequently, lesser growth of these. This causes improvements in mechanical properties. The increase in the speed of cooling can be achieved with shell casting instead of mold casting, which ensures a faster thermal dispersion, or by the introduction of elements (Strontium and Antimony for example), that are able to modify the crystalline structure of the alloy. The structural modifications of greater interest are however obtained on the solid state (mechanically and thermally).

2.1.3.1 Hardening mechanisms

The plastic deformation of metals begins when the stress is higher than the yield one. Block or slow down the movement of the metals dislocations is the way to have a harder material. Dislocations are a type of defect in crystals. Dislocations are areas were the atoms are out of position in the crystal structure (Figure 2.6). Dislocations are generated and move when a stress is applied. The motion of dislocations allows slip – plastic deformation with a much lower effort than what would be necessary if the lattice was perfect.

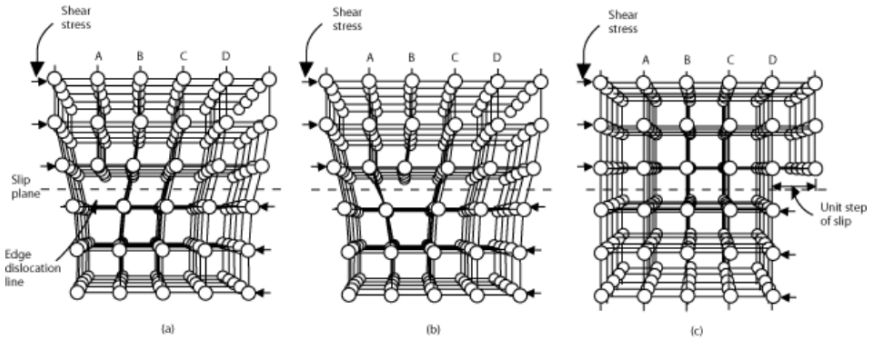

Figure 2.6: Dislocation movement mechanism.

There are many strengthening mechanisms that can be applied to the aluminum alloys. These are:

1) Grain size control
2) Work hardening
3) Dispersion hardening
4) Precipitation of secondary phases
5) Solid solution hardening
6) Precipitation hardening

These hardening processes are effective because they produce conditions that impede the movement of dislocations. Dislocations are faults that enable metal crystals to slip at stresses very much below those that would be required to move two perfect crystal planes past one another.

2.1.3.1.1 Grain size control

A metal is not usually made up of a single large crystal, but of many small crystals called grains, consisting in lattices each having a different orientation from the adjacent one. The formation of the grains begins during the solidification of the material: this last phase influences the characteristics of the grains, in terms of size and quantity. The interfaces between the different crystalline lattices are called grain boundary (Figure 2.7).

The size and the orientation of the grains determine some mechanical properties of the material: the grain boundaries obstruct the plastic deformation, since the dislocations are strongly blocked in their movement near the interfaces. Their effect is greater the more the crystalline lattice orientation from one grain to another is different. Considering these reasons is easy to understand as a material with fine grains have a higher mechanical strength than

coarse grains one; the reduction of the grain size is an important hardening mechanism of the metal.

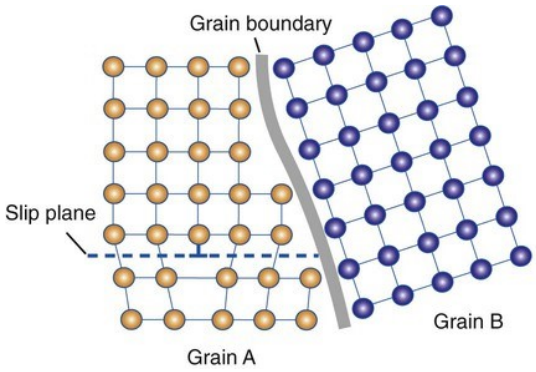

Figure 2.7: Effect of the grain boundary on the dislocation movement

The mathematical model representing this mechanism can be described with the Hall-Petch equation which shows how, at temperatures lower than the recrystallization one, a fine-grained metal is stronger than a coarse-grained one:

$$\sigma_s = \sigma_0 + \frac{k}{\sqrt{d}}$$

σ_s: yield strength
σ_0, k: constants characteristic of the material
d: average size of the crystalline grains.

The following graph shows the grain size effect on the yield strength based on the Hall-Petch model (Figure 2.8).

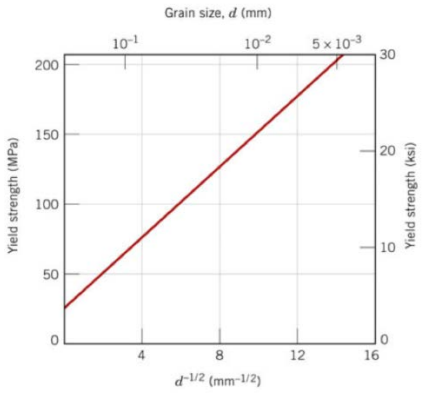

Figure 2.8: Hall-Petch equation. Grain size effect on the Yield strength.

2.1.3.1.2 Work hardening

Aluminum products obtained by rolling processes, extrusion, bending, drawing, etc. are subjected to a mechanical manufacturing process. When the process is performed below the recrystallization temperature (cold work), there is an increase in the strength due to the dislocations which, increasing in number and sliding on different planes, cause a "traffic jam" that block each other, and prevent any movement. In Figure 2.9 is possible to see the different structure of the material before and after the plastic deformations that induce dislocations.

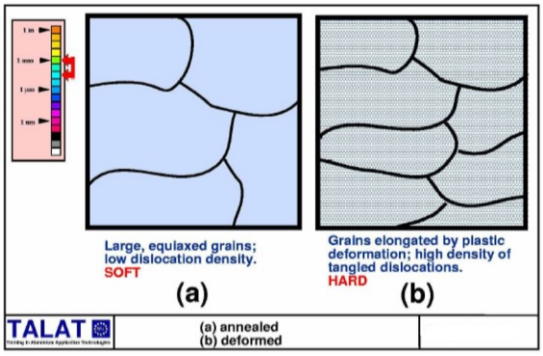

Figure 2.9: Structure of the material before and after cold work.

Fabricating processes carried out above the metal's recrystallization temperature (hot work) do not normally increase strength over the annealed strength condition. With non-heat-treatable wrought alloys, cold work is the only way of increasing strength. With heat treatable alloy, cold work applied after heat treating can increase strength still further. In Figure 2.10 is shown the aluminum structure at a temperature of 250 ° C, and the polygonal shaped structure that dislocations form. If the temperature of the piece is high, new stress arise between the crystals, and the real recrystallization takes place. Softening of the metal starts. This process continues until all the material is softened.

If the recrystallization is obtained at high temperatures for a long time, grains grow with a regular shape.

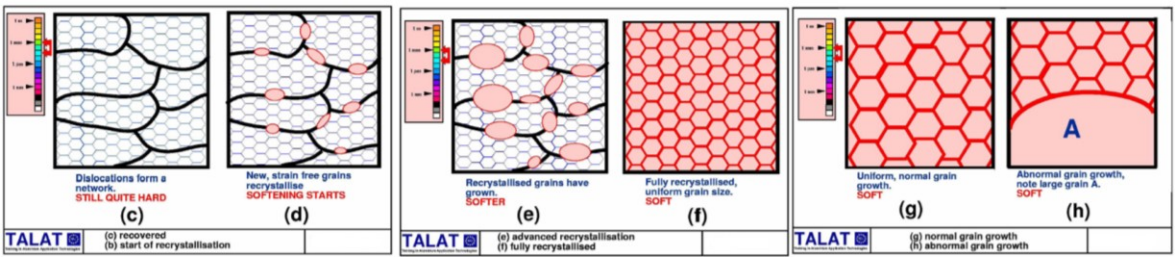

Figure 2.10: High temperature recrystallization, softening process and grain growth.

2.1.3.1.3 Dispersion hardening

Small particles of insoluble material are uniformly distributed within the crystal lattice, in such a way to block the movement of dislocations. For aluminum this kind of hardening can be carried out according to two mechanisms:

- By adding alloying elements that chemically combine with the base metal or between them, forming fine particles that precipitate in the lattice.
- By mixing particles of appropriate substances with aluminum powder, compacting the mixture into a solid mass.

2.1.3.1.4 Second phases precipitation

When the phase diagram (Figure 2.11) of an alloy has a zone of solubility which decreases highly with the temperature there are the conditions for a possible aging. The classic example is series 2000 alloy which contain about the 4% of copper.

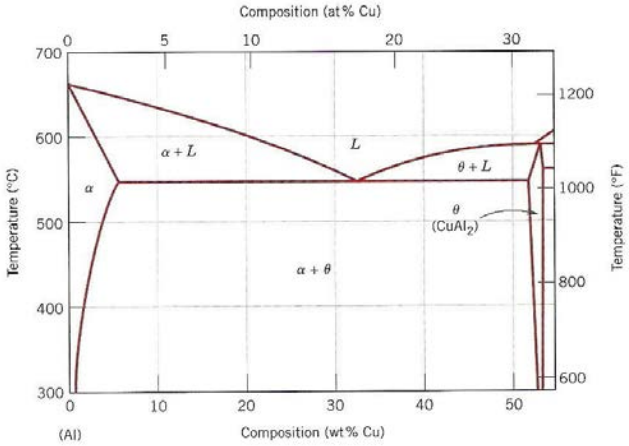

Figure 2.11 Al-Cu phase diagram [9]

Between 500°C and 580°C copper dissolves in aluminum and the alloy is monophasic, however, by cooling, the copper forms the $CuAl_2$ compound. If it cools slowly (Figure 2.12-a) the speed of nucleation of $CuAl_2$ is low, the growth rate is high and then few precipitates on the edges of the grains are formed (the dislocations are able to move easily between them). If the cooling speed is high (Figure 2.12-b) the nucleation speed of $CuAl_2$ is high, the growth rate is low so that many precipitates (not only on the grain boundaries) are formed. In this case the movement of the dislocations is more difficult.

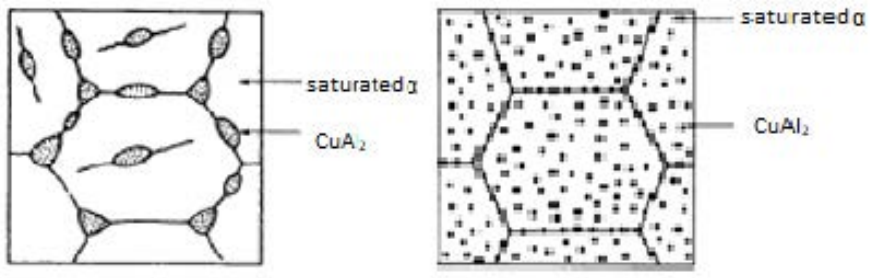

Figure 2.12: Precipitation mechanism in Aluminum alloy. On the left, a long cooling time is used, on the right, a high speed of cooling is used [9].

2.1.3.1.5 Solid solution hardening

Many alloys are solid solution made by one or more metals dissolved in another metal:

- When the atoms of the alloying elements take the place of some atoms of the base metal in the crystalline lattice, there is a substitutional solid solution (see Figure 2.13)
- When these interpose themselves between the atoms of the lattice it is called interstitial solid solution.

In both cases the lattice is distorted, delaying the movement of the dislocations and thus strengthening the material. The 5000 series with magnesium as a solute is a good example. Many aluminum alloys undergo hardening for solid solution for effect of one or more elements that are dissolved in the base aluminum, the contribution of each element in the strengthening of the alloy is added to that of the others. Often these alloys are subsequently strengthened by heat treatment or by mechanical processing.

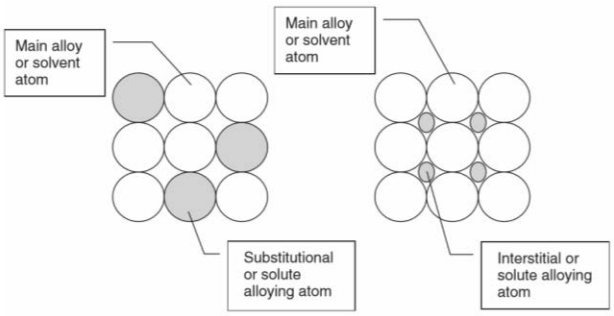

Figure 2.13: Schematic illustration of substitutional and interstitial alloying [13].

2.1.3.1.6 Precipitation Hardening

Precipitation hardening is one of the methods used to improve mechanical properties of a metal. It is a particularly effective mechanism in alloys such as magnesium, titanium and aluminum ones.

The precipitation hardening mechanism consists in increasing the difficulty of movement for dislocations, due to an appropriate distribution of particles inside the grains. It is better to avoid the formation of precipitates on grain boundaries, since they already act as barriers for the dislocations movement. It is also preferable to obtain a homogeneous distribution of particles, since a non-homogeneous concentration of the precipitates involves in non-homogeneous mechanical properties.

The size of the particles is very important: small size particles give better mechanical properties. An important difference, especially regarding aluminum alloys, is the one between coherent and incoherent precipitates. The coherent ones have a different stoichiometry from the matrix, but the structure is the same. The hardening effect consists mainly in the fact that dislocations are no longer free to move in the lattice because this is distorted. The incoherent precipitates have the same stoichiometry of the matrix but a different structure. In this case the hardening effect is due both to an increase in the difficulty of the dislocation motion and to an increase in the concentration of dislocations through the mechanism known with the name of Orowan looping (Figure 2.14).

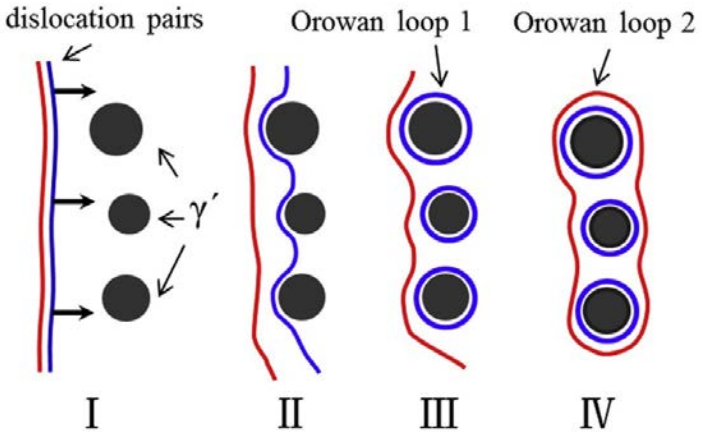

Figure 2.14:Schematic illustration of a double Orowan looping process [14].

The increase in hardness develops mainly during the initial stages of precipitation from a solid supersaturated solution. Considering for example the Al-Mg_2Si phase diagram as

represented in Figure 2.15, the solubility of the alloying elements at different temperatures can be seen.

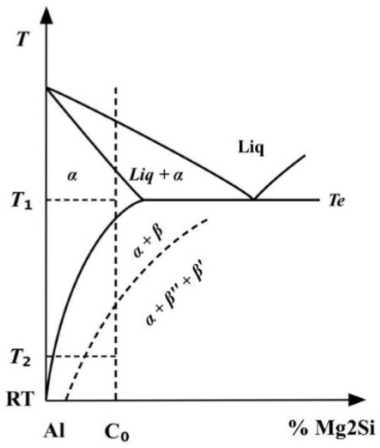

Figure 2.15: Al-Mg_2Si phase diagram.

Precipitation hardening is obtained a heat treatment which consists of 2 stages: solubilization and aging.

Solubilization

In this stage the material is heated to a temperature T1 greater than the solubilization temperature and the whole Mg_2Si phase is dissolved in the matrix constituted by the most abundant phase (aluminum). The piece is maintained at this temperature for enough time to dissolve the precipitates, until a homogeneous solid solution is obtained.

Rapid cooling (hardening) allows to "freeze" this microstructure up to ambient temperature: a metastable condition in which the solution is supersaturated is obtained. The metastable condition obtained, does not show better mechanical properties, compared to the starting material, but this condition is needed for the achievement of the properties and characteristics described below.

Since the hardening mechanisms consist of obstructing the movement of the dislocations, what we want to achieve in the second phase of the process described is the precipitation of the β phase (Mg_2Si) inside the grain (intragranular precipitation) forming precipitate finely dispersed in the whole crystalline grain. The tempering is necessary to avoid the formation of precipitates on the grain boundaries, where the dislocations already have no possibility of movement.

In Figure 2.16 the X condition is representative of the solubilization. The A condition, on the other hand, represents the microstructural state after quenching, the end of this first stage of the hardening process. The undesired D situation is due to a not correct cooling process.

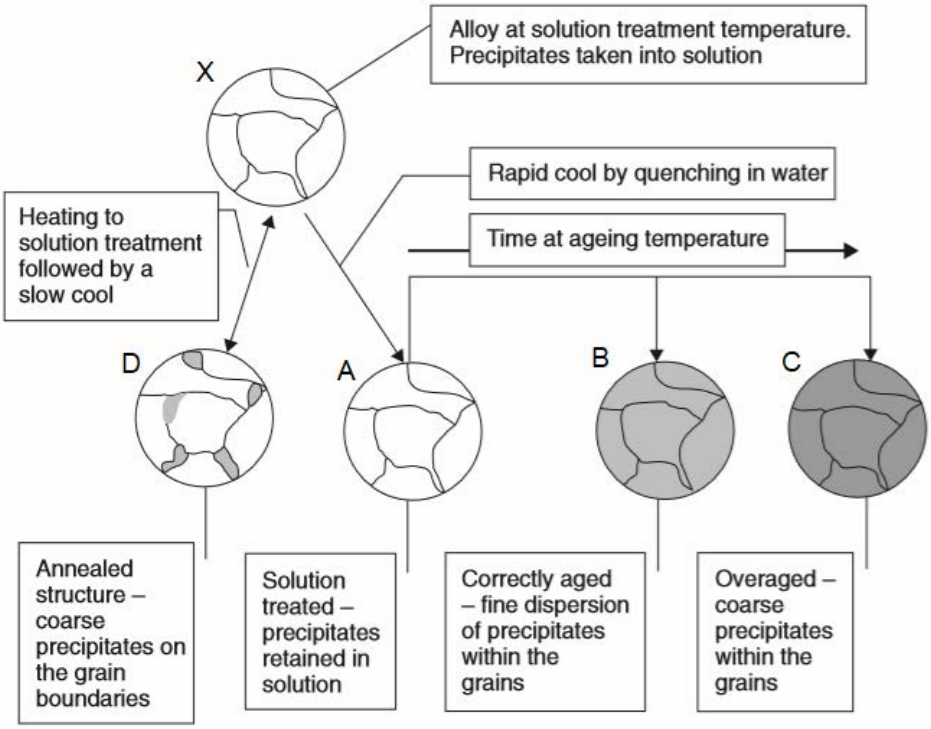

Figure 2.16: Illustration of the solution treatment and age-(precipitation) hardening heat treatment cycle [13].

From the energetic point of view the excess of solute compared to the equilibrium condition causes a difference in the free energy ΔG such that the material tends to restore the equilibrium condition. The excess of free energy is the driving force that push the supersaturated solution to expel the solute in excess: this is the cause of the tendency to make the phase β precipitate. However, this mechanism is extremely slow at room temperature.

Aging

The second part of the heat treatment is the aging. In this stage, to enable the diffusion of atomic species, the temperature is maintained lower than the solubilization one. The intragranular (homogeneous) precipitation of the β phase occurs. The formation of precipitates follows the classic mechanism of nucleation and growth. After a period, necessary for the formation of stable nuclei, the process continues rapidly until a slowdown

caused by the progressive decreasing of solute in the solution. Consider now the strength-time curve of the aging stage (Figure 2.17).

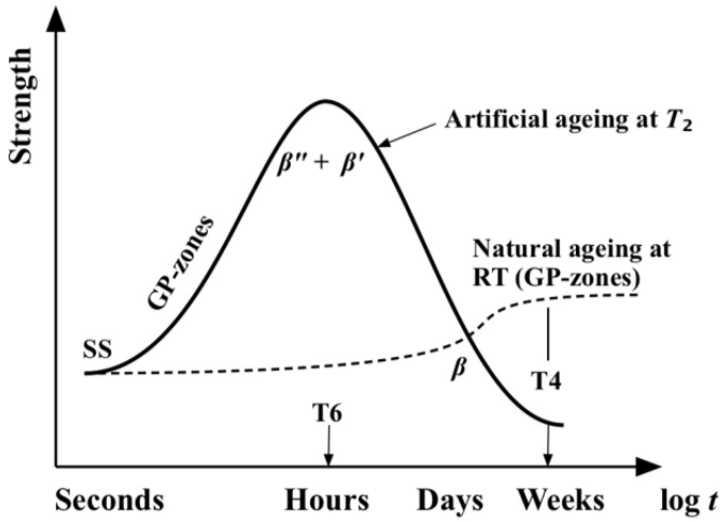

Figure 2.17: Strength evolution during artificial and natural aging of Al-Mg-Si alloys. Copied from [6].

The trend of the graph is due to the precipitation mechanism of β. Artificial aging is used to precipitate strengthening phases throughout the metal (in a controlled way) [4]. The precipitation sequence occurring during precipitation hardening can be summarized as follows:

$$SSSS \rightarrow GP1 \rightarrow \beta'' \rightarrow \beta'(Mg_2Si) \rightarrow \beta(Mg_2Si)$$

The most effective hardening phase, β'', are fully coherent, needle shaped precipitates lying along the $[100]_{Al}$ directions with a monoclinic crystallographic structure. In addition to the fine β'' precipitates, the coarse rod-shaped β'-precipitates will also contribute to an increase in the strength. The properties constantly evolve with ageing time at the ageing temperature.

This can be seen from Figure 2.17, where strength and hardness increase with time to some peak values [6]. This condition is referred to as the peak-aged (T6) condition, where the base metal contains a mixture of the two metastable β'' and β' precipitates [5]. With the progress of the process time, there is a degradation of the mechanical properties: it is called over-aging. Responsible for this is the phenomenon of coalescence of the finely dispersed precipitates to form large precipitates.

The resulting mechanical properties at room temperature are directly linked to the number density and size distribution of the hardening precipitates that form during artificial ageing.

The parameters that influence the entire process of precipitation hardening are substantially two: the temperature and the chemical composition.

As can be seen in Figure 2.18 the process is faster at high temperature, anticipating the peak of hardness, mainly due to the higher spreading speed. The value of the maximum hardness decreases with the increasing of temperature.

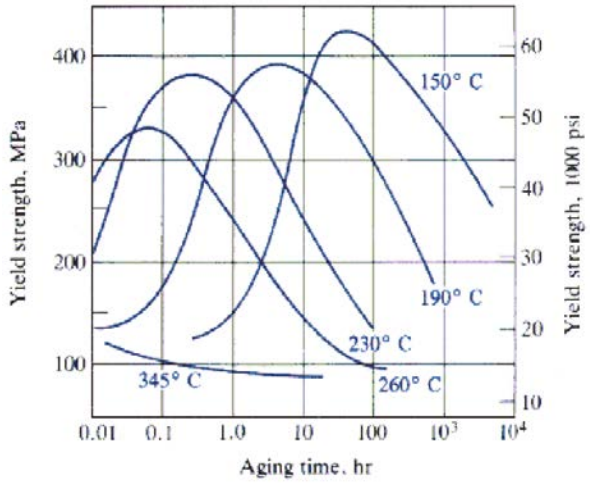

Figure 2.18: Time of aging-Strength at different temperatures [9].

2.2 Welding process

Welding can be described as the joining of two components by a coalescence of the surfaces in contact with each other. This coalescence can be achieved by melting the two parts together (fusion welding) or by bringing the two parts together under pressure, perhaps with the application of heat, to form a metallic bond across the interface. This is known as solid phase joining and is one of the oldest of the joining techniques, blacksmith's hammer welding having been used for iron implement manufacture for some 3500 years. The more modern solid phase techniques are typified by friction welding [15]. Table 2.3 gives an overview of the main processes used for the welding of aluminum.

Table 2.3: Principal processes for the welding of aluminum [13]

Process	Application
Fusion welding	
Tungsten inert gas	High-quality, all position welding process that utilises a non-consumable electrode; may be used with or without wire additions; may be manual, mechanised or fully automated; low deposition rate, higher with hot wire additions; straight or pulsed current.
Metallic arc inert gas shielded	High-quality, all position welding process that utilises a continuously fed wire; may be manual, mechanised or fully automated; can be high deposition rate; twin wire additions; straight or pulsed current.
Manual metal arc	Limited application; uses a flux-coated consumable electrode; non- or lightly stressed joints; obsolescent.
Oxy-gas	Low-quality weld metal; unstressed joints; obsolescent.
Electron beam welding	High-quality, precision welding; aerospace/defence and electronic equipment; high capital cost; vacuum chamber required.
Laser welding	High-quality, precision welding; aerospace/defence and electronic equipment; high capital cost.
Electro-gas, electro-slag, submerged arc	Limited applications, e.g. large bus bars; porosity problems; largely obsolescent.
Welding with fusion and pressure	
Magnetically impelled arc butt welding	Butt joints in pipe; capital equipment required but lower cost than flash butt; fully automated.
Resistance and flash welding	
Spot, projection spot seam welding	Lap joints in sheet metal work, automotive, holloware, aerospace industry; high capital cost; high productivity.
Weld bonding	Combination of spot welding through an adhesively bonded lap joint; automotive industry; very good fatigue strength.
High-frequency induction seam	Butt joints; production of pipe from strip; high capital cost; high production rates.
Flash butt welding	In line and mitre butt joints in sheet, bar and hollow sections; dissimilar metal joints, e.g. Al-Cu; high capital cost; high production rates.

Stud welding	
Condenser, capacitor discharge	Stud diameters 6mm max, e.g. insulating pins, pan handles, automotive trim, electrical contacts.
Drawn arc	Stud diameters 5–12mm.
Solid phase bonding	
Friction welding	Butt joints in round and rectangular bar and hollow sections; flat plate and rolled section butt welds (friction stir); dissimilar metal joints; capital equipment required.
Explosive welding	Field pipeline joints; dissimilar metal joints, surfacing.
Ultrasonic welding	Lap joints in foil; thin to thick sections; Al-Cu joints for electrical terminations.
Cold pressure welding	Lap and butt joints, e.g. Al-Cu, Al-steel, Al sheet and wire.
Hot pressure welding	Roll bonded lap joints, edge to edge butt joints.

The main factors to consider in the aluminum welding are: thermal conductivity, coefficient of thermal expansion, characteristics of the molten metal and electrical conductivity.

The thermal conductivity factor is the most important among those that characterize welding and weldability in general. In the case of aluminum welding, to achieve optimal conditions of the welded joint, the necessary heat must be supplied four times faster than for low carbon steel. The high thermal conductivity of aluminum alloys helps solidify the molten bath, but also leads to rapid heat dispersion within the metal: it is therefore appropriate using powerful and concentrated heat sources to limit the heat affected area.

Linear thermal expansion coefficient: The coefficient of linear thermal expansion is about twice the steel one. The high values of this coefficient and of the thermal conductivity are the first causes of the considerable distortions that they often characterize the welding of aluminum.

Characteristics of the molten metal: The melting ranges of the alloys of aluminum, as well as specific heat and latent heat, are considerably lower with respect to copper and steel ones: the amount of heat necessary for welding results relatively low.

Electrical conductivity: Aluminum has a very high electric conductivity compared to steel, and this is the reason why, even if the temperatures to reach are lower, the current that must be used is very high. This parameter assumes fundamental importance in the resistance welding processes: the resistance that the metal opposes to the current is the cause of the heat necessary for the welding.

2.2.1 MIG welding

The metal arc inert gas shielded process, also known as MIG, MAGS or GMAW, was first used in the USA in the 1940s. Since those early days the process has found extensive use in a wide range of industries from automotive manufacture to cross-country pipelines. It is an arc welding process that uses a continuously fed wire both as electrode and as filler metal, the arc and the weld pool being protected by an inert gas shield. It offers the advantages of high welding speeds, smaller heat affected zones than TIG welding, excellent oxide film removal during welding and an all positional welding capability. For these reasons MIG welding is the most widely used manual arc welding process for the joining of aluminum [16]. Today, GMAW is the most common industrial welding process, preferred for its versatility, speed and the relative ease of adapting the process to robotic automation.

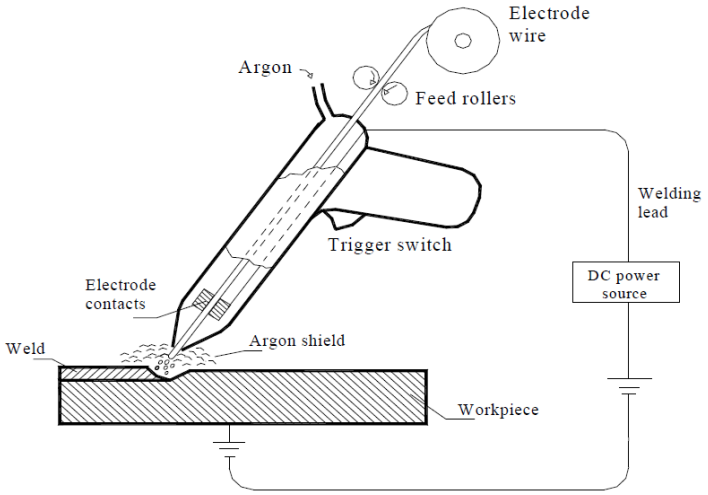

Figure 2.19: Sketch of the GMAW process

Fusion welding produces a locally modified microstructure and fluctuating mechanical properties. Different zones can be identified as a result of local alloy composition changes and/or the temperature cycle during welding. These zones are schematically shown in Figure 2.20. Depending on the actual heat input and the geometry of the joint, the width of these zones can vary considerably [6].

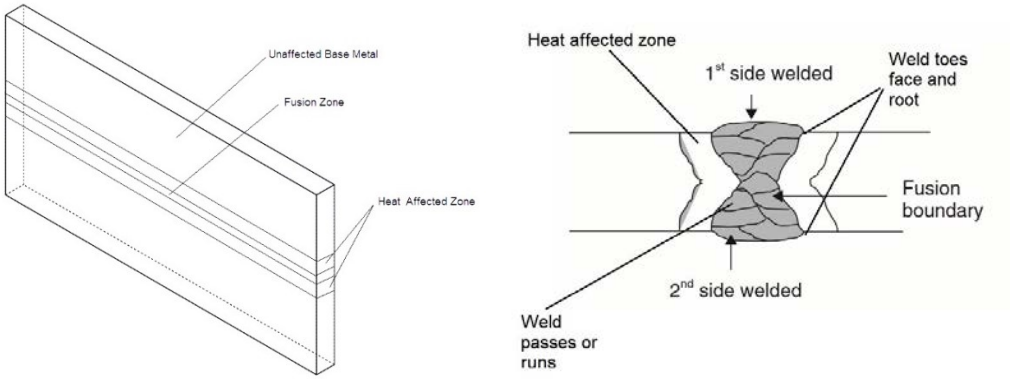

Figure 2.20: Sketch of the different zones which may form in a welded component.

In the fusion zone (FZ) the metal goes back to the as-cast state (Figure 2.20), so that all the processing steps done before are forgotten by the material. In this zone, the microstructure depends on the solidification behavior of the weld pool, which is the responsible for the size and the shape of the grains, segregation, inclusions and porosity formation. In fusion welding of aluminum, the fusion and re-solidification process of the metal makes the material to become brittle, because of the formation of brittle inter-dendritic structure and eutectic phases. This leads to a drastic decrease in the mechanical properties.

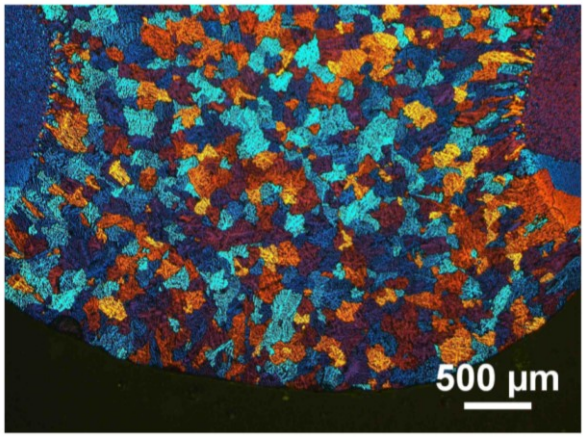

Figure 2.21: Optical micrograph showing the fusion zone of an aluminum alloy (welded with filler material AA5183). Copied from [6].

During the welding process, sub-grains nucleate directly from randomly oriented grains in the parent material (in the Heat Affected Zone), which form the substrate at the fusion boundary. When the temperature goes down, the growth of new grains occurs. New crystals nucleate by arranging atoms from the HAZ grains, following their existing crystallographic orientation. This is described as epitaxial growth, as shown in the following Figure 2.22.

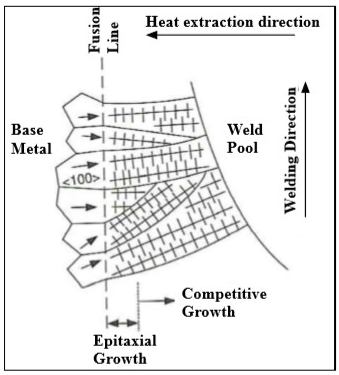

Figure 2.22: Epitaxial growth at the fusion boundary. Copied from [6] .

The FZ grain structure is mainly determined by the base metal structure and the welding conditions. Grains tend to grow perpendicular to the pool boundary along the maximum direction of heat extraction. In addition to this, crystallographic effects will influence grain growth by favoring growth along the easy growth direction, namely the <100>-direction (Figure 2.22). Conditions for growth are optimum when one of the easy growth directions coincides with the heat-flow direction. These grains grow faster than grains less favorably oriented, and this results in formation of solidification grain boundaries at regions where these sub-grains impinge (competitive growth). Without additional nucleation, this will promote a columnar grain structure. The weld (FZ) microstructure varies noticeably from the edge to the centerline of the weld. This is because the temperature gradient G and the growth rate R dominate the solidification microstructure. Since the ratio between the temperature gradient and the growth rate G/R decreases from the fusion line toward the centerline, the solidification mode may change across the fusion zone [6]. This is shown in Figure 2.23.

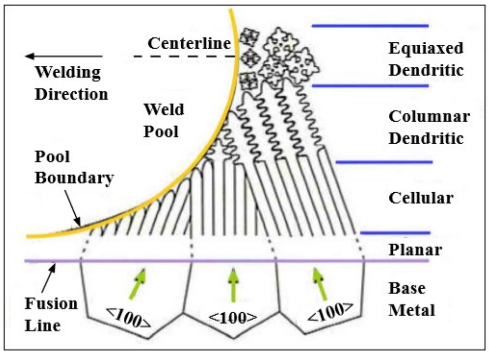

Figure 2.23: Solidification modes across the fusion line. Copied from [6].

The heat-affected zone (HAZ) represents a major problem because the resulting microstructural changes lead to a permanent mechanical degradation of the base metal. After artificial ageing, a high density of the fine needle-shaped β'' particles is present in the matrix, see Figure 2.24 (a). These particles are thermodynamically unstable in a welding situation, so the smallest particles will start to dissolve in parts of the HAZ where the peak temperature exceeds 220°C. The larger particles continue to grow, see Figure 2.24.

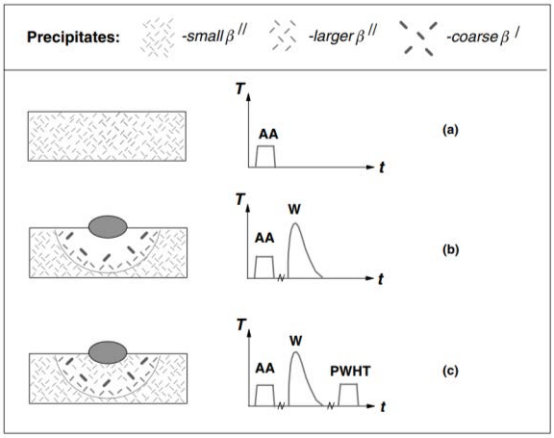

Figure 2.24: Schematic diagrams showing the microstructure evolution during multistage thermal processing of Al–Mg–Si alloys involving heat treatment and welding. AA: artificial ageing, W: welding, PWHT: post weld heat treatment. The outer boundary of the HAZ is indicated by the semicircles in the diagrams. [17]

Close to the weld fusion line full reversion of the β'' particles is achieved. At the same time, coarse rod-shaped β' precipitates may form in the intermediate peak temperature range between 220-500°C. The minimum HAZ hardness is found in the position of the HAZ that experience temperatures within this range. This zone is also referred to as the overaged zone [4]. Figure 2.25 shows a sketch of the typical HAZ strength profile for a peak-aged Al-alloy after complete natural ageing.

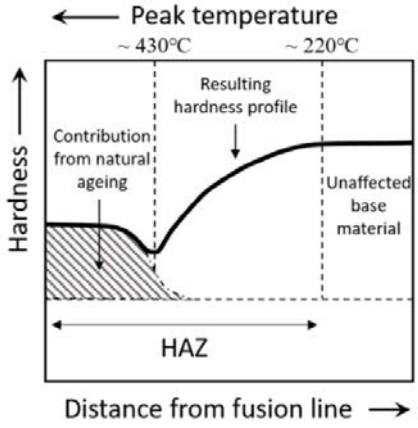

Figure 2.25: Relation between peak temperature and hardness distribution in an AA6082-T6 weld. Copied from [18]

At higher temperatures, in positions close to the fusion line, particles are dissolved, and their constituent elements go into solid solution. Upon natural ageing (cooling) subsequent to welding, this solute may precipitate as strengthening phases. This contributes to the slight increase in hardness that typically occurs near the FZ for the 6xxx series alloys, see Figure 2.25 in the previous page.

2.2.2 Aluminum weldability problems

A proper welding process should not cause harmful discontinuities, such as hot cracks (as a welding effect or as a consequence of post-welding heat treatment), cold cracks (caused by absorption of hydrogen, in the presence of humidity), porosity or blanks.

In addition to this, it must be considered that due to welding, the properties of the base metal are changed not only in the fused area, but also in the HAZ (Heat Affected Zone), a region near to the real joint, which does not mix with it, but that is structurally modified by the heat generated by the welding process and by the heat cycle induced by it.

Obviously, the usability of a welding is related to the application to which the welded piece is intended.

2.2.2.1 Problems deriving from superficial oxide.

Aluminum and its alloys, in presence of air, show the tendency to immediately form a layer of oxide on the surface (Al_2O_3), whose thickness is on average 10 Å. The thickness and the formation speed depend on many factors, especially the composition of the alloy (magnesium, for example, even if in small percentages, accelerates this formation) and the temperature (as it increases, the thickness of the layer tends to increase, as well as its formation speed).

The Al_2O_3 oxide melts at about 2050 ° C, a value much higher than the melting temperature of the base metal: these can remain trapped inside the molten causing serious consequences such as loss of ductility, cracks formation, areas in which perfect fusion is not reached.

Another characteristic of alumina that conditions the process is its high density (3600 kg / m^3) with respect to the molten alloy (aluminum 2300 kg / m^3, maximum value of aluminum alloys 3000 kg / m^3). For this reason, the oxide has the tendency to remain imprisoned, during the solidification, creating inhomogeneities and inclusions: this can cause the loss of mechanical resistance of the joint, and promote corrosion mechanism. During welding, oxidation can be prevented by protecting the entire area involved in melting and heating by using inert gases, flows antioxidants, or with the use of appropriate coatings. The flows, solidified on the surface in the welding zones, must be removed: in the case it doesn't happen, the flows would continue to exercise theirs absorbing action against alumina, eliminating the passivating oxide layer.

2.2.2.2 Welding defects

Welding defects are interruptions in the physical structure of the junction. Defects can be classified into three categories: caused by the project, caused by the welding process and caused by metallurgical reasons.

The first class of defects includes issues that involve design or structural parameters, such as the wrong choice of the type of joint for a given application or unacceptable variations through the junction sections.

Process defects include:

a) **Undercut**: a groove in the base metal adjacent to the base of the joint, not filled with base metal. Visible undercut is associated with improper welding techniques or excessive currents, or both. Undercuts creates a mechanical notch at the weld toe. In addition to the stress raiser caused by the undercut notch, fatigue properties are reduced.
b) **Slag inclusion**: a solid and non-metallic particle remains trapped in the welded metal or between the welded metal and the base metal.
c) **Porosity**: defect formed by trapped gas during the solidification process. Porosity has little effect on strength, some effect on ductility, and significant effects on fatigue strength and toughness. External porosity is more injurious than internal porosity because of the stress concentration effects. Porosity is considered a spherical and non-planar imperfection, thereby not a serious threat to weld in normal loading and even in fatigue conditions. The tolerance of porosity in such condition is liberal, and often up to 5% porosity in standard radiograph length is accepted.
d) **Overlap**: the protraction of the welded metal over the head, the face or the root of the welded joint. It's a surface discontinuity that forms a severe mechanical notch parallel to the weld axis. Fatigue properties are reduced by the presence of this, as it could be the initial point for cracks.
e) **Defect from the support**: damage caused by the removal of the plate used to support the melted metal.
f) **Shrinkage cavity**: cavity in the welded metal caused by the natural shrinkage during solidification.
g) **Oxide inclusions**: surface oxide particles that have not been melted and which are trapped in the welded metal.
h) **Lack of fusion (LOF)**: condition characterized by the incomplete fusion of the metal. This is a stress-concentrating flaw and can in most cases initiate cracks.
i) **Lack of penetration (LOP)**: condition in which the welding penetration is lower than the design specification. It may result from insufficient heat input, improper joint

design, incorrect bevel angle, or poor control of the arc. Like LOF, this is a stress-concentration point, and crack can initiate in the un-fused area.

j) **Craters**: cavities at the ends of the weld or in the pit of molten metal.

k) **Underfill**: a depression on the face of the welding or on the base surface in the welded metal, which extends just below the surface of the adjacent base metal. Underfill results from the failure to fill the joint with weld metal, as required. It is corrected by adding additional layers of weld metal. If left this becomes a stress concentration point and may be cause of the failure.

In the following Figure 2.26, the main defects in welding are shown.

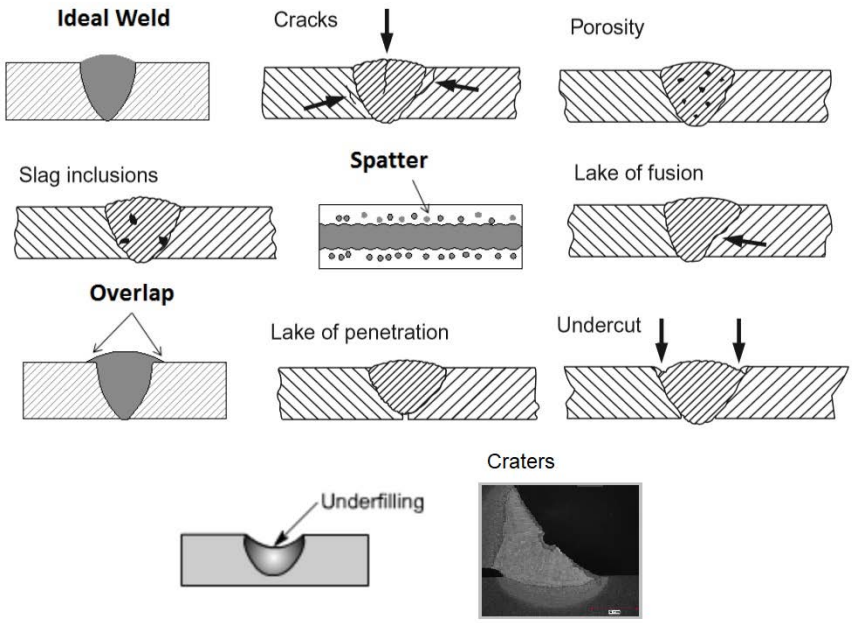

Figure 2.26: Main welding defects.

Metallurgical defects are:

a) **Cracking**: defect consisting of a fracture characterized by a sharp, pointed opening with a high ratio length/width. In most cases cracks occur when the localized stresses exceed the tensile strength of the material. Cracking is often associated with stress amplification near discontinuities in welds and base metal, or near mechanical notches associated with weldment design.

b) **Segregation**: the non-uniform distribution or concentration of impurities or alloying elements that emerge during solidification.

c) **Lamellar tearing**: a type of fracture that runs through the base metal or in the heat affected zone, it is the result of a low ductility along the thickness of the joint.

There are some defects that are more relevant considering their frequency and their effect on the joint. These are the porosity, lack of fusion/penetration and cracking.

The **porosity** formed on the surface of the welding or in the areas adjacent to it, in particular they can be located on the base or on the head of the joint.

This type of defect, as already mentioned before, can be caused by gas in the molten metal, due to a not proper cleaning operation during the preparation of the joint, but also from humidity present on the base metal or on the filler metal, and in this case the formation of the pores is to be attributed to the presence of hydrogen, which has a very low solubility in the metal. Different types of porosity can be identified on the base of the amount and distribution of the "bubbles" (see Figure 2.27).

- Uniformly distributed porosity;
- Clustered porosity: areas with many pores and areas free of porosity;
- Linear porosity: pores that have a linear distribution. This type of porosity takes place at the base of the welding and it is associated with the lack of penetration;
- Worm hole porosity.

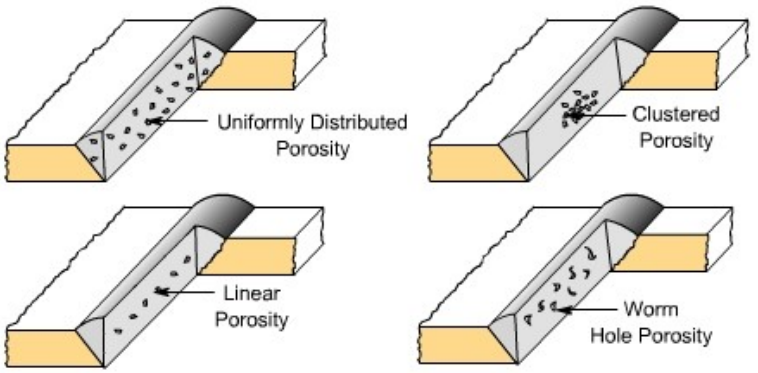

Figure 2.27: Types of porosity.

The identification of the porosity is performed by radiographic or ultrasound examination.

The **lack of fusion** and the **lack of penetration** (see Figure 2.28) are caused by inadequate welding conditions.
It is evident that there can be fusion without complete penetration and vice versa. Lack of fusion is usually localized on the side of the welding, while lack of penetration is localized on the bottom of the joint (in the case of single side welding).

The causes of LOP can be attributed to the high speed of welding, to an excessive size of the electrode or of the tool, to a high angle of the joint (very acute angle), incorrect manipulation of the tools, etc.
The causes of LOF are, on the other side, imputable to a low electrode current, to an excessive welding speed, to an incorrect handling, to the presence of oxides and oils that prevent the complete melting of the metal.

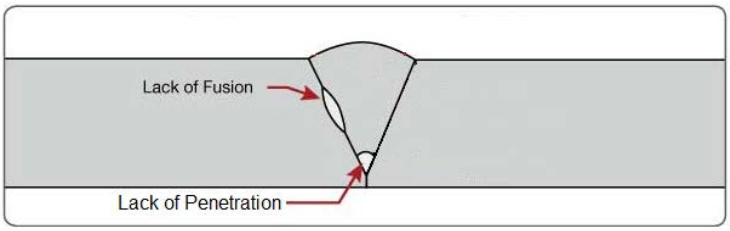

Figure 2.28: Sketch of LOF and LOP.

The **cracks** can be in the fused zone or in the base metal.

In most cases cracks occur when the localized stresses exceed strength of the material. Cracking is often associated with stress amplification near discontinuities in welds and base metal, or near mechanical notches associated with weldment design. Hot cracks develop at elevated temperatures during or just after solidification. They propagate between the grains. Cold cracks are often delayed and associated with hydrogen embrittlement. They propagate both between and through grains. Throat cracks run longitudinally in the face of the weld and extend toward the root. Root cracks run longitudinally and originate in the root of the weld. Longitudinal cracks are associated with high welding speeds or with high cooling and related restraint. Transverse cracks are perpendicular to the weld and may propagate from the weld metal into the HAZ and the base metal. Transverse cracks are associated with longitudinal shrinkage stressed in weld metal that is embrittled by hydrogen. Crater cracks are formed by improper termination of the welding arc. They are shallow hot cracks.

Toe cracks are cold cracks that initiate normal to the base metal and propagate from the toes of the weld where residual stresses are higher. They result from thermal shrinkage strains acting on embrittled HAZ metal. Under-bead cracks are cold cracks that form in the HAZ when three conditions are met:

- Hydrogen in solid solution
- Crack-susceptible microstructure
- High residual stresses

None of the above can be detected by visual inspection and do not normally extend to the surface. Cracking in any form is an unacceptable discontinuity and is the most detrimental type of welding discontinuity. Cracks must be removed [13].

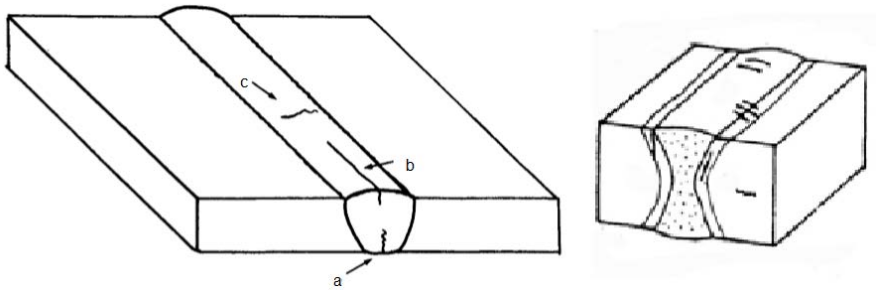

Figure 2.29: Types of cracks. a) on the top b) longitudinal c) transversal

2.2.2.3 Residual stresses

The residual stresses are stresses that occur in the welded joints for effect of localized heat application. They have the feature to remain in the joint even when this has been completed. The residual stresses are in general the stresses present inside the piece even when all external loads have been removed. In particular, the thermal residual stresses refer to thermal loads and to their variations. The stresses can often cause cracks in the welded joints. These solicitations can also give a premature breaking of the structure, if subjected to certain conditions. As a welded joint is subject to the action of a mobile thermal source, the distribution of temperatures in it is not uniform, but varies during the whole process: consequently, during the welding heat cycle, the welded area and surrounding area are subject to complex thermal stresses. In the following Figure 2.30 it can be seen the trend of temperatures and tensions during welding in the different sections of the joint.

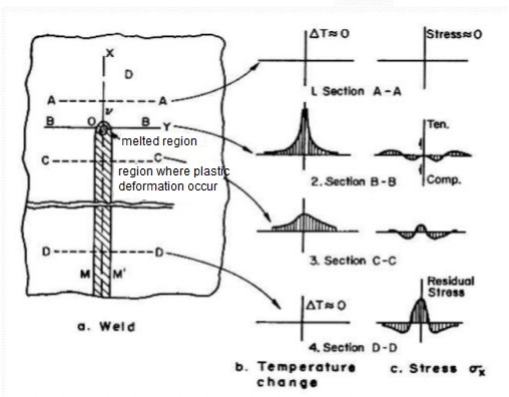

Figure 2.30: Trend of temperatures and tensions during welding in the different sections of the joint.

2.2.2.4 Welding distortions

Another problem in the aluminum welding process consists in the distortions of the joints after cooling. The reason of this problem can be attributed to the non-uniform heating-cooling cycle during a welding operation, which determines the complex distortions within the joint. These effects and the consequent reactions of the metal produce internal forces that cause bends, rotations, buckling. These dimensional variations are known as cooling distortions and they are shown in the following Figure 2.31.

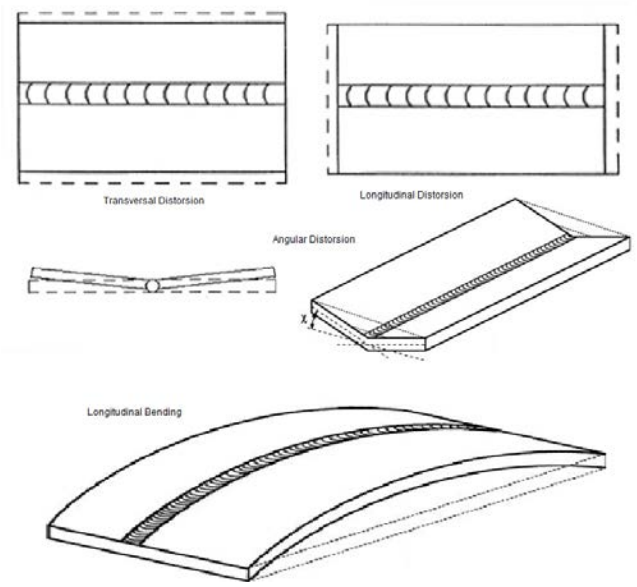

Figure 2.31: Welding distortions.

The problem of distortions occurs particularly in aluminum welding because of physical characteristics that this metal presents: high coefficient of linear thermal expansion, high thermal conductivity, low modulus of elasticity. All this means that with the same welding technique, the shrinkage is three times higher than the one of the steel.
In the upper part of Figure 2.31, a transverse and a longitudinal distortion is shown in the case of uniform shrinkage along the welding; the uniformity of the deformation is rather rare, especially if the plates are long.
The transverse and longitudinal shrinkages are mainly caused by the contraction of the base metal. The shrinkage of the welded metal constitutes only a 10% of the total shrinkage.
When two plates are welded, the opposite sides move generating an angular distortion. This problem was present in our case, and it was considered in the tests results analysis.

2.2.2.5 Heat affected zone

As mentioned earlier, alloys in the as-cast or annealed condition may be welded without any significant loss of strength in the HAZ, the strength of the weldment matching that of the parent metal. Where the alloy has had its strength enhanced by cold work or precipitation

hardening then there may be a substantial loss of strength in the HAZ. The cold worked alloys will experience a loss of strength due to recrystallisation in the HAZ. Recrystallisation begins to take place when the temperature in the HAZ exceeds 200°C and progressively increases with full annealing taking place over 300°C. The high temperatures reached cause structural changes in the HAZ due to the dissolution or to the growth of precipitates. Depending on the aluminum alloy, the temperature beyond which the material is believed to be thermal affected, varies between 240 and 250 ° C. Typically, the HAZ can be subdivided into two sites with different characteristics: the area adjacent to the welding bead, where higher temperatures are reached, there is the complete solution of the grains, thus giving characteristics of low strength but good ductility; the area where the temperature is lower than the solubilization one, but higher than the aging one. Here, various degrees of aging and therefore different characteristics of hardness and ductility are reach, depending on the temperature (which decreases moving away from bead) and on the maintenance time of that.

The HAZ consists in various degrees of dissolution and dimension of the grains depending on the thermal conditions reached. The welding procedure and the parameters used determine the dimension of the heat affected zone: high values of the heat generated, or the preheating process increase the size values and the degree of alteration of the HAZ. The deterioration of the HAZ can be reduced, for example, by using several passes, checking the temperature at each single pass and avoiding preheating. In Figure 2.32 a typical hardness profile of a welded aluminum alloy is shown.

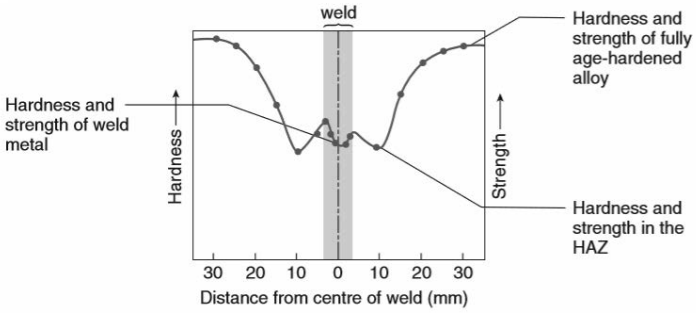

Figure 2.32: Effect of welding on 6061 T6 age-hardened alloy – as welded [13].

2.3 Load-bearing capacity of welded components

The HAZ softening does a great effect on the load bearing capacity in welding of precipitation hardened aluminum alloy. The weakest part of the welded components is the bottle-neck in bearing capacity, and it takes place in the HAZ, as the minimum strength level is in this region. As shown in the following Figure 2.33, two idealized loading conditions is examined in detail.

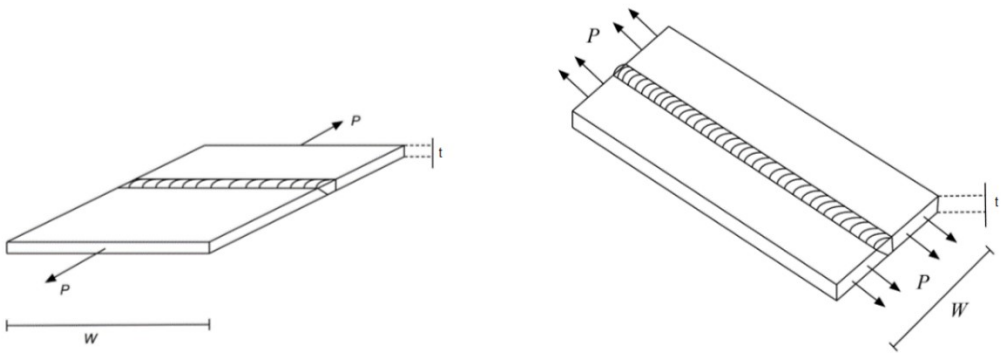

Figure 2.33: The two idealized loading conditions being examined. (a) Loading perpendicular to weld. (b) Loading parallel to weld. Copied from [6]

The measured HAZ hardness profile can be used to calculate the yield stress across the HAZ by using the relationship:

$$\sigma_y = 3.0*HV - 48 \quad (1)$$

By inserting the minimum value from the HAZ hardness profile into Equation (1), the corresponding minimum HAZ yield strength σ_{min} [MPa] can be found. If the loading is perpendicular to the weld, as shown in Figure 2.33, the load-bearing capacity P [N] can be calculated by using the relationship:

$$\sigma_{min} = \frac{P}{Wt} \quad (2)$$

from which:

$$P = \sigma_{min} * (Wt) \quad (3)$$

where P [N] is the maximum tensile (or compressive) force that can be applied perpendicular to the axis of the weld, t [mm] is the plate thickness and W [mm] is the width of the component.

If the loading is parallel to the welding, as shown in Figure 2.34, the calculations of the design stress become more complex. In this approach, Mazzolani introduces the idea of reduced cross-sectional area A_{red} as a basis for calculating the design stress. Figure 2.34 is a sketch showing how the equivalent half width of reduced strength zone y_{red}^{eq} of minimum strength σ_{min} is related to an assumed yield strength profile across the weld.

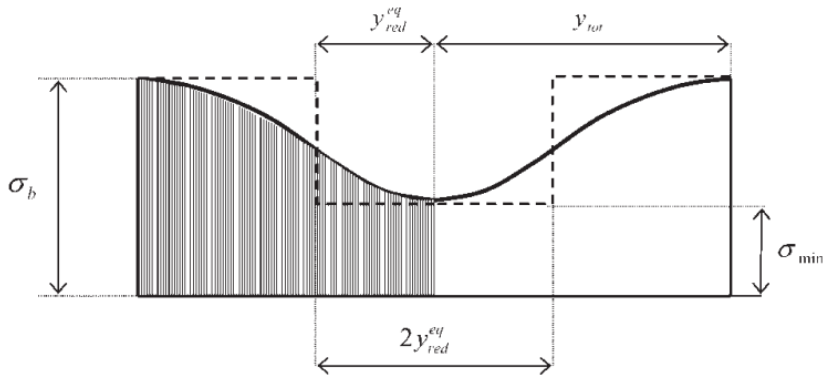

Figure 2.34: Sketch showing how equivalent half width of reduced strength zone Δy_{red}^{eq} of minimum strength σ_{min} is related to assumed yield strength profile across weld: diagram is based on ideas of Mazzolini [19].

The so called reduced cross-sectional area A_{red} is a basis for calculating the design stress, which according to the definitions in Figure 2.34 can be written as:

$$A_{red} = A - 2y_{red}^{eq} * t * (1 - \beta) \quad (4)$$

where A is the total cross-section area of the joint (including the weld reinforcement), y_{red}^{eq} is equivalent half width of the reduced strength zone (including the weld metal) of strength σ_{min}, while b is a metallurgical efficiency factor that takes into account the degree of softening occurring due to welding $\beta<1$. Thus, provided that yielding is not permitted during service,

β is equal to the ratio between the minimum HAZ yield stress σ_{min} and the base metal yield stress σ_b.

$$\beta = \frac{\sigma_{min}}{\sigma_b} \tag{5}$$

Similarly, the equivalent half width of the reduced strength zone y_{red}^{eq} of strength σmin can be calculated by considering the idealised yield strength profile shown in Figure 2.35 and solving the integral:

$$y_{red}^{eq} = \frac{\int_0^{\infty} (\sigma_b - \sigma(y))\,dy}{(\sigma_b - \sigma_{min})} \tag{6}$$

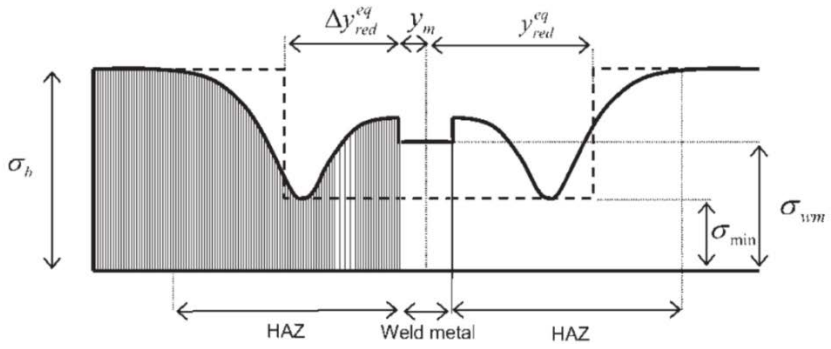

Figure 2.35: Schematic diagram showing yield strength profile across AA6082-T6 butt weld following complete natural aging: equivalent half widths of reduced strength zones y_{red}^{eq} and Δy_{red}^{eq} of minimum strength σ_{min} are defined to right and left in diagram respectively. [19]

2.4 Tensile test

The stress-strain curve

An engineering stress-stain curve is made by data from a tensile test, plotted as stress [MPa] versus strain [mm/mm], see in Figure 2.36 below. In a tensile test, the tensile specimen is subjected to a tensile force until fracture.

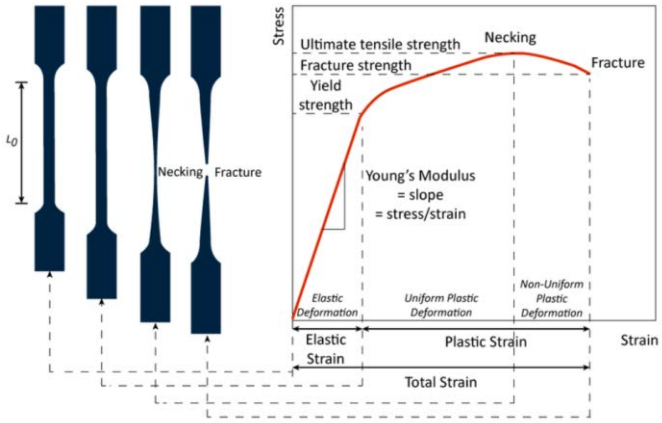

Figure 2.36: example of stress-strain curve.

During the linear part of the stress-strain curve, the material is not permanently deformed. This is called elastic deformation. After the linear part, the material is permanently deformed, this is called plastic deformation. The engineering stress (σ) is defined as the force (F) divided by the original area (A_0),

$$\sigma = \frac{F}{A_0} \tag{7}$$

The engineering strain (ε) is defined as the elongation of the material ($L - L_0$) divided by the original length (L_0),

$$\varepsilon = \frac{L - L_0}{L_0} \tag{8}$$

The stress-strain curve provides several information such as yield strength (σ_y) and ultimate tensile strength (σ_{UTS}). The yield strength is defined as the intersection between the stress-

strain curve and a line drawn parallel to the curve from a strain equal to 0.002. Thus, the yield strength is the stress which will produce a small amount of plastic strain.

Another important feature from the stress-strain curve is the amount of work hardening. The amount of work hardening is the increase of stress from the yield strength to the ultimate tensile strength, hence strengthening during plastic deformation. Work hardening is defined as the increase in stress needed to induce slip as a consequence of previous plastic deformation. Hence, work hardening happens because of dislocation movement and the generating of dislocations.

2.5 Fatigue

In materials science, fatigue is the progressive and localized structural damage that occurs when a material is subjected to cyclic loading. The maximum stress values are less than the ultimate tensile stress limit and may be below the yield stress limit of the material.

2.5.1 The SN-curve

Fatigue data can be presented as a SN curve, where S stands for stress and N for number of cycles until failure, displayed in Figure 2.37. The fatigue strength is the stress level where failure will occur for a specified number of cycles. The number of cycles at failure is called the fatigue life, N_f. The fatigue strength and fatigue life are marked on Figure 2.37. Some metals, like titanium and steel, have a so-called fatigue limit, where the SN-curve becomes horizontal at a limiting stress, and the metal can endure an infinite number of cycles. Aluminum, on the other hand, does normally not experience a fatigue limit and therefor the SN-curve will gradually decrease until failure at low stresses. Usually for metals without a fatigue limit, the limit is chosen to be at $5 \cdot 10^8$ cycles. As an approximation, the fatigue limit of aluminum can be calculated as 1/3 of the yield strength [20].

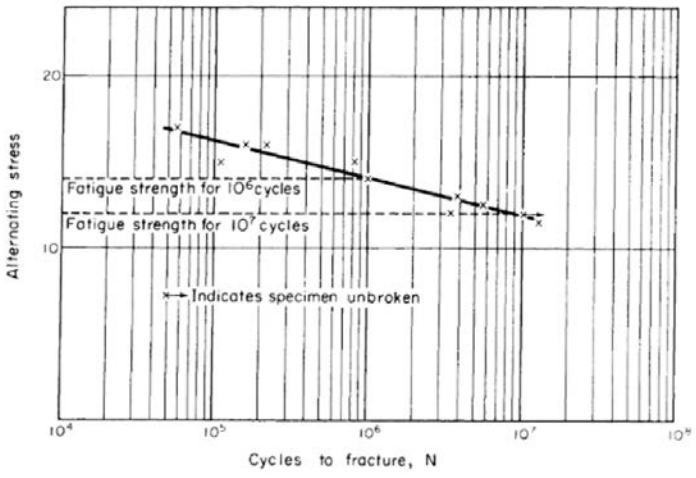

Figure 2.37: example of SN curve.

The stress plotted in the S-N curve is usually the alternating stress (σ_a) from the fatigue stress cycle, described in Figure 2.38. The S-N curve is also plotted for one fixed value of stress ratio (R), amplitude ratio (A) or the mean stress (σm). The mean stress is one half the stress range (σ_r).

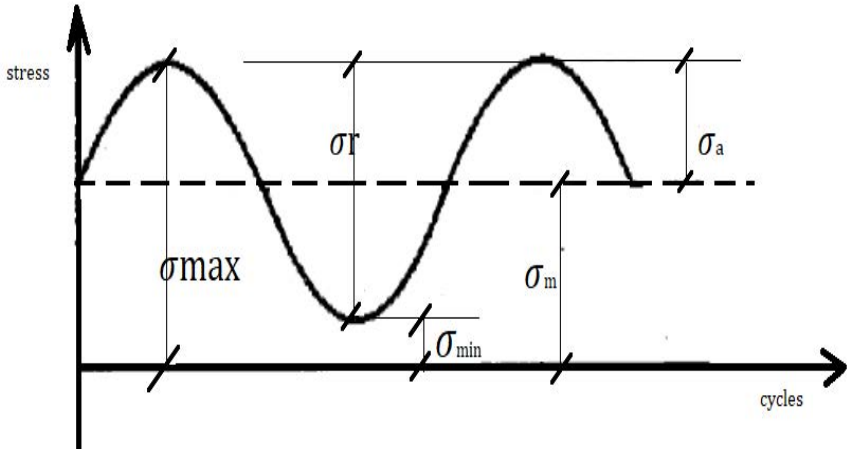

$$\sigma_r = \sigma_{max} - \sigma_{min}$$

$$\sigma_a = \frac{\sigma_r}{2}$$

$$\sigma_m = \frac{\sigma_{max} - \sigma_{min}}{2}$$

$$R = \frac{\sigma_{min}}{\sigma_{max}}$$

$$A = \frac{\sigma_a}{\sigma_m}$$

Figure 2.38: Schematic example of cyclic load applied in the fatigue test.

The stress ratio (R) indicates what type of fatigue test has been done. In our case a stress ratio R=0,1 has been chosen.

The SN-curve during high cycle fatigue may be described by the Basquin equation:

$$\sigma_a^k N = cost \tag{9}$$

Where N is number of cycles, σ_a is the stress amplitude, and k and C are empirical constants.

2.6 Types of fracture

The types of fractures that will be discussed in this subchapter are: brittle, ductile and fatigue fractures. The most accurate way of defining a fracture is to study the fracture surface and then decide the fracture type depending on features on the fracture surface [21].

2.6.1 Ductile fracture

Ductile fracture results from the application of an excessive stress to a metal that has the ability to deform permanently, or plastically, prior to fracture. Thus, the property of ductility

is simply the ability of the material to flow or deform, which may or may not lead to fracture, depending on the magnitude of the stress applied [22].

The property of ductility is somewhat related to the property of toughness, although the latter is usually measured in the presence of a notch or other stress concentration. The Charpy V-notch impact test is commonly used as a measure of toughness. However, the ability to absorb energy and deform plastically prior to fracture is characteristic of both ductility and toughness. This ability to absorb energy is a valuable property of ductile metals.

It is on a microscopic scale that the characteristics of ductile deformation and fracture really become unique.

The actual fracture surface of a ductile metal is essentially nothing but a mass of dimples, or half voids, which usually can be seen only with the aid of an electron microscope: this is termed a dimpled-rupture fracture surface, as shown in Figure 2.39. Examination of these dimples is exceedingly useful in studying fractures because the dimples are extremely sensitive to the direction of the stresses that formed them.

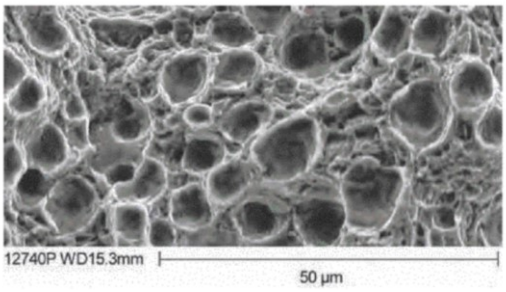

Figure 2.39: Typical dimpled-rupture fracture surface of a ductile metal viewed with a scanning electron microscope at a magnification of 1000x.

Dimple shapes have been studied extensively and are shown schematically in the following figure (Figure 2.40):

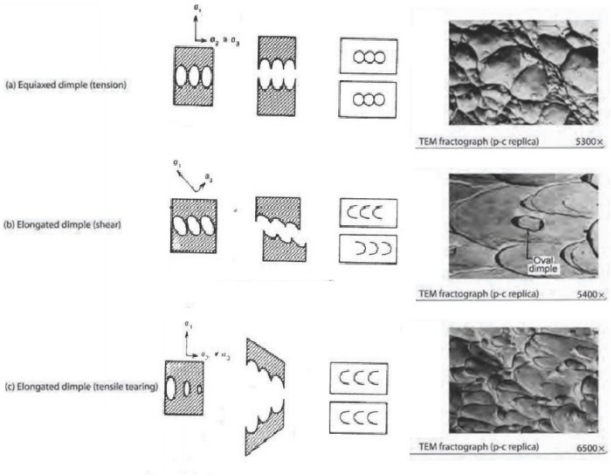

Figure 2.40: The influence of the direction of principal normal stress on the shape of dimples formed by micro void coalescence.

1. Tension.

As shown in Figure 2.40(a), the tensile force at the center of the specimen causes micro voids first to form near the center and then to spread to nearby areas that must then carry more stress because the cross section is now smaller in area. Under an axial force as shown, the micro voids are not skewed, or tilted, in any particular direction; thus, the fracture surface consists of equiaxed dimples when viewed perpendicular to the surface. The angle of view is particularly important when the dimples are studied in a scanning electron microscope; if they are viewed from an angle, they can appear foreshortened and not equiaxed.

2. Shear.

As shown in Figure 2.40(b), the dimples become elongated at a pure shear fracture surface, such as that of a torsional fracture of a ductile metal. The dimples can become so elongated that they no longer closely resemble dimples except for their C-shaped ends. Also note that the "C" shapes are in opposite directions on the opposed fracture surfaces because each represents one end of a dimple that was pulled in opposite directions. On torsional fractures, these dimples are frequently damaged by rubbing from the opposite sides so that the surface observed is simply a mass of circular rub marks. (These marks must not be confused with fatigue striations).

3. Tensile Tearing.

As shown in Fig. 2.40(c), this mechanism of fracture is somewhat similar to the pure tension mechanism shown in Fig. 2.40(a) except that the fracture actually originates at the edge of the metal rather than at the center. This is due to a bending force on the part that causes tensile

fracture with equiaxed dimples at the region close to the origin, while the actual tensile tearing causes the C-shaped dimples to form near the end of the fracture, opposite the origin.

At this point, it is prudent to insert some cautions about interpretation of the evidence visible with this type of microscopic examination. The analyst must be aware of complicating factors extraneous to the fracture itself. For instance, in certain metals, cuplike cavities may be present on a fracture surface, but the cavities may not be the dimples characteristic of ductile fracture. In cast metals and weldments, particularly, this type of rounded cavity may be evidence of gas porosity. Gas porosity occurs because the inevitable gases in castings and weldments cannot escape to the atmosphere before the metal solidifies and traps the gas in the metal. This is particularly true in weldments in metals such as aluminum, which has a high rate of thermal conductivity. In effect, large, cold members having high thermal conductivity act as heat sinks, causing rapid solidification of the weld metal and entrapping gas bubbles before they can escape. In ductile fractures of metals with extensive gas porosity, it may be quite difficult to determine which cavities are true dimples and which are evidence of gas porosity.

2.6.2 Brittle fracture

Brittle means little or no permanent deformation prior to fracture, usually accompanied by high hardness and strength but with little tolerance for discontinuities. A brittle fracture occurs at stresses below the material's yield strength.

On a macroscopic scale, a brittle fracture has a bright or shiny surface. For the failure analyst, distinguishing between macroscale ductile and brittle fractures is an important first step in identifying the failure mechanism. Fractures accompanied by gross deformation (ductile fracture) are caused by one of three possible failure mechanisms: monotonic ductile overload, very low cycle fatigue, or stress rupture. In contrast, fracture in the absence of gross deformation (brittle fracture) is caused by either: (1) high cycle fatigue; or (2) monotonic overload of an inherently brittle material or of an embrittled, normally ductile material. Embrittlement may be due to conditions such as high constraint as caused by thick sections, sharp notches and cracks, or crack-like imperfections; low temperature; high strain rate or impact; improper heat treatment; and/or environmental embrittlement. Brittle fractures, rather than ductile fractures, are more often the subject of a failure investigation, because they are often sudden, unexpected, and sometimes catastrophic.

Brittle fractures usually propagate by either or both of two fracture modes, cleavage or intergranular. In most cases it is necessary to study the fracture surface with a scanning electron microscope to distinguish the fracture mode.

Cleavage fractures are characterized by splitting of the crystals, or grains, along specific crystallographic planes without respect to the grain boundaries, as shown in Figure 2.41. Since the fracture goes through the grains, this type of fracture is frequently referred to as transgranular. Cleavage fractures are the most common type of brittle fracture and are the normal mode of fracture unless the grain boundaries have been weakened by a specific environment or process.

A typical cleavage fracture viewed by the scanning electron microscope is shown in the following Figure 2.41.

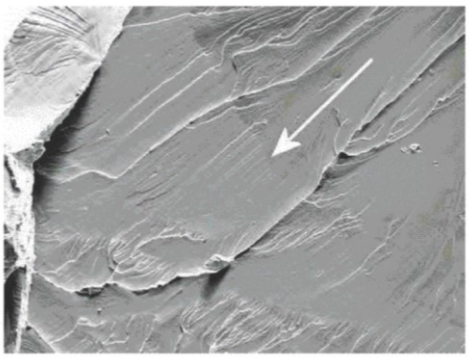

Figure 2.41: Cleavage fracture in hardened steel showing numerous "river" marks. The overall direction of crack propagation is in the direction of the arrow. New river patterns are created where grain boundaries were crossed. Magnification 125x. [23].

Intergranular fractures are those that follow grain boundaries weakened for any of several reasons. An analogy may be made to a brick wall, which fractures through the mortar rather than through the bricks them-selves. The mortar is analogous to the grain boundaries, while the bricks are analogous to the metal grains. In steels, intergranular fracture follows the prior austenite grain boundaries. A typical intergranular fracture is shown in the following Figure 2.42.

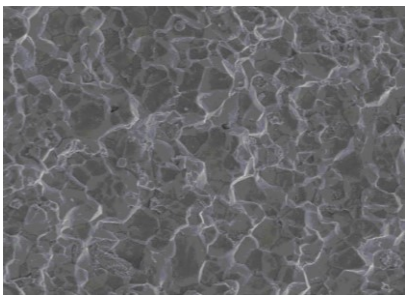

Figure 2.42: 14 Intergranular fracture viewed under the scanning electron micro scope. Note that fracture takes place between the grains; thus, the fracture surface has a "rock candy" appearance that reveals the shapes of part of the individual grains. [23]

2.6.3 Fatigue fracture

Many submicroscopic changes take place in the crystalline structure of the metal under the action of relatively low-level, repetitive load applications. These little changes in the structure, may progress gradually to form tiny cracks that may grow to become large cracks under continued cyclic loading, and that can then lead to fracture of the part or structure. Once initiated, the fatigue fracture can propagate by high stresses and low cycles or by low stresses and high cycles. The final rupture may have characteristics of brittle and/or ductile fracture modes, depending on the metal involved and the circumstances of stress and environment. This suggests that there are three stages of fatigue fracture: initiation, propagation, and final rupture (overload) [23].

Striations are the most characteristic microscopic evidence of fatigue fracture, although interpretable striations are not always present on fatigue fracture surfaces.

In the following figure (Figure 2.43) a schematic cross-sectional sketch of stage 1 and stage 2 of the fatigue fracture is shown.

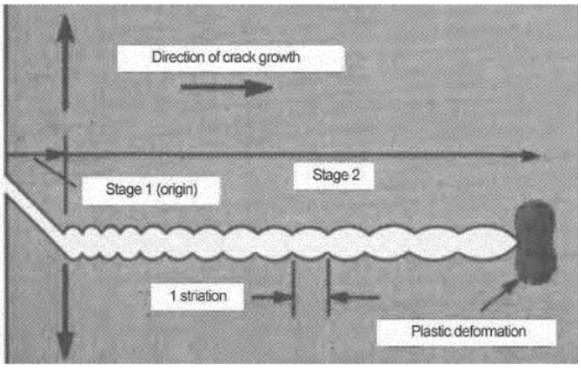

Figure 2.43: highly enlarged schematic cross-sectional sketch of stage 1 and stage 2 fatigue. The edge of the metal is at left. When tensile forces repeatedly act on the surface, the microstructural changes of stage 1 cause a submicroscopic crack to form. With each repetitive opening, the crack jumps a small distance (one striation). Note that the spacing of each striation increases with the distance from the origin, assuming the same opening stress. The metal at the tip of the fatigue crack (right) is plastically deformed on a submicroscopic scale. [24].

When a crack reaches a certain length and the cross section no longer can support the load, failure will occur. Hence, the ultimate failure occurs rapidly.

3 Experimental

3.1 Materials

3.1.1 Parent material

In the experimental process of this work, 4 mm extruded plates of aluminum alloy 6082, received in the T6 tempered condition, were used. The chemical composition of the base metal is shown in Table 3.1. The parent material certificate can be found in Appendix.

Table 3.1:Chemical composition of AA6082 used as parent metal.

Si (%)	Fe (%)	Cu (%)	Mn (%)	Mg (%)	Cr (%)	Zn (%)	Ti (%)	Al (%)
0.97-1.00	0.20-0.21	0.02-0.03	0.47-0.48	0.63-0.64	0.00-0.01	0.00-0.01	0.02	Balance

3.1.2 Filler material

The filler material used in the GMAW process was a 1.2 mm diameter wire of the AA5183 type, with chemical composition as shown in Table 3.2. The material certificate can be found in Appendix.

Table 3.2: Chemical composition of the AA5183 used as a filler material.

Chemical composition limit (%)									Unspecified elements	
Si	Fe	Cu	Mn	Mg	Cr	Zn	Ti	Zr	Each	Total
0.40	0.40	0.10	1.00-0.50	5.20-4.30	0.25-0.05	0.25	0.15	-	0.05	0.15

This choice comes from the wanted properties which are reached using the 5183 as the filler material for the AA6082 in the GMAW process. As shown in the Table in Appendix, this choice gives the following properties:

- Excellent strength;
- Excellent ductility;
- Excellent color match;
- Good cracking resistance;
- Good toughness;
- Good corrosion resistance.

3.1.3 Joining conditions

A schematic drawing of the plates during the welding is shown in the following Figure 3.1.

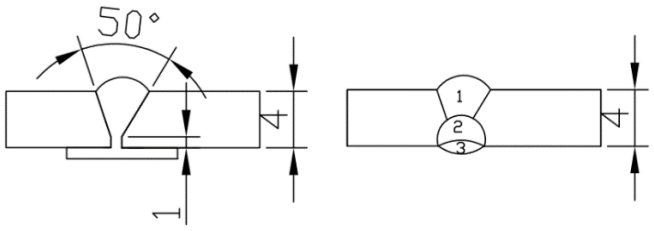

Figure 3.1: Schematic illustration of the plates during the welding process.

The weld deposition was carried out at LEIRVIK with AA5183 as filler wire. Welding parameters can be found in the following Table 3.3.

Table 3.3: Welding parameters used in GMAW of AA6082.

Plate code	Elec. Dim	Amps Min-max	Volt Min-max	Heat input [KJ/mm]	Gas Flow Shield [l/min]
1b	1.2	180	22	0.43	20
2b	1.2	165	22.2	0.3	20

3.2 Sample preparation

Samples were cut transverse to the welding/rolling direction and numbered, as illustrated in the following Figure 3.2.

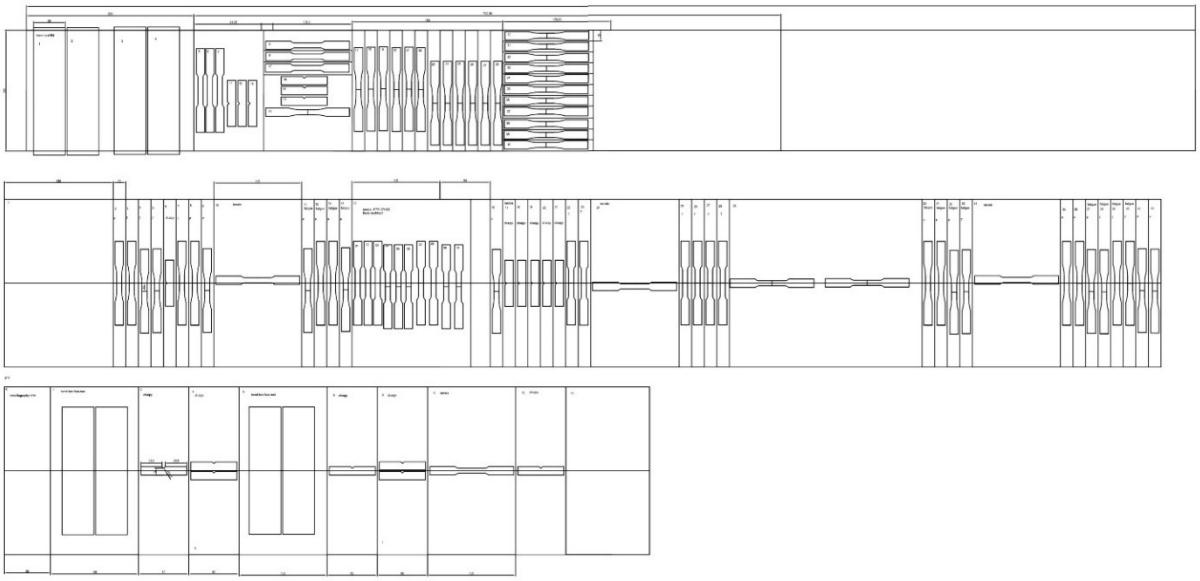

Figure 3.2:Schematic illustration of sample sectioning and numbering of specimens.

A total of one hundred specimens have been obtained from the plates. The bend test samples were cut to a width of approximately 45mm and then machined with a milling machine to the final width. The other samples were first cut to a width of 15mm and then, using a milling machine, they have been machined down to 10 mm. From the rectangular shape obtained, they were machined to the final geometries using a CNC machine. The metallographic samples were cut to a width of 15mm and then prepared to be polished.

3.2.1 Optical microscopy

The samples used for the microstructural investigation have been obtained cutting the plates into samples in which the weld zone was centered.

After cutting the samples were cold mounted in a ClaroCit acryl resin. The mounted samples were then ground using SiC grinding paper of increasing fineness (P80, P120, P220, P500, P1000, P2000 and P4000). Water was used as lubricant. In between each grinding step, the samples were rinsed in water and then ethanol.

The grinding process was followed by the polishing one, using 3 μm and 1 μm polishing disks and diamond paste suspensions. DP-Lubricant Blue was used as lubricant. After polishing, the samples were cleaned using an ultrasonic ethanol bath.

The ground and polished samples used for the microstructural examination were immersed in an alkaline sodium hydroxide solution ($1g\ NaOH$ + $100ml\ H2O$). The holding time was 3 to 4 min. Then the samples were ready for examination in the optical microscope. The analysis in the optical microscope was done using a Leica DMLB light microscope and an Alicons Confocal Microscope.

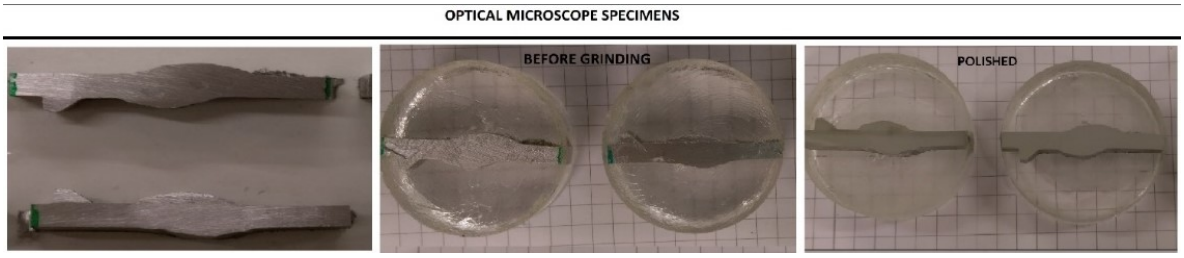

Figure 3.3: samples prepared for the optical microscope.

3.2.2 Hardness testing

Vickers hardness tests has been found to be very useful for materials evaluation, quality control of manufacturing processes and research and development efforts. Hardness, although empirical in nature, can be correlated to tensile strength for many metals, and is an indicator of wear resistance and ductility. The Vickers hardness (HV) was measured on one sample. To ensure that the complete HAZ degradation could be revealed, a total length of 150 mm have been kept. A total of three different test series were conducted. In-between each test series, the sample was ground and polished before the next one. The grounding and polishing procedure is the same described for the optical microscope samples. The base metal hardness was measured from ten individual measurements being randomly taken on a specimen of the unaffected parent material.

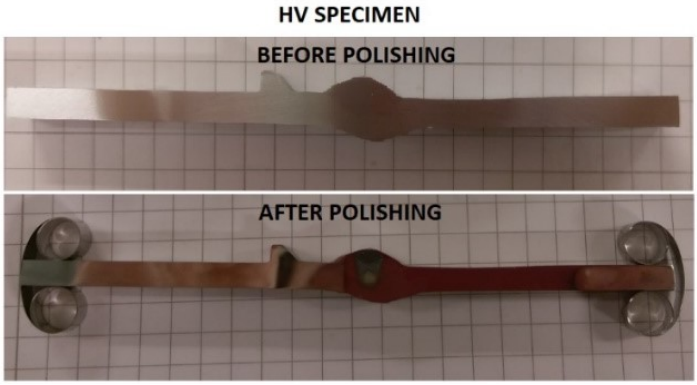

Figure 3.4:samples prepared for the HV measurement.

The hardness measurements were made using a Mitutoyo Micro Vickers Hardness Testing Machine (HM-200 Series) using a load of 1 kg (Figure 3.5). The ideal Vickers indenter is a highly polished, pointed, square-based pyramidal diamond with face angles of 136°. Following the recommendation in the standard (Figure 3.5), the distance between each indentation was 0.5 mm, and the full test force was applied for 10 seconds. All these hardness measurements are in accordance with the ASTM E92-16 standard [25].

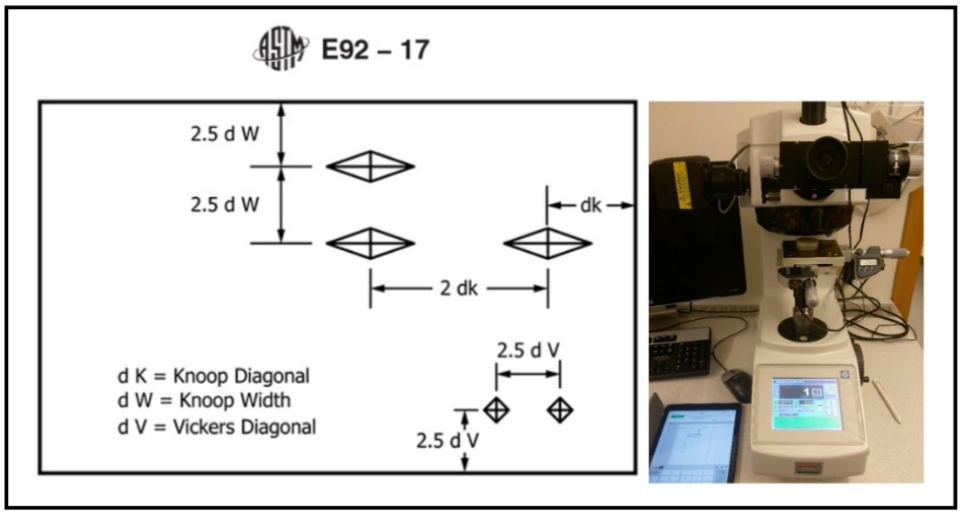

Figure 3.5: On the left: Minimum Recommended Spacing for Vickers and Knoop Indentations. On the right: Mitutoyo Micro Vickers Hardness Testing Machine (HM-200 Series).

The Vickers hardness number, in terms of indentation test forces in Newtons (N) and indentation diagonals measured in millimeters (mm), is calculated as follows:

$$HV = 0.1891 * \frac{F[N]}{d_v^2[mm]} \quad (10)$$

In our case, this formula is already implemented in the testing machine.

3.2.3 Bend testing

Bend test has been carried out following the NS-EN ISO 5173:2010 standards [26]. In the three-point bend test the specimen is bent in a U-shaped die by means of a centrally applied force to the weldment in a flat specimen supported at two positions equidistant from the line of force application (Figure 3.6). The specimen is forced into the die by a plunger having the shape necessary to produce the desired contour. The convex surface of the bent specimen is examined for cracks or other open flaws. The guided bend test is used to evaluate the quality of welds as a function of ductility as evidenced by their ability to resist cracking during bending. The types of specimens generally used for guided bend testing are rectangular ones machined from plates and pipes. In this case, rectangular specimens from plates have been tested (Figure 3.6). The measures of the specimens and the radius of the rollers are shown in the following figure (Figure 3.6). The weld-face surface of the flat specimen contains the greater width of the weld material, while the opposite side is called the weld-root surface.

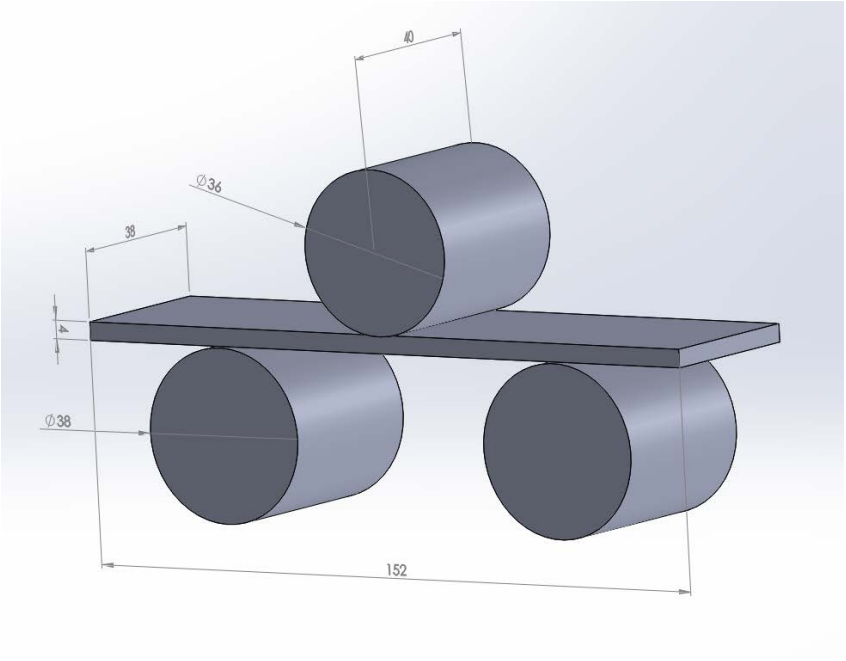

Figure 3.6: Schematic representation of the three-point bend test.

The procedure consists in bending the guided-bend specimens in a test jig. Before start bending is necessary to place transverse specimens on the die member of the jig with the weld at midspan. Place face-bend specimens with the weld face directed toward the gap. Place root-bend specimens with the weld root directed toward the gap. A great amount of grease has been used between the rollers and the specimen. After bending, examine the convex surface of the bent specimento check if there are any cracks or other open flaws. The test has been conducted for informational purposes. The tests have been stopped in case of cracks propagated though the whole thickness or at the end of the plunger stroke.

The bend test has been done using a MTS 809 Axial/TorsionalTest System, setting the speed of the plunger to 1mm/min.

Figure 3.7: Bend test set-up.

The total number of specimens used in the bend test can be found in the following Table 3.4.

Table 3.4: Total number of bend specimens machined from the welded and the parent material plates.

Specimen Location	Number of specimens
Fused Zone Face	2
Fused Zone Root	2
Parent material Transverse	4
TOT	**8**

3.2.4 Tensile testing

Tensile test has been carried out following the ASTM E8/E8M − 16a standards [27]. Tension tests provide information on the strength and ductility of materials under uniaxial tensile stresses. This information may be useful in comparisons of materials. As can be seen in the following table, the specimen dimensions chosen are the ones for the "subsize specimen".

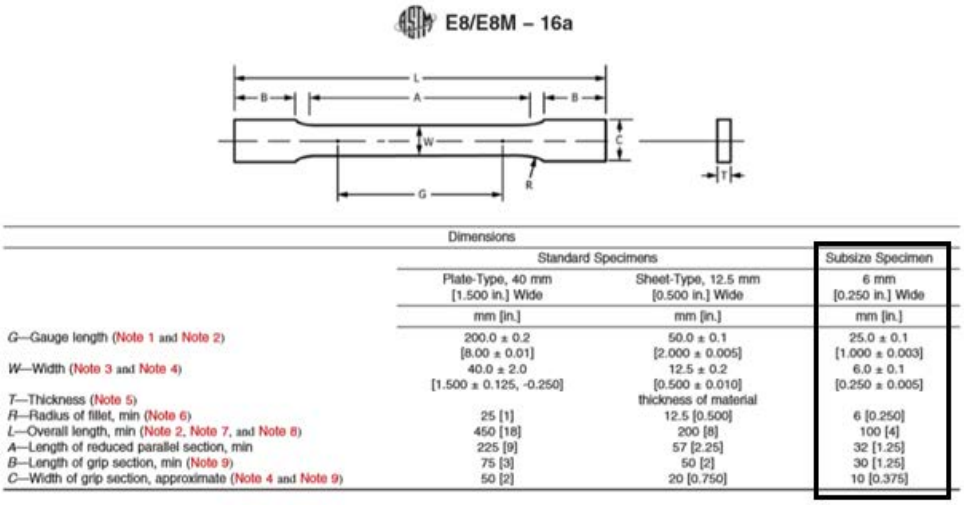

Dimensions	Standard Specimens		Subsize Specimen
	Plate-Type, 40 mm [1.500 in.] Wide	Sheet-Type, 12.5 mm [0.500 in.] Wide	6 mm [0.250 in.] Wide
	mm [in.]	mm [in.]	mm [in.]
G—Gauge length (Note 1 and Note 2)	200.0 ± 0.2 [8.00 ± 0.01]	50.0 ± 0.1 [2.000 ± 0.005]	25.0 ± 0.1 [1.000 ± 0.003]
W—Width (Note 3 and Note 4)	40.0 ± 2.0 [1.500 ± 0.125, -0.250]	12.5 ± 0.2 [0.500 ± 0.010]	6.0 ± 0.1 [0.250 ± 0.005]
T—Thickness (Note 5)		thickness of material	
R—Radius of fillet, min (Note 6)	25 [1]	12.5 [0.500]	6 [0.250]
L—Overall length, min (Note 2, Note 7, and Note 8)	450 [18]	200 [8]	100 [4]
A—Length of reduced parallel section, min	225 [9]	57 [2.25]	32 [1.25]
B—Length of grip section, min (Note 9)	75 [3]	50 [2]	30 [1.25]
C—Width of grip section, approximate (Note 4 and Note 9)	50 [2]	20 [0.750]	10 [0.375]

Figure 3.8: Dimensions for tensile specimens.

The specimens have been cut from these different locations, transverse or longitudinal to the welding direction, to generate specific data for the different weld regions. For the welded ones, two different types of specimens have been tested: one type maintaining the reinforcement, one type machining it. The number and the labelling of the tensile specimens (for further use in the results), can be found in the following Table 3.5.

Table 3.5: Total number of tensile specimens tested.

Specimen Code	Number of specimens
Parent material Transverse	3
Parent material Longitudinal	3
Fused Zone Transverse	3
Fused Zone Longitudinal	3
HAZ Transverse	3
HAZ Longitudinal	3
FZ Machined	3
HAZ Machined	3
TOT	**24**

In the following figure (Figure 3.9) are shown the tensile specimen geometry and the schematic representation of a welded plate from where the specimens have been obtained.

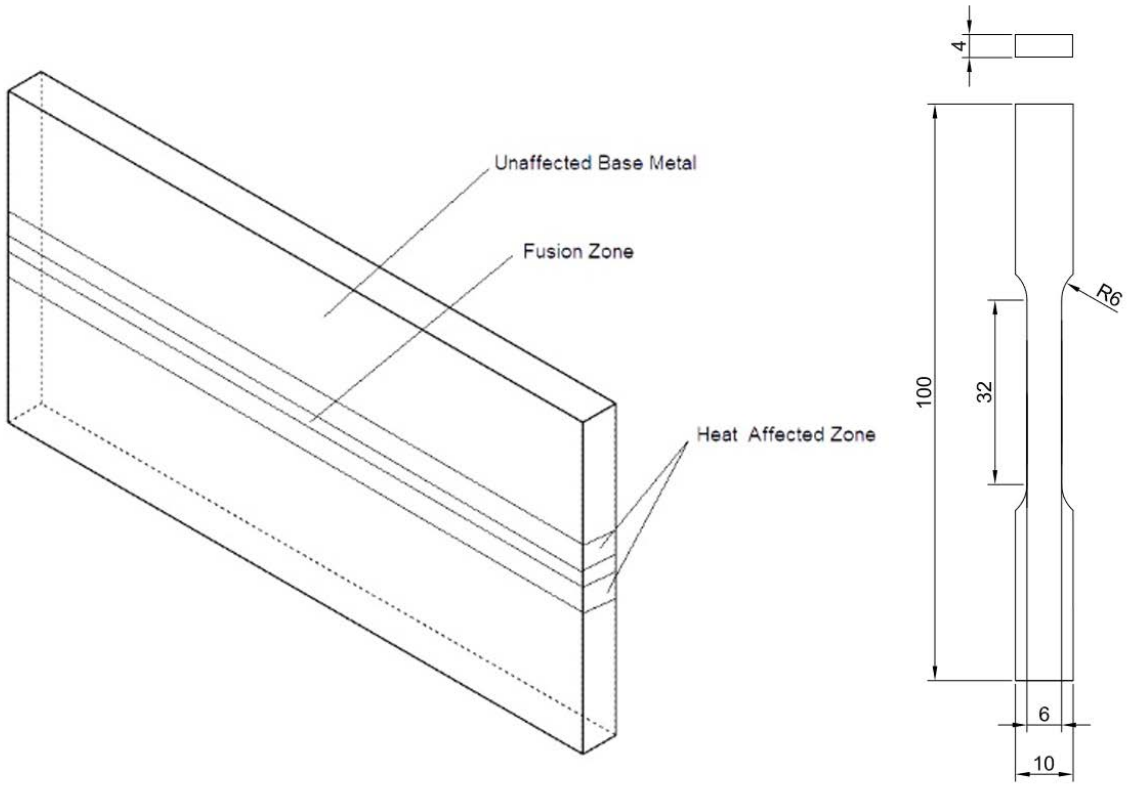

Figure 3.9:Plate zones and basic dimensions of the tensile test specimens.

The Fused Zone specimens have been machined placing the welded part in the center of the specimen. For the HAZ specimens, the center have been chosen using the data of the hardness test, placing the weakest part of the specimens in the center. The tests were done in a MTS servo-hydraulic tensile machine at SINTEF in Trondheim, Department of Materials Testing. The axial elongation was measured using an extensometer with 25 mm gauge length. The cross-head speed was fixed to v = 1.5 mm/min, which corresponds to a strain rate of $\dot{\varepsilon}_{nom}$ = $10^{-3}\ s^{-1}$. The basic dimensions of the tensile test specimens are shown in Figure 3.9.

3.2.5 Fatigue testing

Fatigue test has been carried out following the ASTM E466 – 15 standards. The axial force fatigue test carried out is used to determine the fatigue resistance of the material subjected to direct stress for relatively large numbers of cycles. The results may be used as a guide for the selection of metallic materials for service under conditions of repeated direct stress. This information may be useful in comparisons of materials. The practice used covers the procedure for the performance of axial force-controlled fatigue tests to obtain the fatigue strength of metallic materials in the fatigue regime where the strains are predominately elastic, both upon initial loading and throughout the test. The practice is limited to the fatigue testing of axial unnotched and notched specimens subjected to a constant amplitude, periodic forcing function in air at room temperature. The specimen dimensions are shown in the following figure (Figure 3.10).

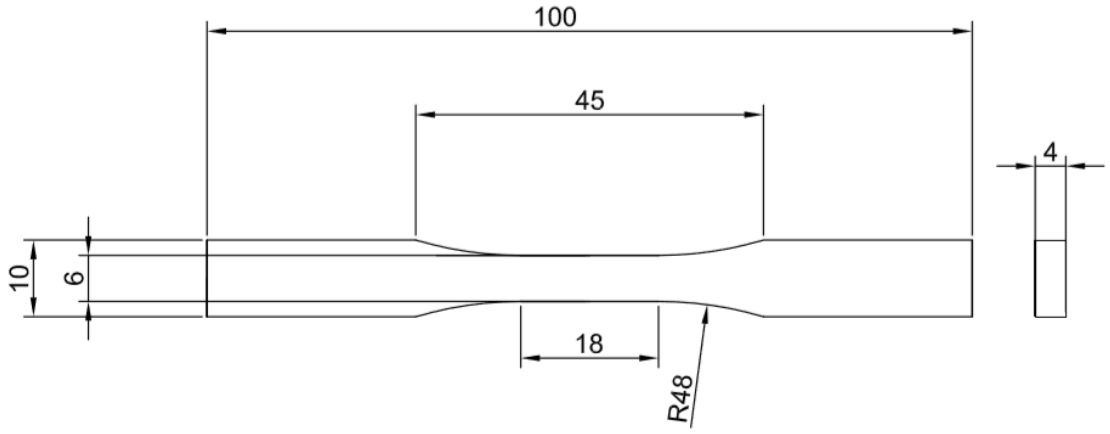

Figure 3.10: Fatigue specimen geometry in accordance to the standard indications.

The specimens have been cut from the parent material both longitudinal and transverse to the extrusion direction. The welded specimens have been taken in two different ways: one centering the welding, one centering the weakest part of the plate (basing on the tensile and hardness tests results). For all the fatigue specimens, the reinforcements have been taken. The number and the labelling of the fatigue specimens (for further use in the results), can be found in the following Table 3.6.

Table 3.6: Total number and codes of fatigue specimens tested.

Specimen Code	Number of specimens tested
BML	12
BMT	12
FZ	12
HAZ	12
TOT	**48**

The ratio chosen for the tests is R=0,1. In order to obtain a S-N curve, the stresses have been calculated on the base of the tensile tests results. The stress amplitude range used goes from 112 MPa to a minimum of 40 MPa. Considering the stress chosen, knowing the measure on each specimen, the forces have been set on the fatigue machine. The fatigue machine used is a MTS Landmark (Figure 3.11). The frequency chosen for the tests is 10Hz as it is the maximum that the hydraulic machine used can reach.

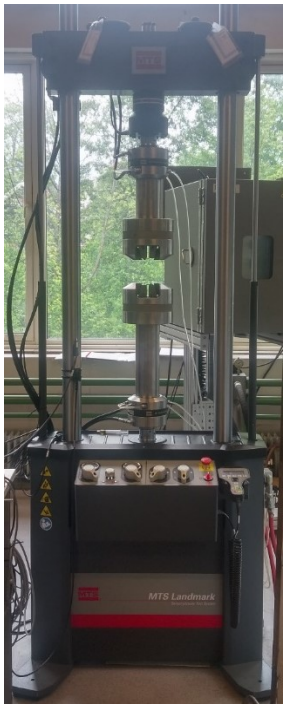

Figure 3.11: MTS Landmark machine used for the fatigue test.

3.2.6 Impact testing

Impact data was collected using the Charpy V-notch test. This test has been carried out following the ASTM E23 – 16b standards [28]. This test was used to get information about the energy absorbed during impact. The Charpy specimens were prepared for the base metal, fusion zone and HAZ in the same direction and orientation as the tensile test specimens. In the following table the different codes and types of specimens taken are summarized.

Table 3.7: Total number and codes of Charpy specimens tested.

Specimen Code	Number of specimens tested
BMT	3
BML	3
FZL	3
FZT	3
HAZL	3
HAZT	3
TOT	**18**

The machine used for the impact Charpy test is a Zwick/Roell RKP450 (Figure 3.12). The tests were done at SINTEF in Trondheim, Department of Materials Testing.

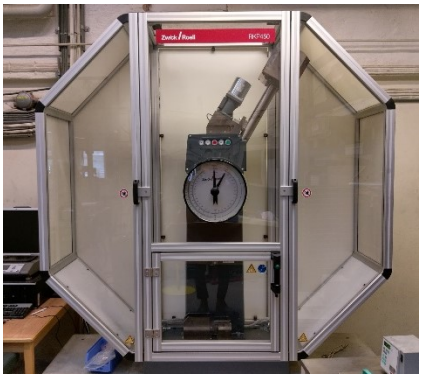

Figure 3.12: Machine used for the impact test.

The dimensions and the geometry of the specimens have been chosen to obtain straight specimens for all the types. The basic dimensions of the Charpy test specimens are shown in the following figure (Figure 3.13). The 2.5 mm thikness has been chosen because the welded plates were distorted, and in the transverse case, mantaining the original thikness of the plates brought to a not straight specimen. The specimens have been machined with a milling machine and the notch has been made at SINTEF.

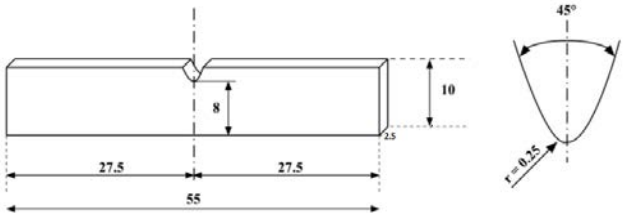

Figure 3.13: basic dimensions of the Charpy test specimens.

3.2.7 Fracture surface analysis in the Scanning Electron Microscope (SEM)

The fracture surface of selected tensile and fatigue test specimens was examined in the scanning electron microscope (SEM). The microscope was a Quanta FEG 450. The fracture surface examinations were performed with an acceleration voltage of 20 kV or 30 kV. The working distance and aperture was set to approximately 10 mm and 30 µm, respectively.

4 Results

In this chapter, all the results from the experimental tests will be presented.

4.1 Optical micrographs of the metal

The following figure is an overview of the welded joint. This picture has been taken with a confocal microscope. The magnification used is 5x. To analyze the microstructure of the different zones, a greater magnification is necessary. In the following figure are shown the different zones from which the pictures have been taken.

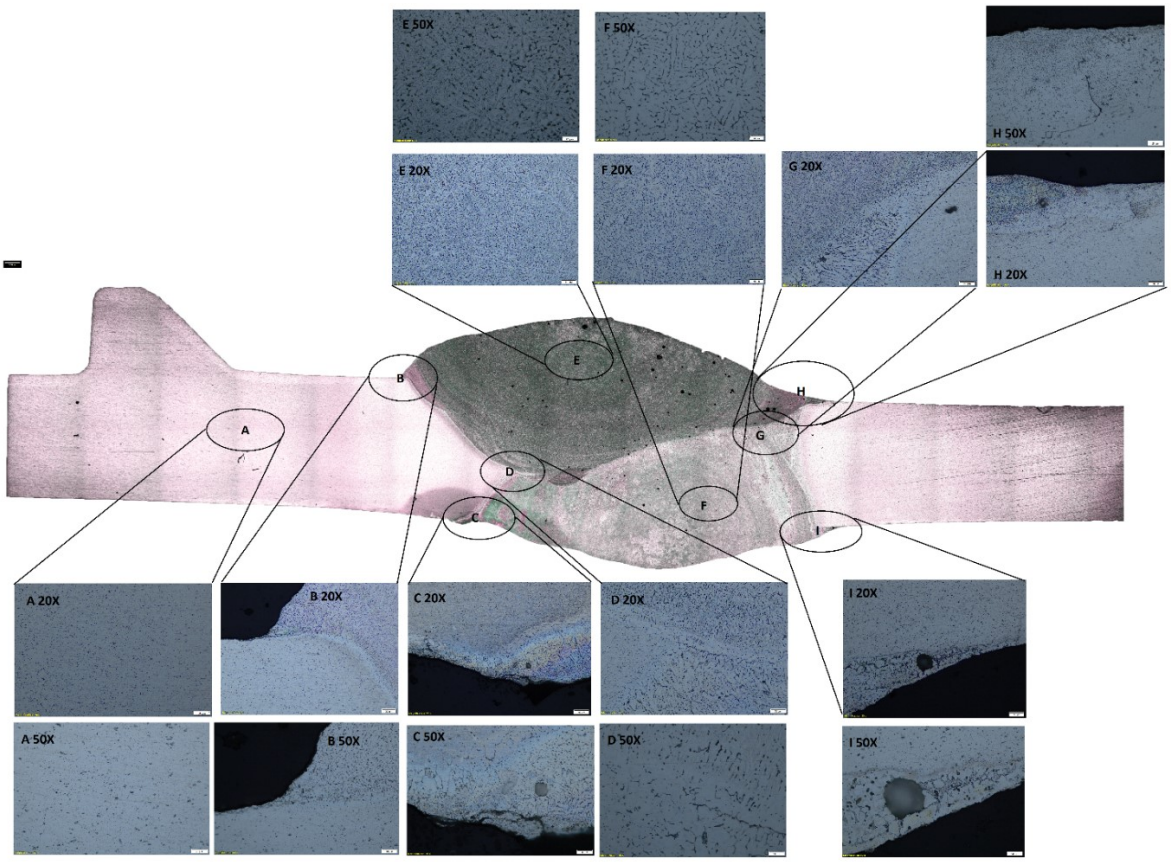

Figure 4.1: overview of the weldment made using the confocal microscopy.

To compare the microstructure of the different zones, the following pictures have been chosen (A, E, F).

From the analysis of the Figure 4.1 it has been calculated that the percentage of area covered by pores is approximatively 0,5%. This value is less than the 3% indicated in the standard for this kind of welding.

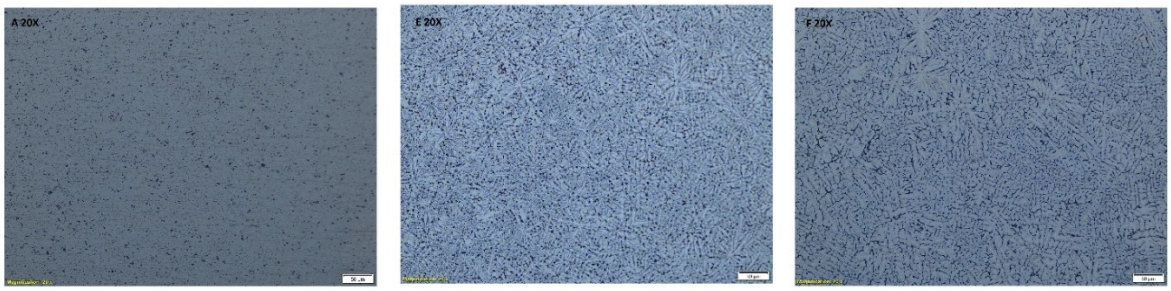

Figure 4.2: from the left to the right: HAZ, FZ upper part, FZ lower part. Magnification 20X.

As can be seen in the previous Figure 4.2, the grain dimensions are different. In the fused zone the grains are bigger than in the parent material and consists of equiaxed dendritic grains with different orientations.

4.2 Hardness test

The method used was the Vickers one, which employs the diamond pyramid indenter with vertex angle between opposite sides of 136 °. In the following figure is shown the appearance of the indentation during the measuring of the diagonals.

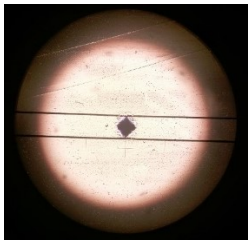

Figure 4.3:Vickers indentation appearance during the hardness test.

The following Figure 4.4 shows the resulting hardness profile for the GMA weldments. To make clearer the hardness trend, the hardness profile is linked to a macro image of the hardness specimen. The parent material hardness was measured, and the value is 105 HV.

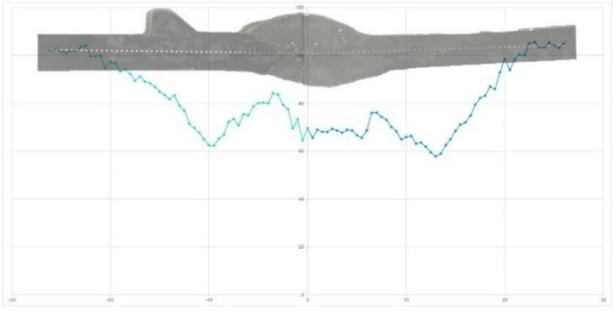

Figure 4.4: Hardness profiles for the GMA weldment, including a macro image of the hardness specimen.

In Figure 4.4 it is possible to notice the M-shape, typical of this type of junctions. The reduction of the HV value, confirms the presence of a super-aging (coalescence of β' or β phases) of the alloy that has reduced its mechanical performance. Considering the hardness profile, the minimum HAZ hardness value can be found around 12 mm from the center of the weld on both sides. The minimum HAZ hardness was measured to 61 and 58 HV, respectively. In addition, a small drop in hardness can observed at the fusion line. Full recovery of the base metal hardness is observed approximately 22 mm from the center of the weld. All the individual hardness measurements can be found in Table 8.8 in the Appendix.

4.3 Bend test

The goal of the tests was to understand if the weld preserved enough ductility to be bent without the onset of cracks on the specimen. In the following figures (Figure 4.5, Figure 4.6) are shown some pictures taken at different stages of the tests: the first picture shows the parent material, in which the crack started to propagate very soon, the second picture shows the results of bending a welded specimen.

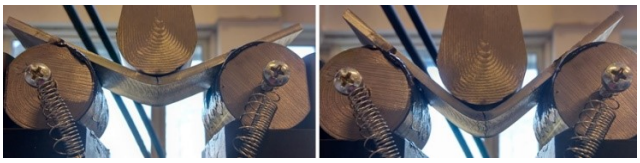

Figure 4.5: Bending of the parent material.

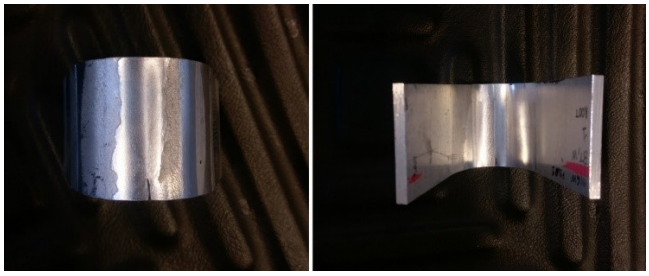

Figure 4.6: Fused zone specimens after bending.

As can be seen, the welded specimens appear to be more ductile, since the crack is not visible. This result will also be confirmed with the tensile and Charpy tests.

In the following graphs, the force and the displacement of the plunger are plotted. For a better quality of the following plots see the Appendix.

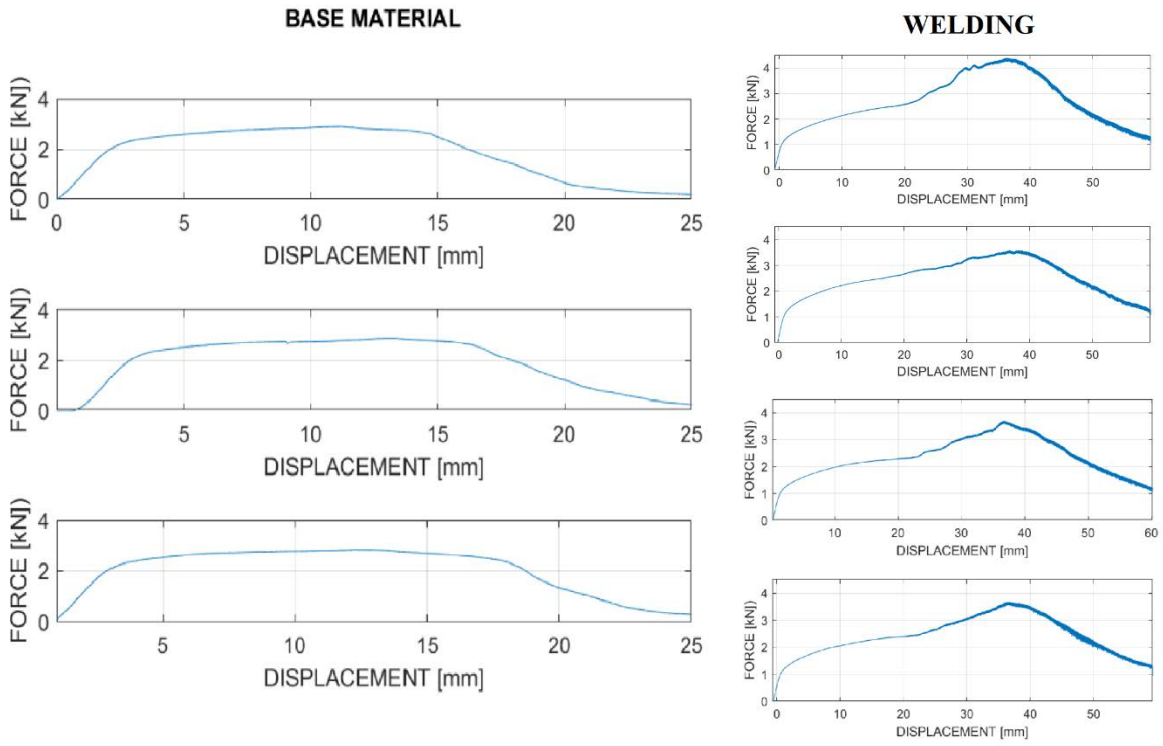

Figure 4.7: Force vs Displacement in the bend test. On the left: Force vs Displacement in the parent material; on the right: Force vs Displacement in the welded specimens.

As can be seen in the plots, the force in the parent material tests goes down to zero, that is because the crack propagated through the whole thickness of the specimens. On the right, the plots for the welded specimens show that the force does not go down to zero, and the test was stopped not because of the braking of the specimen but because the maximum displacement was reached.

4.4 Tensile test

Tensile test results have been analyzed using Microsoft Excel. As explained in the experimental chapter, the tensile specimens have been cut from the base metal (BM), the fusion zone (FZ) and the heat-affected zone (HAZ), both transverse (T) and longitudinal (L) to the welding direction. Figure 4.8 shows macro images of a selection of the BM, FZ and HAZ tensile specimens after testing.

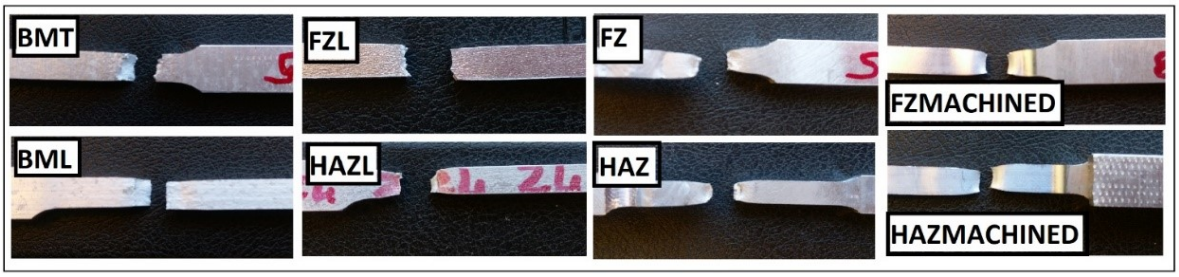

Figure 4.8: selected specimens fracture zone.

From these macro images it can be seen the different behavior of the material depending on the zones/direction tested. For example, it's clear the ductility behavior of the welded specimens, especially in the heat affected zone, where the reduction in area after testing is greater than in the parent material. From this first approach, it can be seen the brittle behavior of the fused zone tested in the longitudinal direction. This can be explained watching at the fracture surface, covered by pores, due to the welding process. Another aspect to consider is that the welded specimens have all broken in the heat affected zone, even is the fused zone was centered in the geometry. This can be easily explained considering the hardness profile, which can be related to the strength of the material: the weakest part of the specimen is in the heat affected zone, around 12mm from the center of the welding.

After a first qualitative analysis, the data from the tests have been analyzed, showing the behavior of the material, in accordance to what expected from that first analysis. In the following Figure 4.9, the resulting stress-strain diagrams are presented. All the graphs and the measures used for each specimen tested can be found in the Appendix.

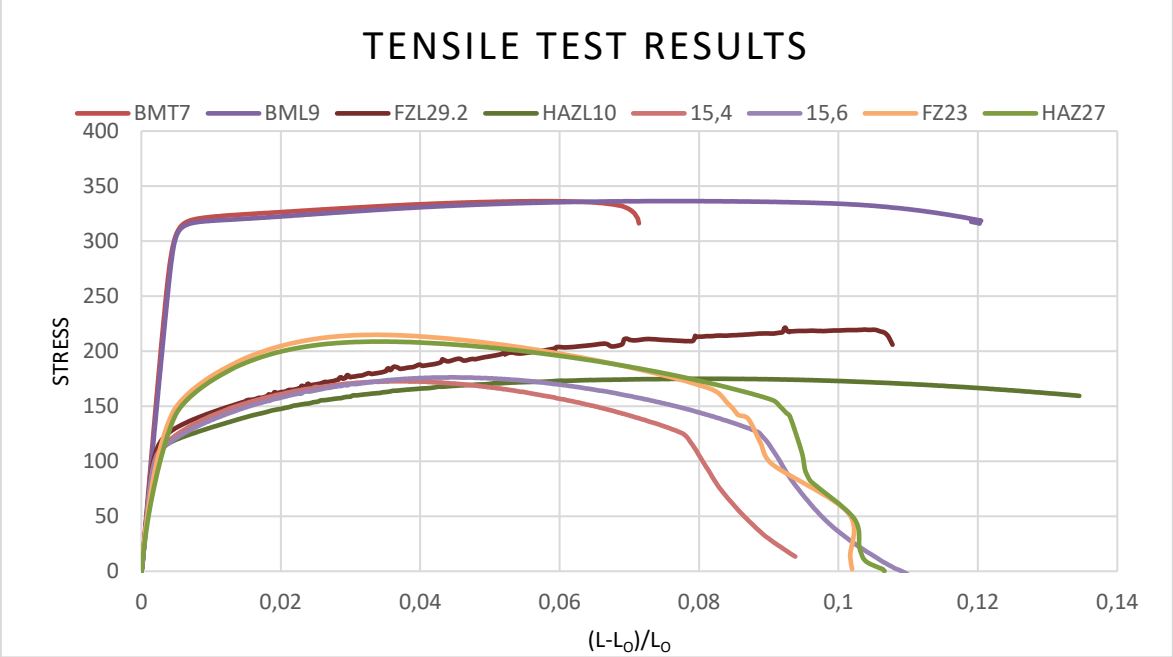

Figure 4.9: comparison between all types of specimens.

Considering the graphs above, the parent material is more ductile in the longitudinal direction (longitudinal with respect to the extrusion direction) than in the transverse one. On the other hand, the strength appears to be the same. Regarding the fused zone and the heat affected zone longitudinal specimens, the ductile behavior is also appreciable. The behavior of the welded specimens appears similar in both the machined or in the ones where the reinforcement has been taken. The small difference between those can be due to the different thickness: the machined ones have a very small thickness which can affect the behavior during the test, taking the material to a condition of plane stress. The fused zone longitudinal test results are affected from the vibrations due to the work near the laboratory which produced many vibrations during the tests.

In order to have a quick comparison between the results of the tests the following summary tables is presented.

Table 4.1:tensile test result summary table.

	E [GPa]	σ 0.2%[Mpa]	UTS [Mpa]	E MEAN [Gpa]	σ0.2% AVERAGE [MPa]	UTS AV [MPa]
BMT	70,9	318	334	70,7	317	336
	70,4	317	337			
	70,7	317	336,4			
BML	66,99	317,7	338,12	65,9	314	335
	66,69	315,8	336,24			
	64	308,9	330,49			
FZL	67,69	130,4	228,5	65,7	132	216
	64,7	140,3	221,4			
	64,78	126,1	196,7			
HAZL	60,5	116,6	219	62,8	145	210
	65,37	170,2	213			
	62,63	148	197			
FZMACH	20	110	180	64,0	115	176
	64	117,9	173,8			
	64	117,9	173,8			
HAZMACH	63,9	118,4	172,67	62,9	118	175
	63,67	117,8	176,53			
	61	116,5	176,25			
FZ	52,8	122	213	67,0	142	213
	64	160	214			
	70	144	213			
HAZ	48	153	214	54,4	141	211
	54,7	132	208,7			
	54	137	209,55			

In the welded specimens, we noticed a strong reduction in yield strength: this phenomenon is certainly related to the thermal stress that the material undergoes during welding.

In the following graphs a comparison between the results is presented.

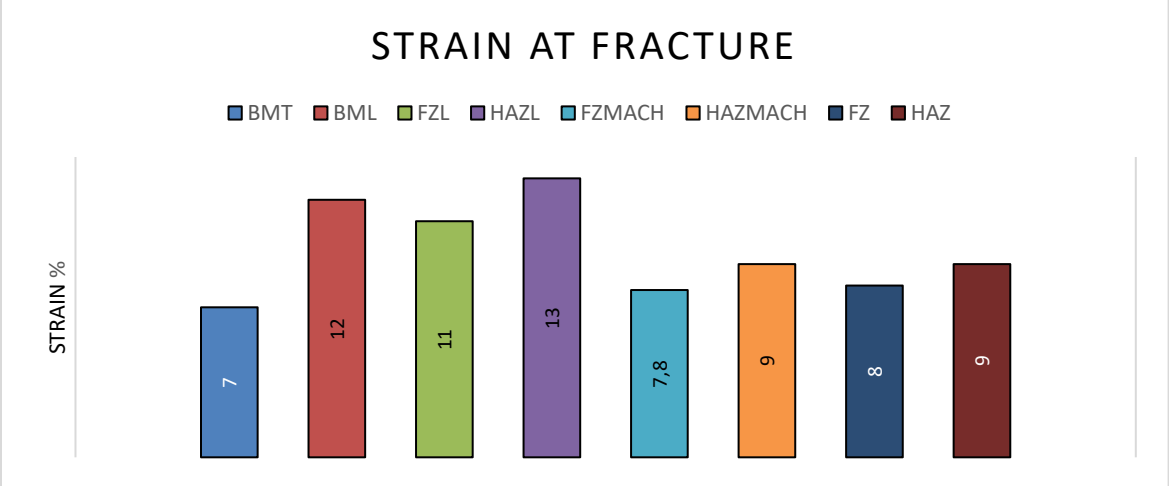

Figure 4.10: Strain at fracture comparison.

As can be seen in the graph above, the most ductile behavior appears in the heat affected zone specimen, in the longitudinal direction. The most brittle behavior appears in the parent material, transversal to the extrusion direction. On the other hand, as can be noticed in the following graphs, the strength in the parent material is the same in both directions.

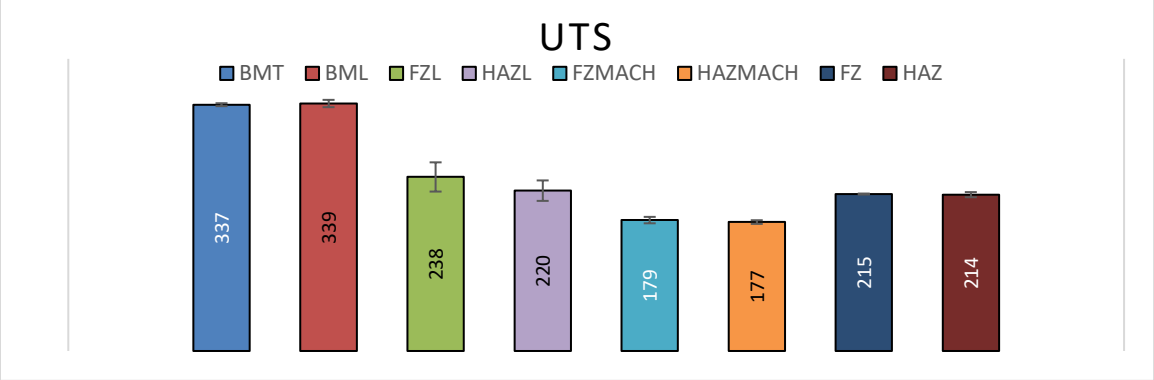

Figure 4.11: UTS results comparison.

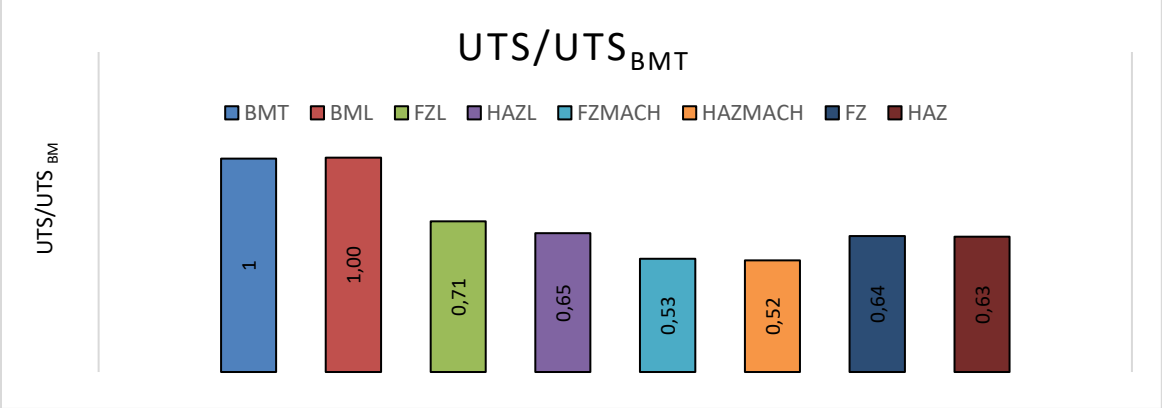

Figure 4.12: Ratio comparison using as a standard value the parent material transverse one.

The last graph shows a comparison between the ultimate tensile strength. The strength in the welded specimens is around a half the one of the parent material.

The following graph shows the reduction in area of the specimens tested. The values have been calculated using the following formula:

$$red\% = \frac{A_f - A_i}{Ai} * 100 \tag{11}$$

Where A_f is the cross-section area after testing, A_i is the cross-section area of the specimen before testing.

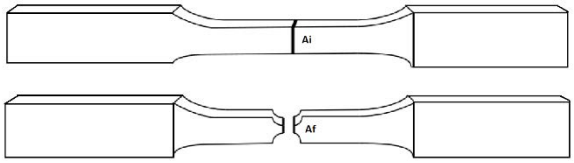

Figure 4.13: sketch of the initial cross-section area Ai and the cross-section area at the point of fracture A_f.

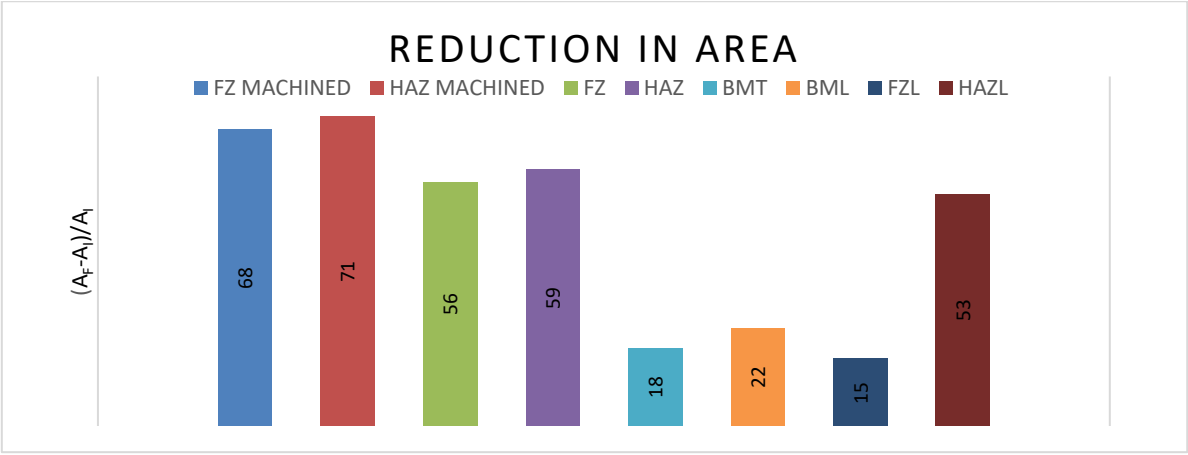

Figure 4.14: Reduction in area of the tensile specimens after testing.

Considering the results from the cross-section area measures, the most ductile behavior is present in the welded specimens. It can also be seen that the fuse zone specimen longitudinal presents the most brittle behavior.

4.5 Fatigue test results

As already explained, the fatigue tests were done using a MTS machine, setting the frequency (10 Hz) and the forces calculated to obtain a stress range R=0,1. A total of 12 specimens for each type were tested. In the following graphs the results of the tests are shown.

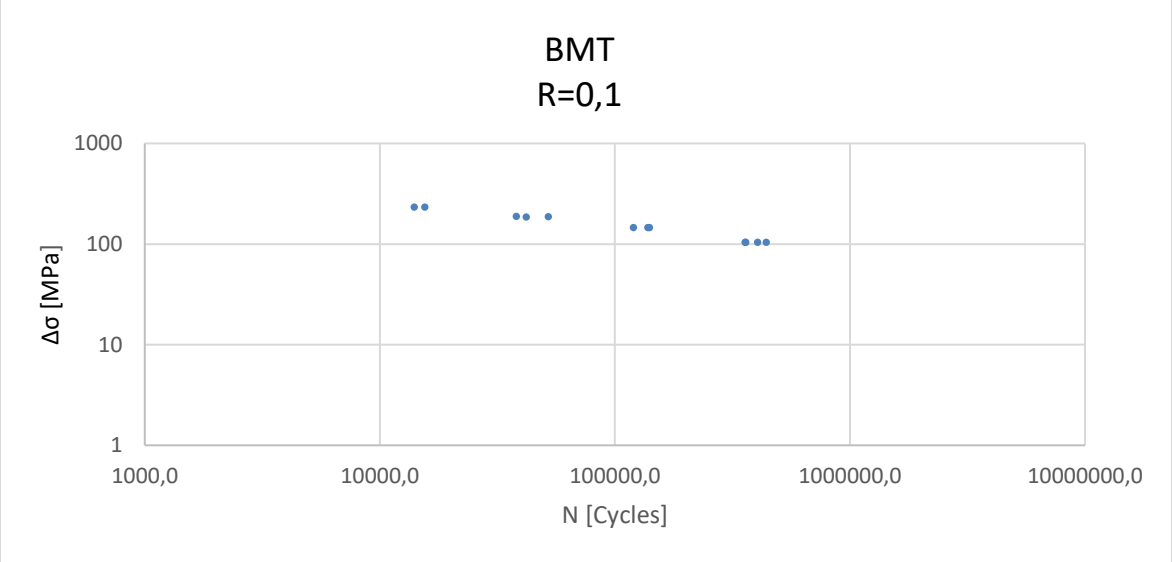

Figure 4.15: S-N curve of the fatigue testing of the parent material taken transverse to the extrusion direction.

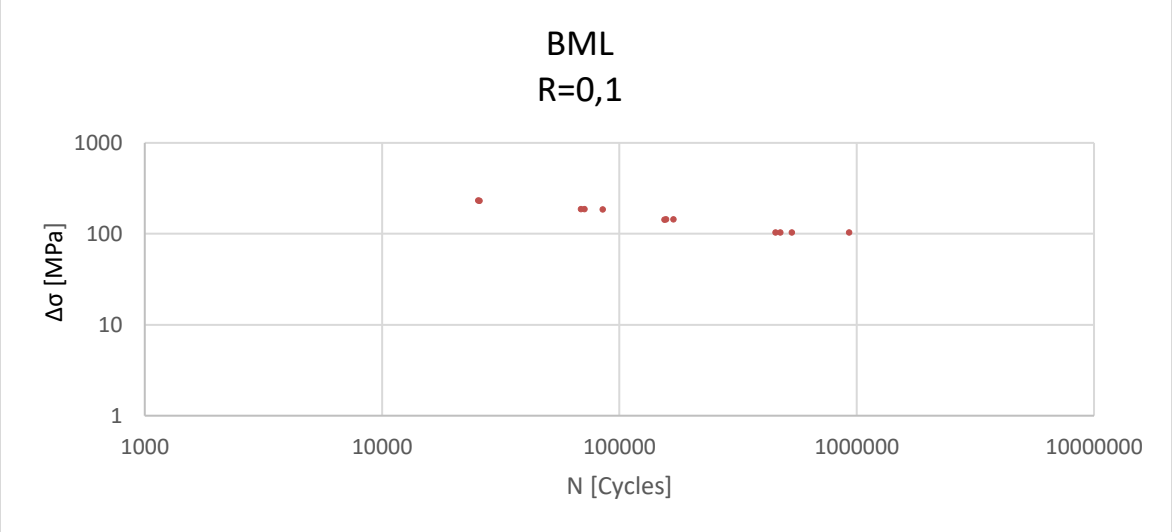

Figure 4.16: S-N curve of the fatigue testing of the parent material taken transverse to the extrusion direction.

The parent material results appear to be in accordance to the typical fatigue behavior. The first plot shows the results obtained testing the parent material in the transverse direction with respect to the extrusion one. The second plot shows the fatigue behavior of the specimens

taken longitudinal to the extrusion direction. In both cases the behavior appears to be the same. The fatigue resistance appears to be a bit higher in the longitudinal specimens.

The plots are shown using the stress range, instead of the stress amplitude, to make the comparison with the standard indications easier.

In the following graphs the results from the fatigue tests made on the welded specimens are shown.

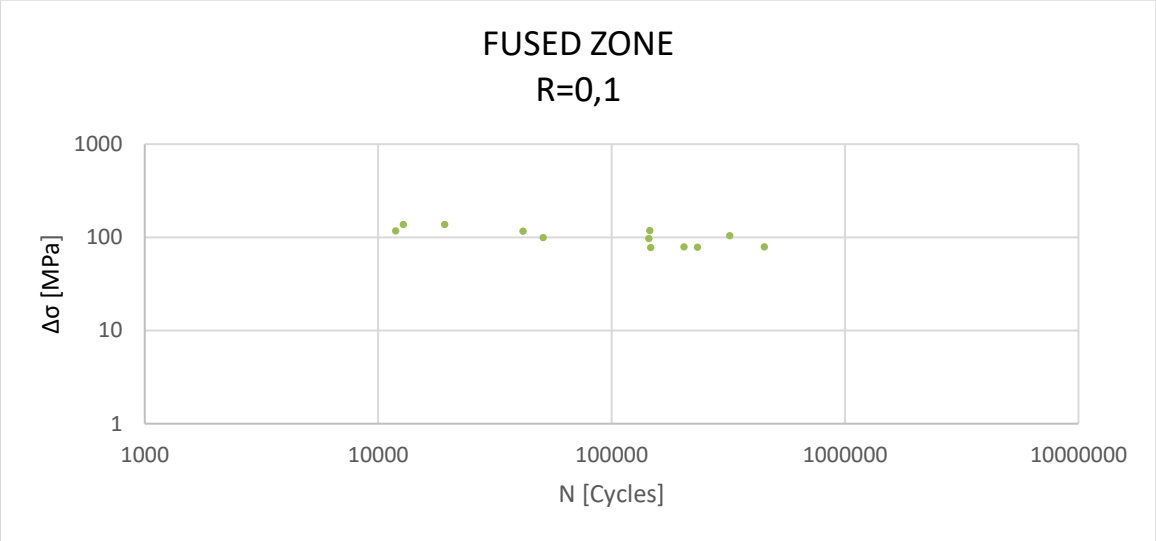

Figure 4.17: S-N curve of the fatigue testing of the welding. Specimen code: FZ.

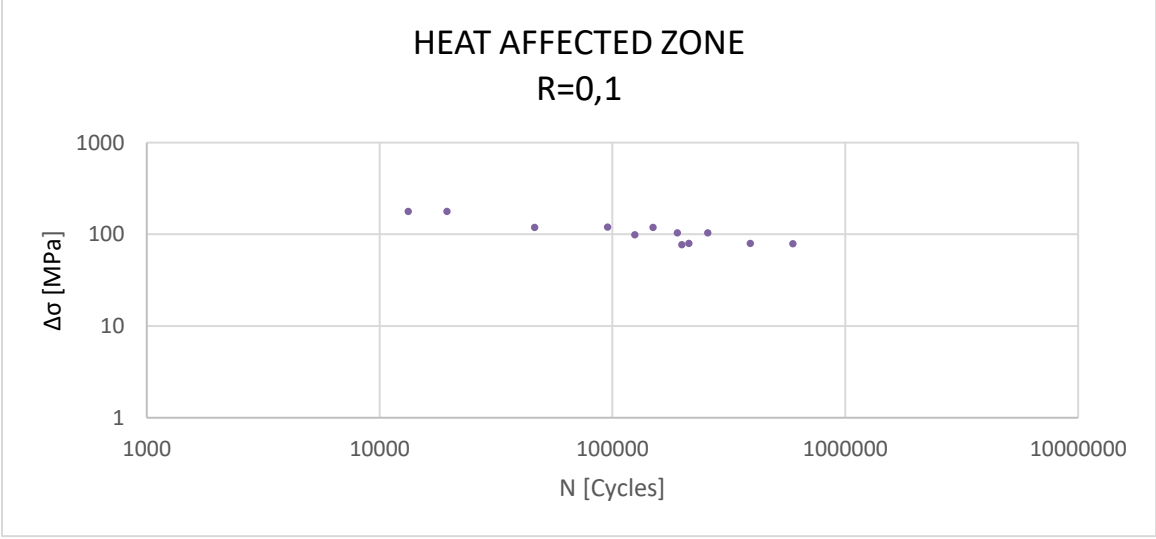

Figure 4.18: S-N curve of the fatigue testing of the welding. Specimen code: HAZ.

The difference between the FZ and HAZ fatigue specimens consists in the position of the geometrical center of the tested zone. In the FZ specimens the fused zone was taken in the center, in the case of HAZ, the center corresponds with the weakest part of the specimens in accordance to the hardness profile measured. This differentiation appears to not have effect on the breaking mechanism: as expected all the fatigue specimens broke starting from the welding toe, where the stress concentration occurs.

As can be seen, the fatigue resistance in the welded specimens appears to be lower than in the parent material. This behavior is due to the stress concentrations that occur on the weldment toes. This stress distribution is shown in the following schematic model (Figure 4.19).

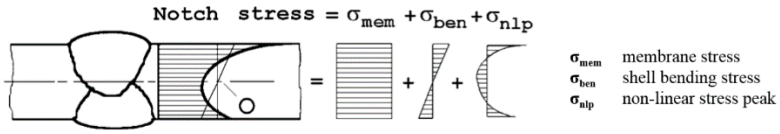

Figure 4.19:The stress distribution over the plate thickness is non-linear near notches.

To calculate the fatigue behavior of the welded specimens the nominal stress was used.

Nominal stress is the stress calculated in the sectional area under consideration, disregarding the local stress raising effects of the welded joint, but including the stress raising effects of the macro geometric shape of the component near the joint, such as large cutouts. The nominal stress may vary over the section under consideration. The effects of macro geometric features of the component as well as stress fields near the concentrated loads must be included in the nominal stress. The secondary bending stress caused by axial or angular misalignment needs to be considered if the misalignment exceeds the amount which is already covered by fatigue resistance S-N curves for the structural detail. This is done by the application of an additional stress raising factor $k_{m,eff}$. The misalignment is considered when assessing the fatigue actions (stress) by multiplying by the factor. In our case both the results have been taken. This choice comes from the fact that the results appear to be more similar to the standard graphs not using the $k_{m,eff}$ factor. In the following Figure 4.20 the two conditions of misalignment present in our specimens are shown.

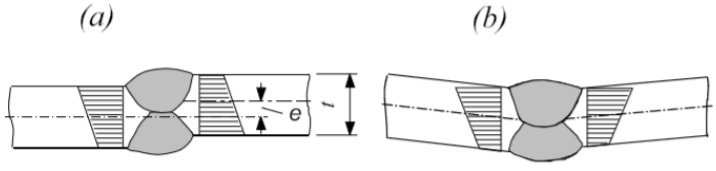

Figure 4.20: Schematic representation of misalignment cases.

In simple components as in our case, the nominal stress can be determined using elementary theories of structural mechanics based on linear-elastic behavior. Nominal stress is the average stress in weld throat or in plate at weld toe.

$$\sigma = \frac{F}{wt} \tag{12}$$

Where F is the force set in the testing machine, w is the width of the specimen and t the thickness of it.

Many of the welded specimens tested were not straight as in the following schematic Figure 4.21.

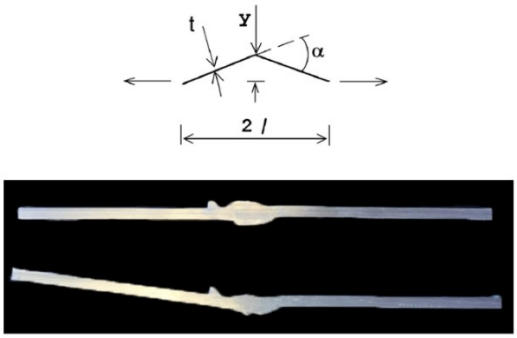

Figure 4.21: Model of the specimen misalignment. The best and the worst case we had are shown.

To consider the misalignment effect explained before, a formulation of the $k_{m,eff}$ factor is provided as follows:

$$k_m = 1 + \frac{3}{2}\frac{\alpha l}{t}\frac{\tanh(\beta/2)}{\beta/2} \tag{13}$$

Where α is the angle of misalignment, l is the half length of the specimen tested, t the specimen thickness, and β as follows:

$$\beta = \frac{2l}{t}\sqrt{\frac{3\sigma_m}{E}} \tag{14}$$

Where σ_m is the membrane stress, E the Young's modulus. The tanh correction allows for reduction of angular misalignment due to the straightening of the joint under tensile loading. It is always <1 and it is conservative to ignore it. In our case it has been taken.

To measure the misalignments the software Kinovea was used. This software allows to measure the angles using picture of the specimens.

The resulting S-N diagrams are shown in the followings figures:

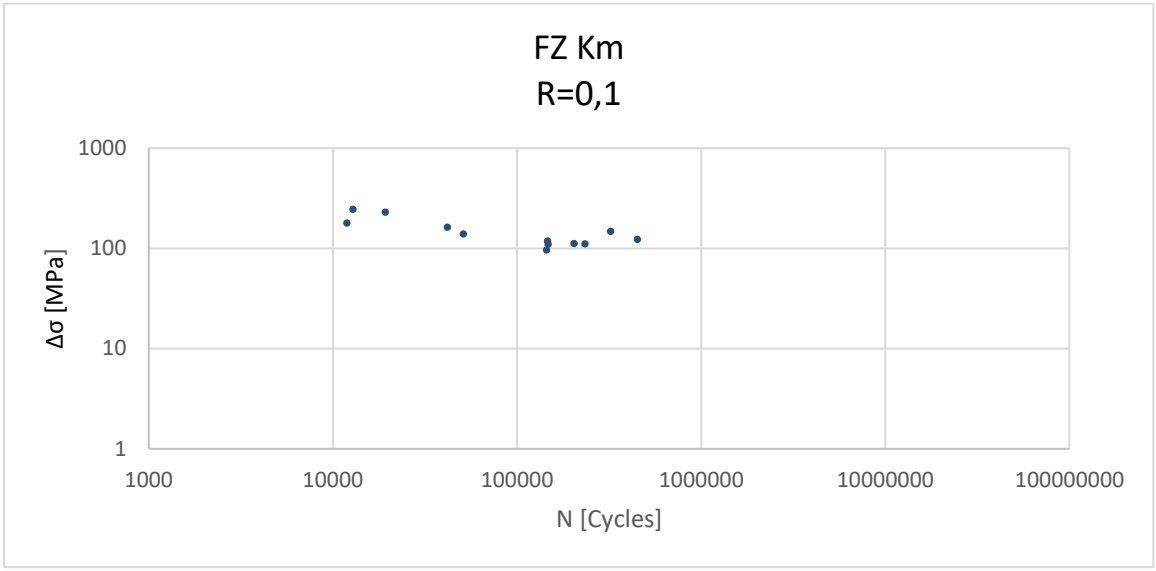

Figure 4.22: S-N curve of the fatigue testing of the welding. Specimen code: FZ.

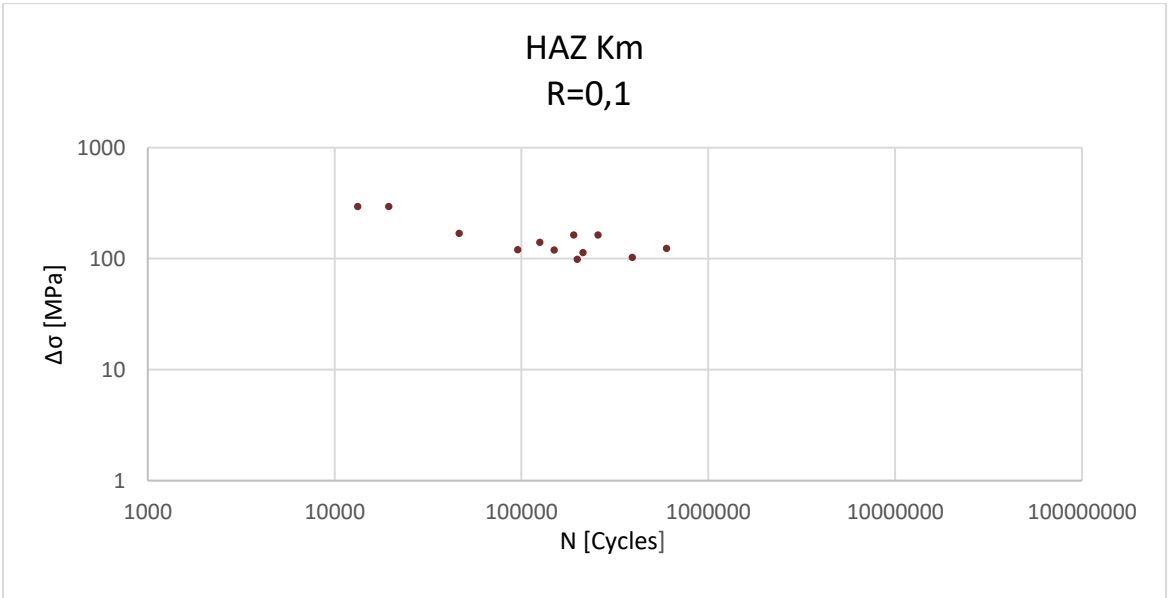

Figure 4.23: S-N curve of the fatigue testing of the welding. Specimen code: FZ.

As a result, the equivalent stress calculated applying the formula provided is higher. The equivalent fatigue resistance seems to be higher considering this effect.

Figure 4.24 shows the SEM fractography of a selected fatigue specimen.

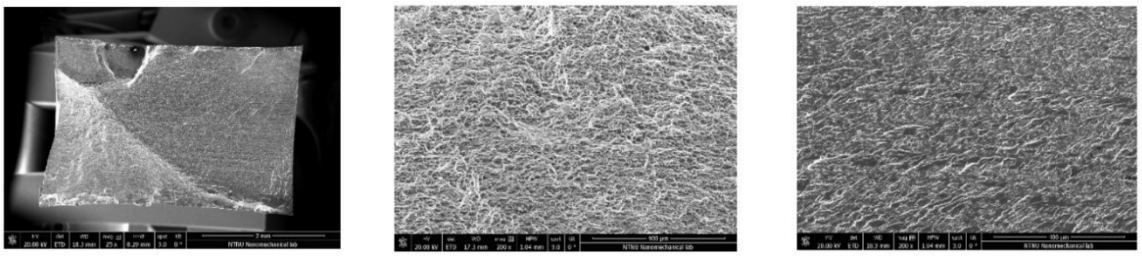

Figure 4.24: Fractography of a selected specimen after breaking under cyclic load in the fatigue test. The specimen is one of the parent material.

As can be noticed, two different zones are present. The zone on the upper part shows the crack propagation, the other one is the final rupture zone. Further fractography of selected fatigue specimens can be found in the Appendix.

4.6 Impact test results

Figure 4.25 shows macro images of a selection of the Charpy V-notch specimens. The figure includes images of the base metal specimens representing the transverse d) and longitudinal c) orientations, the fused zone longitudinal a) and transverse b), heat affected zone longitudinal e) and transverse f).

Figure 4.25: Macro images of the Charpy V-notch specimens after testing.

From the picture above, the different behavior of the specimens can be seen. The specimens taken from the heat affected zone are not completely broken. The fused zone specimens appear to have an uneven fracture surface, and the parent material doesn't show difference if tested in the longitudinal or transversal direction. In the following diagrams the results from the impact tests are shown, the values are referred to the mean of the three specimens tested for each category.

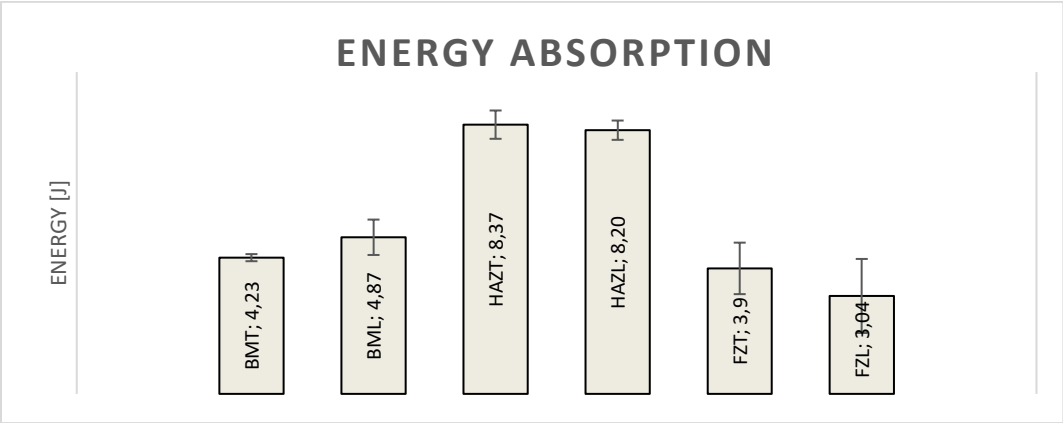

Figure 4.26: Energy absorption from Charpy test.

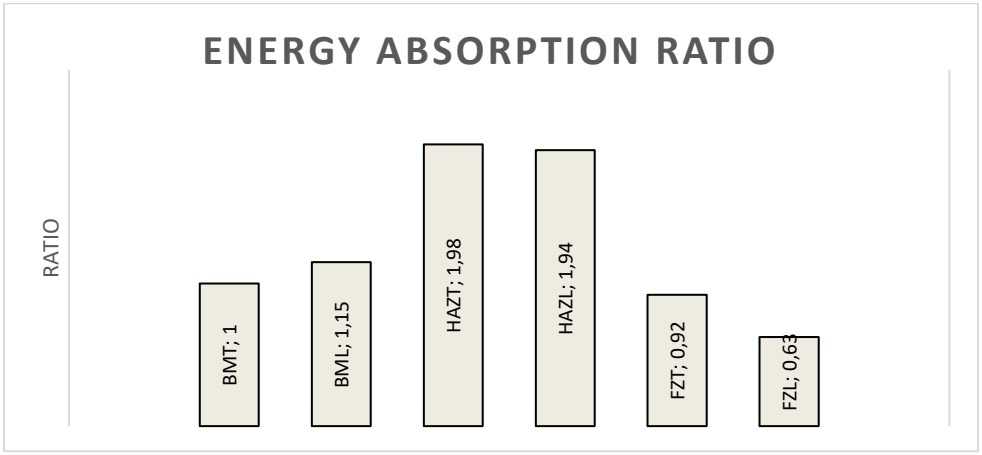

Figure 4.27:Energy absorption ratios using the parent material as a referring value.

As can be seen in the graphs above, the energy absorption is higher in the specimens taken from the heat affected zone (both longitudinal and transversal). This behavior can be also explained referring to the results from the tensile and hardness tests, which show the more ductile properties of the heat affected zone, where the strength, on the other hand, is lower. The parent material tested in the longitudinal direction shows also a bit higher energy absorption capacity with respect to the parent material taken transverse to the extrusion direction. This is in accordance to what obtained in the tensile test, where the strain at fracture was higher in the longitudinal specimens. The lowest value in energy absorption was obtained with the specimens from the fused zone. This low capacity in absorbing energy can be due to the pores that are present in this zone. It has to be taken in account that the filler material of the fused zone has a different composition with respect to the material of the welded plates.

4.7 Fractography of the specimens

In this subchapter a series of images showing the fracture surface of the specimens tested are presented. In particular the fracture surface of transverse specimens of the tensile and fatigue are presented. Fractographs have been taken from selected specimens. All the fractography picture taken with the SEM microscope can be found in the Appendix.

4.7.1 The tensile fractured surface:

Heat affected zone

The following picture (Figure 4.28) shows the fractography of the specimen broken under static tension in the tensile test. The zone of fracture is located in the heat affected zone, in proximity of the weakest section. The specimen under consideration is one of the machined ones, in which the reinforcement of the welding has been removed using a milling machine.

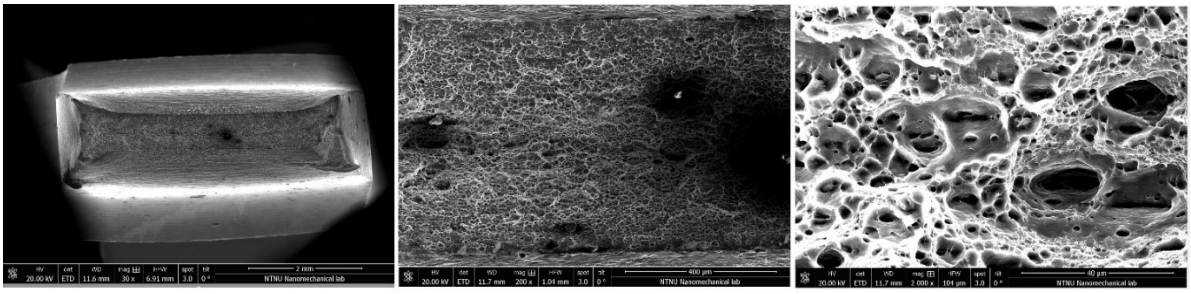

Figure 4.28: fractography of a selected specimen broken under static tension in the tensilte test.

As can be seen in the figure above, the fracture surface of the tensile specimen broken in the heat affected zone has the characteristic of a ductile fracture. The fracture surface presents many dimples, this is in accordance to the tensile test results, in which the heat affected zone presents a ductile behavior. In the middle of the fracture surface some darker zones are visible, this can be due to the presence of some defects or to some pieces of fractured aluminum which deposited on the surface after the test. Considering the Figure 4.28 (a), the reduction in area is clear, the deformation of the edges is typical of a ductile fracture.

Parent material

The following Figure 4.29 shows the fractography of the specimen broken under static tension. The zone of fracture is not in the middle of the specimen, but neither so far from it. The specimen is one of the parent material taken transverse to the extruding direction.

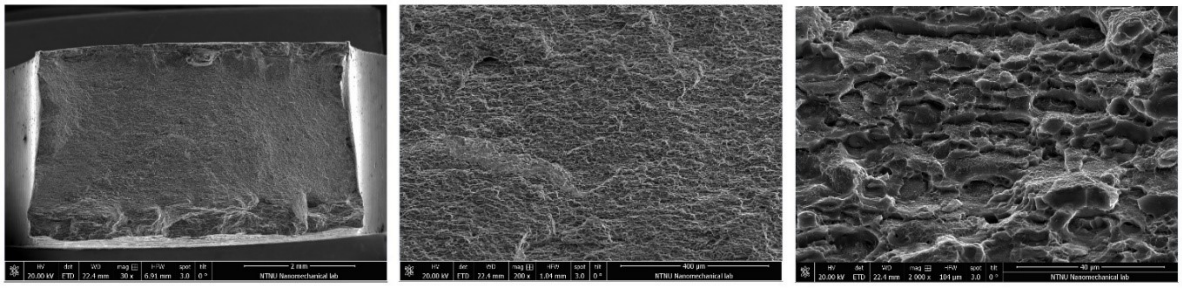

Figure 4.29:fractography of a selected parent material specimen broken under static tension.

As can be seen in the figure, also in this case the fracture surface is covered by many dimples. This is in accordance to the tensile test results, in which the parent material presents a ductile behavior. Note that the fracture surface appearance is different with respect to the HAZ one, which presents smaller dimples and a greater deformation in the edges. This is because the parent material is not as ductile as the one in the HAZ.

Heat affected zone

The following Figure 4.30 shows the fractography of a selected specimen broken under static tension in the heat affected zone. The specimen is one of the welded in which the reinforcement has been taken.

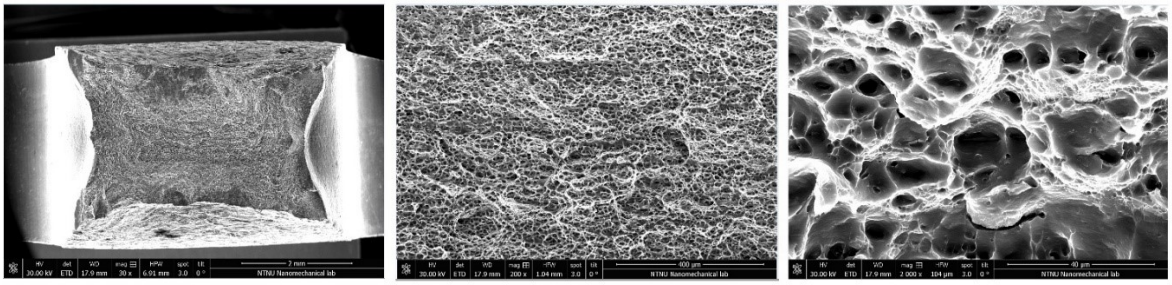

Figure 4.30:fractography of a selected specimen broken under static tension in the heat affected zone

The fracture surface appears similar to the first case presented in this chapter, which showed the fracture in the machined specimen, but where the fracture occurs in the same zone. The mechanism of fracture is the same, the surface is covered by small dimples and the edges are deformed, showing the ductile behavior of this zone. The reduction in area is great also in this case.

Fused zone longitudinal

The following Figure 4.31 shows the fractography of the specimen broken under static tension. The specimen under consideration was taken from the welded zone, longitudinal to the welding direction.

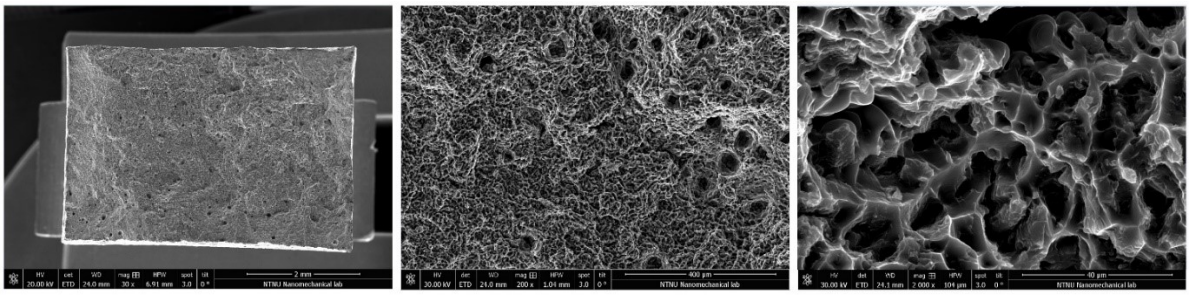

Figure 4.31:fractography of a selected specimen broken under static tension in the fused zone.

Considering the Figure 4.31 (a), the main difference with respect to the previous cases is that the edges are not deformed, the fractured area appears rectangular as the initial one. This macro feature shows the more brittle behavior of the fused material. In addition to that, the presence of many pores explains the more brittle behavior of this zone, where the elongation at fracture is lower than the one of the other tensile tests. The reduction in area measured was in accordance to what just said.

4.7.2 The fatigue fractured surface

The most characteristic feature that identifies the fatigue fracture at the microscopic level are the striations, even if they are not always present on surfaces. The striations are due to the crack propagation, when the cycle of load occurs, on the apex of the crack there is a plastic deformation at a microscopic level.
This phenomenon generates on both fracture surfaces a small striation, index of the crack propagation. The striations identify the position of the origin of the fracture, which is configured as the point of convergence those; they propagate from the origin, often in circular or semicircular way and they are relatively parallel. They don't cross each other. If the load cycle is constant, the striations close to the origin are extremely small and the space between two successive ones is very small; the crack grows slowly because its size is still small. As the fracture propagates, the resistant section area is reduced, therefore, for the same maximum load, the applied stress increases and this leads to an increase of the space between the striations.
Once the crack starts to propagate, the resistant section area is reduced until the resulting stress is too high for the material. At this moment the final breaking occurs. This can be both fragile and ductile, depending on the metal involved. Usually, as the fracture due to fatigue mechanism does not require high level of stress, there isn't an appreciable plastic deformation in the specimen tested.

Parent material

In the following figure 4.32, the fracture surface of the parent material broken under cyclic load is shown. The specimen under consideration is one of the transverse to the extruding direction.

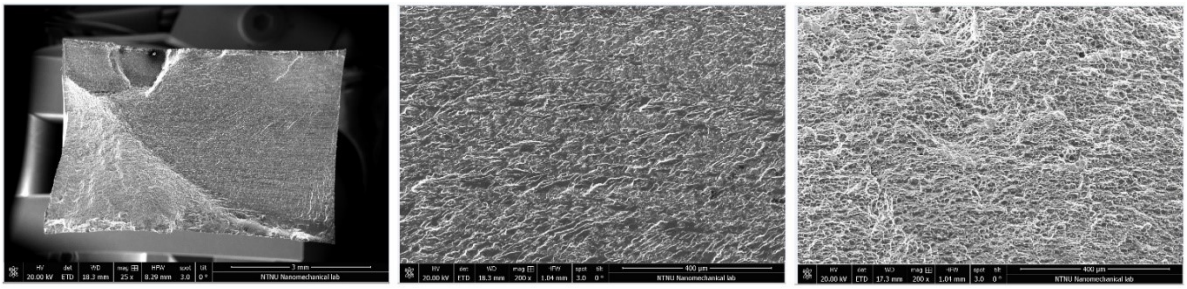

Figure 4.32:Fractography of a selected parent material specimen broken under cyclic load.

As can be seen in the pictures above, the typical fatigue fracture surface is present. The fracture propagated from the surface collocated in the upper part in the Figure 4.32 (a). The specimen under consideration broke at high cycles. The area where the striations are visible is large, this is due to the low stress applied during the test. In Figure 4.32 (b) a high magnification of the area of propagation is shown, the direction of the growth of the crack is clear and it follows the striations direction. On a macroscopic level, the fatigue fractured area is plane and perpendicular to load direction. In Figure 4.32 (c) the final fracture area is shown. This zone has the typical characteristics of a ductile fracture, covered by dimples and with a fracture surface oriented 45° with respect to the load direction. The shape of the dimples does not follow a specific direction.

Welded specimen

In the following Figure 4.33, the fracture surface of a welded specimen broken under cyclic load is shown. The specimen under consideration broke in the zone close to the welding, the fracture started from the toe of the welding.

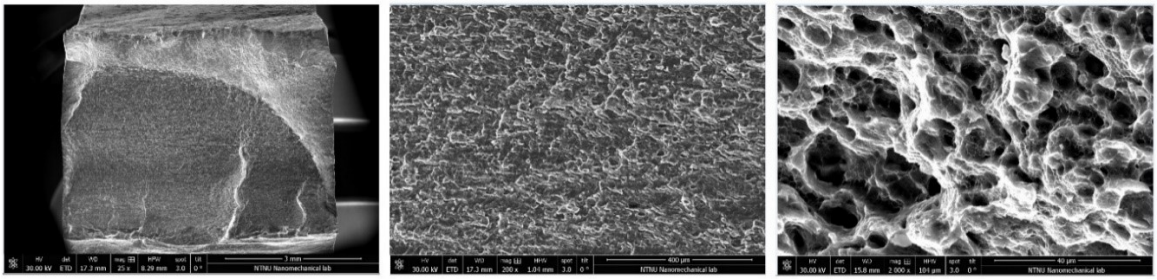

Figure 4.33:Fractography of a selected welded specimen broken under cyclic load.

Considering the Figure 4.33 (a), the crack propagated from the lower zone. The specimen under consideration broke at high number of cycles. In accordance to that, the zone of the fracture propagation covers the main percentage of the total area, on the other hand, the final fracture zone is small. In Figure 4.33 (b) a high magnification of the fracture propagation zone is shown. In Figure 4.33 (c) a high magnification of the final fracture zone is presented. Note that the magnification of the last figure is ten times higher than the one in the middle. In this case as in the previous one, on a macroscopic level, the fatigue fractured area is plane and perpendicular to load direction. The final fracture area has the typical characteristics of a ductile fracture, covered by dimples and with a fracture surface oriented 45° with respect to the load direction.

5 Discussion

In this chapter, the results from the tests will be discussed and analyzed. The fatigue performance will be discussed in comparison with the standard. The hardness profiles have been used to calculate the HAZ yield stress profiles, and the results will be compared with the yield stress measured in the tensile testing. This analysis is accompanied by a case study of the load-bearing capacity of the joints.

5.1 Fatigue performance

In this subchapter the fatigue performances are analyzed. The use of the k_m factor will be discussed. The following Figure 5.1 shows the S-N curve for different types of welding geometries. The class we will consider is the 25, where 25 is the value of stress at $2*10^6$ cycles. The standard graph given is referred to a test run with R=0,5. In our case the R was equal to 0,1 but the comparison can be done in accordance to the standard indication, using a correction factor equal to 1.

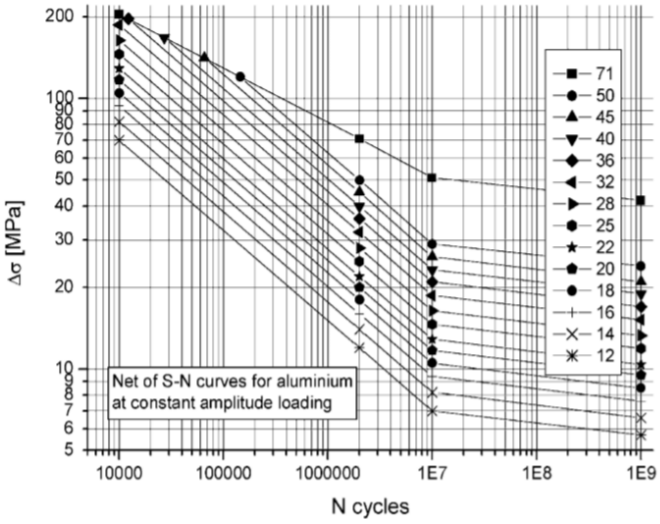

Figure 5.1: S-N curve from the standard used to compare the results.

In the following graphs, the resulting S-N graphs are presented, comparing the values obtained using the k_m factor with the original values obtained from the tests. Those results will be then compared with the parent material results and with the standard shown above.

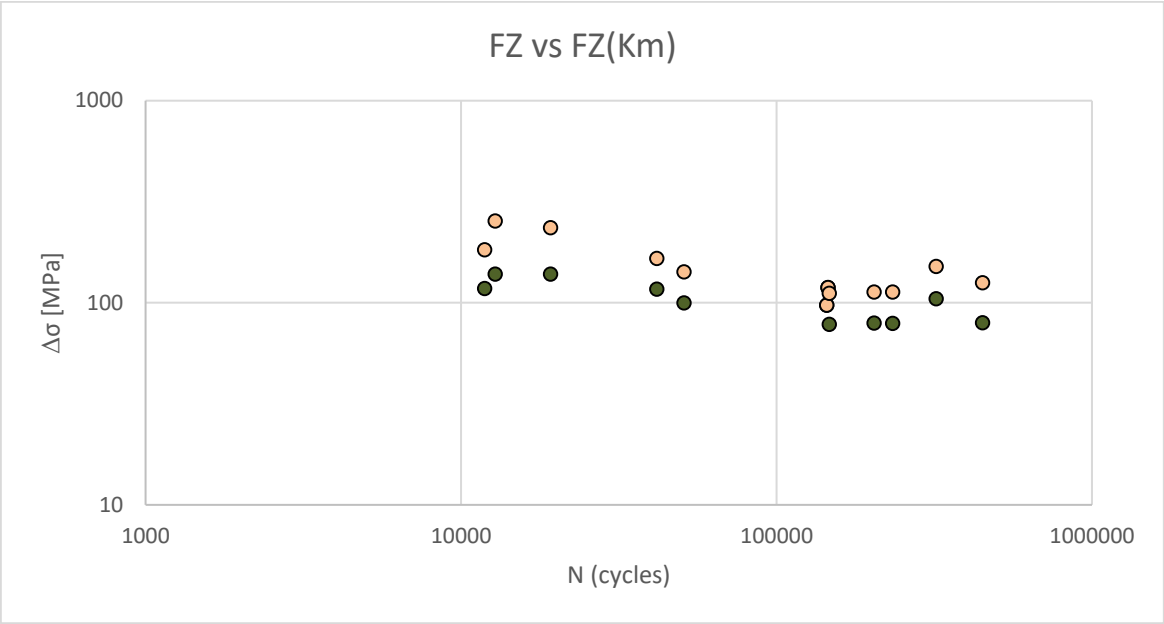

Figure 5.2: S-N diagram of the welding.

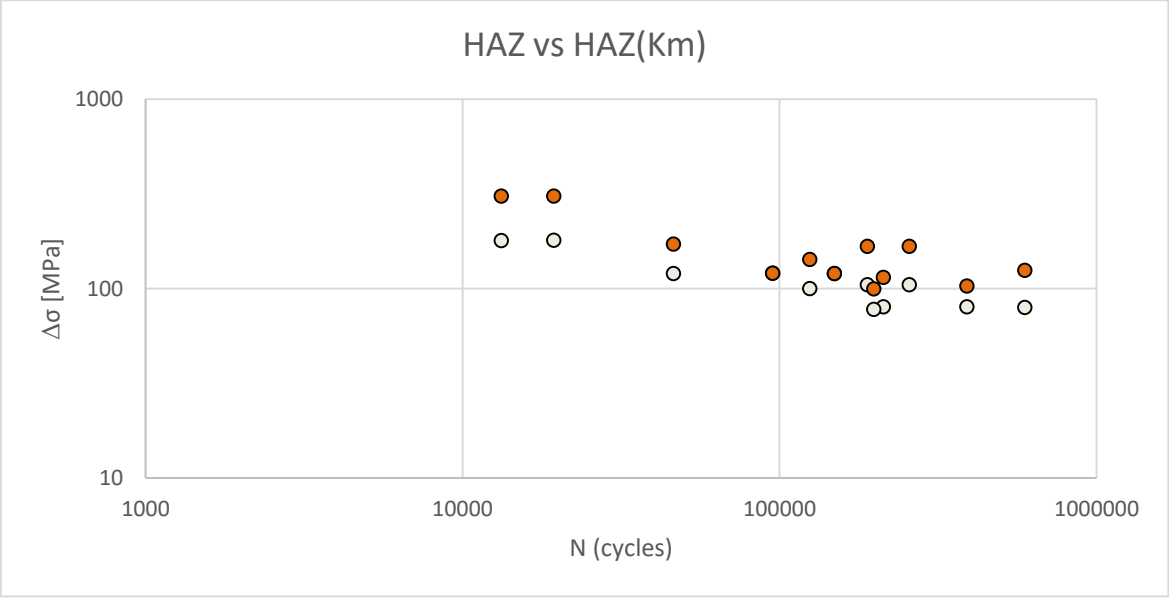

Figure 5.3:S-N diagram of the welding.

The two previous graphs show the behavior of the welding considering or not the Km factor. As the misalignment is high in some specimens, the resulting Km factor is sometimes near to 2, that means the fatigue resistance would be twice in the case of well aligned specimen. This result will be discussed in the following parts, comparing those corrected results with the parent material and the standard indications.

Comparison of the results

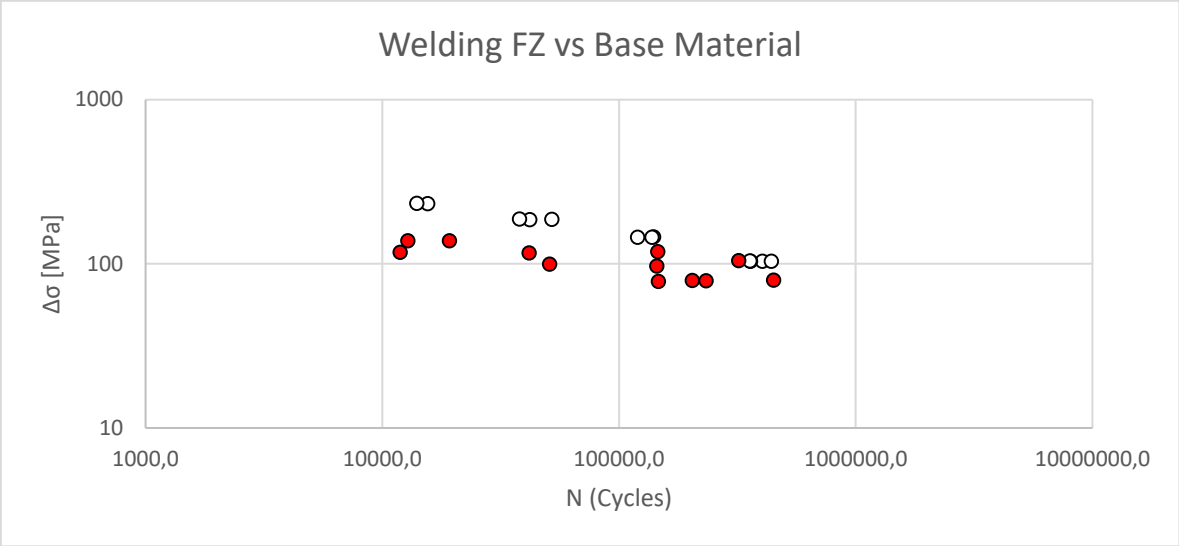

Figure 5.4: S-N diagram: comparison between the welding and the parent material results.

The previous graph shows the comparison between the performance of the welded plates with respect to the parent material. As can be seen, the parent material shows a better performance, resisting a higher number of cycles under the same cyclic stress.

If we consider the K_m factor, the fatigue resistance of the welded plates increases and the difference between the welding and the parent material changes.

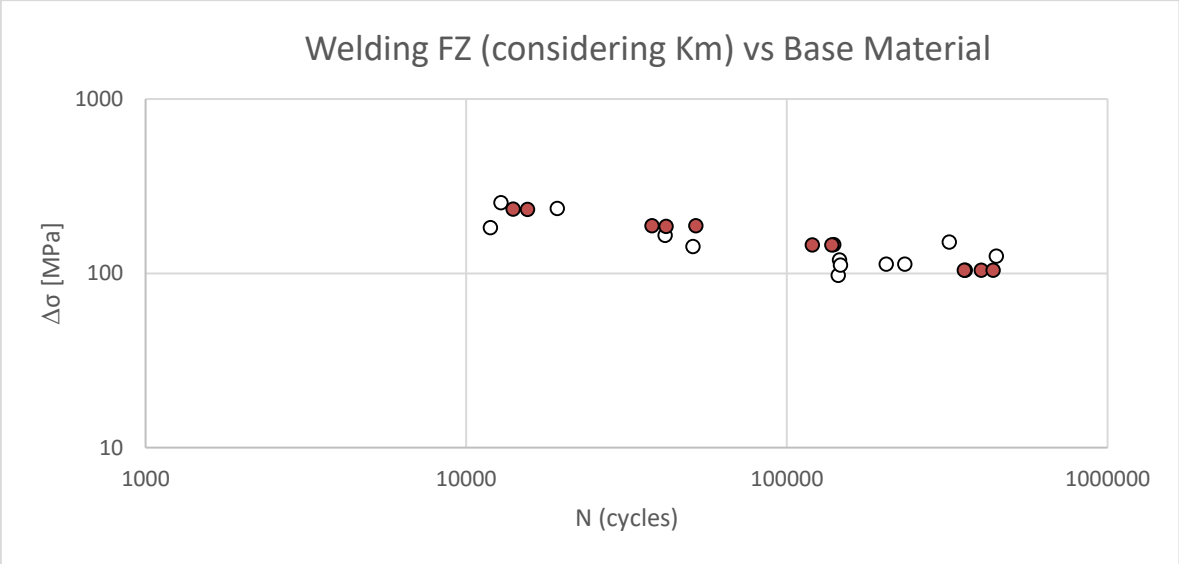

Figure 5.5:S-N diagram: comparison between the welding FZ results corrected considering the Km factor and the parent material results.

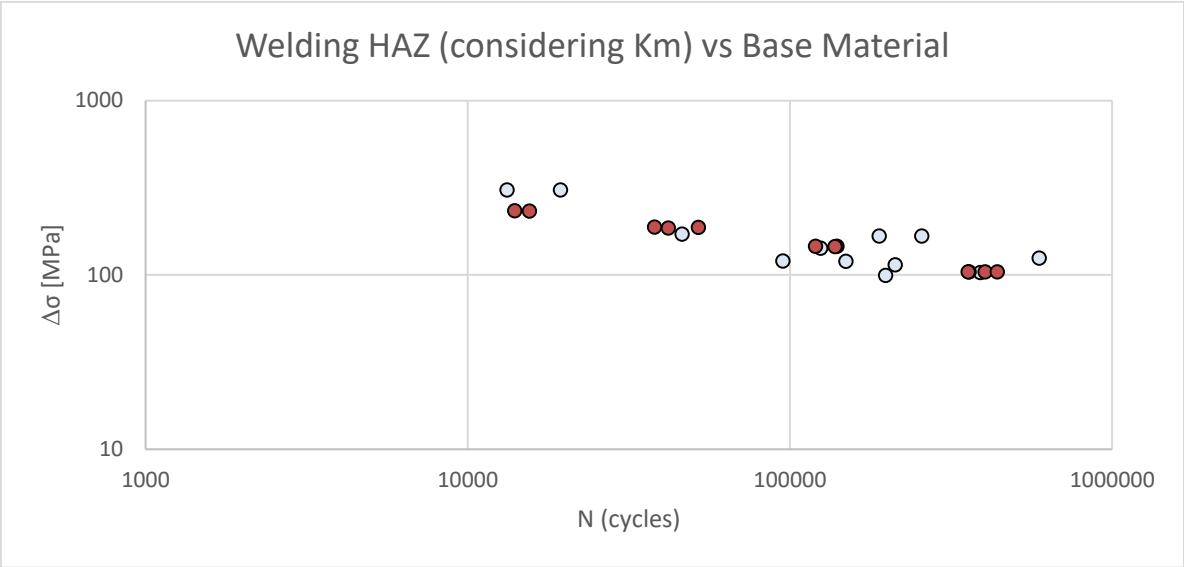

Figure 5.6:S-N diagram: comparison between the welding HAZ results corrected considering the Km factor and the parent material results.

As can be seen in the previous graphs, the fatigue resistance of the welded specimens appears to be more similar to the one of the parent material. Note that all the welded specimens broke as expected starting from the root toe, where the geometrical notch is responsible of the stress concentration. A further comparison can be done with the fatigue behavior given by the standard. This comparison is presented in the following graphs.

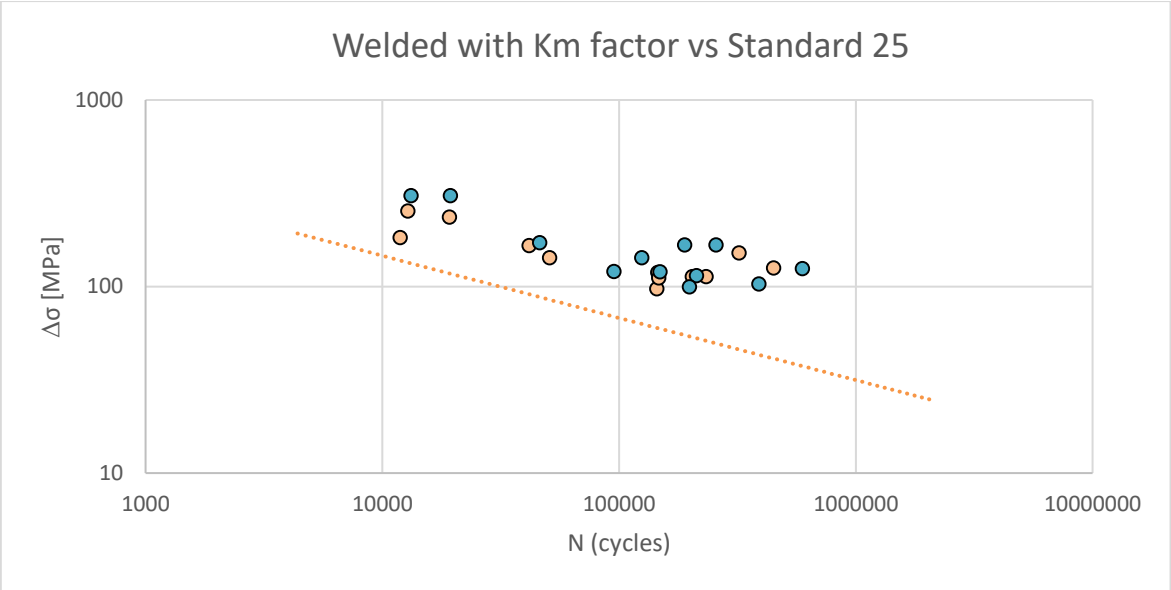

Figure 5.7:S-N diagram: comparison between the welding results corrected considering the Km factor and the standard curve (class 25).

The line under the points is the expected behavior given in the standard indications, considering the class 25. This result shows the behavior that would be expected using the K_m factor, showing how the fatigue resistance of straight specimens would be higher.

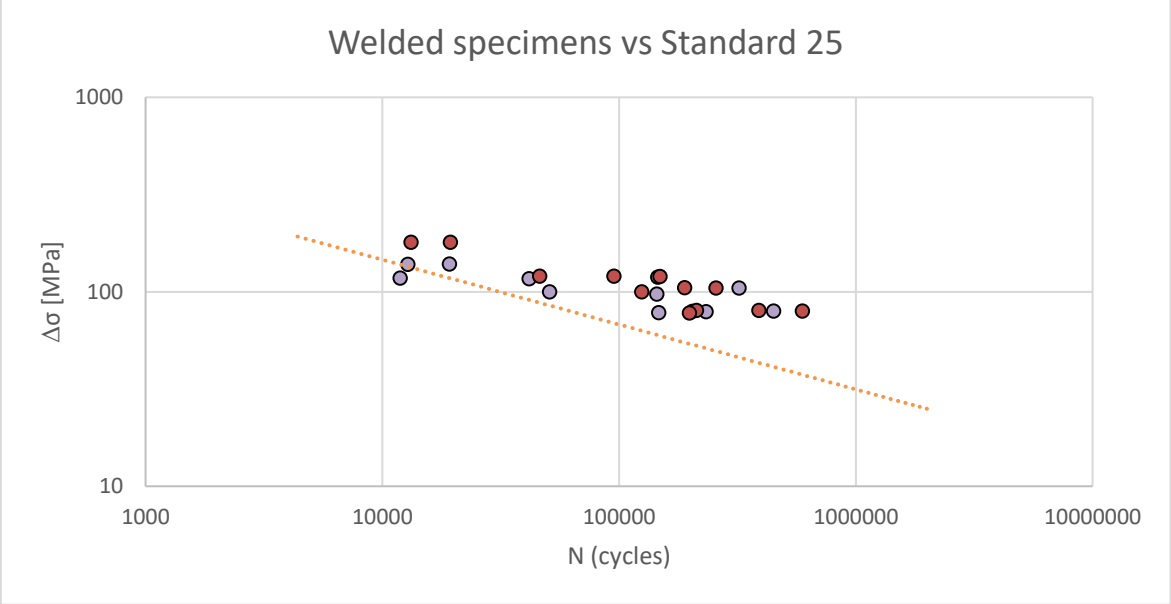

Figure 5.8:S-N diagram: comparison between the welding results and the standard curve (class 25).

The graph shows the distribution of the points obtained with the fatigue test of the welded specimens. As can be noticed, there is one point that is under the standard line. For the material characterization process is better to keep the worst case, but it's also true that the standard provides the K_m factor that should be applied in our case as has been done. The results are presented both using the correction and in the original values to provide a more complete overview of the behavior of the material. Note that the standard line is referred to a PS95%. Considering that, the results obtained using the K_m factor appear to be more in accordance to the standard indications.

The following Table 5.1 provides an overview of the fatigue results, giving the values of the k as an indication of the slope of the log-log resulting graphs.

Table 5.1: Overview of fatigue test results: K and $\Delta\sigma_{(95\%)(2e6)}$,

	BMT	BML	FZ	HAZ	FZ+HAZ	FZ (Km)	HAZ (Km)	FZ+HAZ (Km)	Standard for welding
k	3,9	3,7	4,6	3,6	3,8	3,3	2,5	2,8	3
$\Delta\sigma_{(95\%)(2e6)}$	62	64	30	33	31	28	23	27	25

The value of k in literature is around 4 for the parent material, and this value is in accordance to what has been found from the tests. For the welding, the standard provides a value equal to 3 for the k. As can be seen in the Table 5.1, the experimental results are in accordance to that indication. Another parameter to compare is the value of stress at $2*10^6$ cycles, which should be equal to 25 considering the standard chosen. The results show that this value is closer to the standard if we consider the K_m factor to take into account the misalignment effect.

As a conclusion, it can be said that the standard gives good indications for the case studied.

5.2 Relationship between hardness profile and yield strength

All the tensile specimens broke in the Heat Affected Zone approximately 10 mm from the welding center. This corresponds well with observations made from the hardness profile, where the minimum hardness is found in HAZ on the side without the guide for the welding tool (the plate had that guide because the same plates were used for the HYB). This fact can be due to the heat dispersion which is higher in the part with the guide because of the higher heat exchange area.

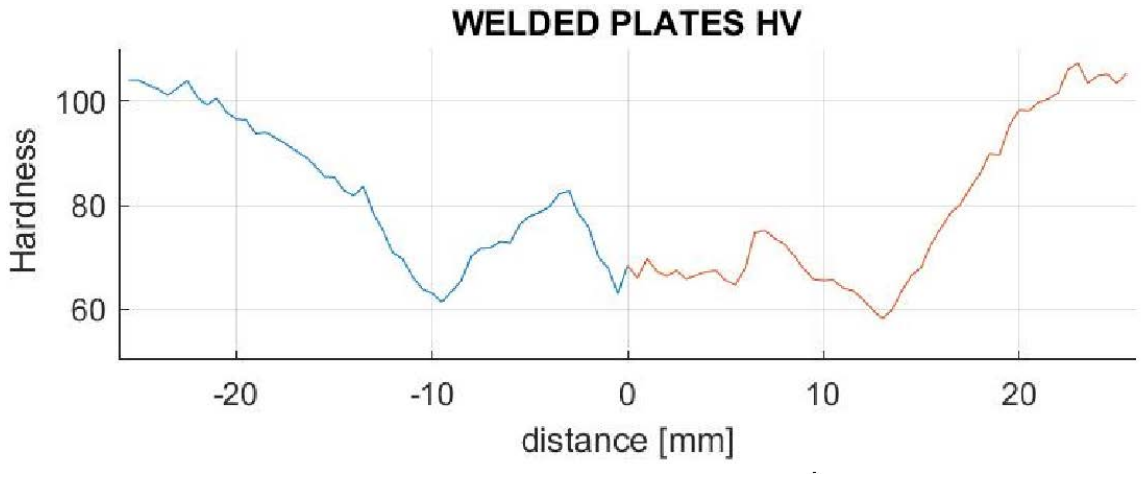

Figure 5.9:Hardness profile of the welded specimen.

Considering the correlation between hardness and yield strength, the resulting yield strength profile for the welded plates can be calculated based on Equation (1) and the experimental hardness profiles.

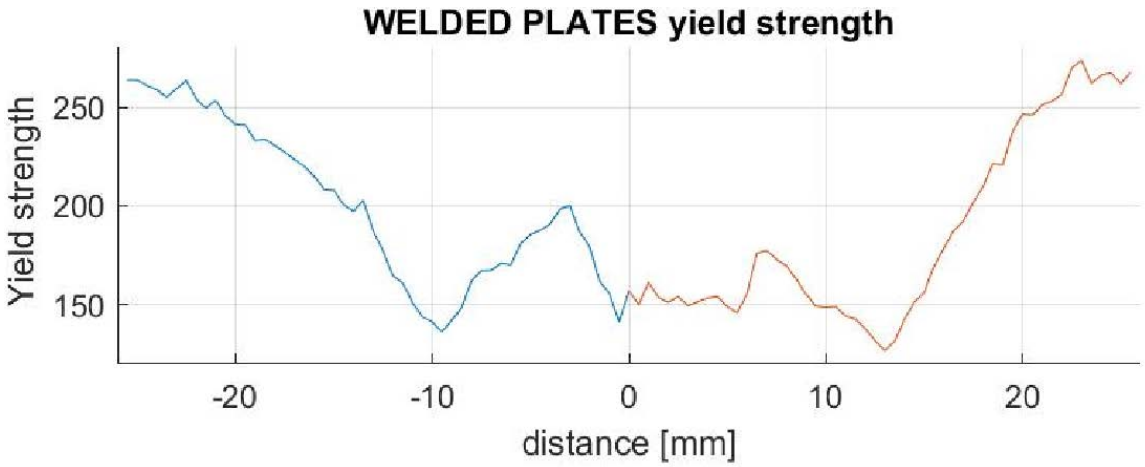

Figure 5.10: Yield strength profile of the welding.

The previous graphs can be explained considering the following schematic illustration of the response of a peak-aged Al-Mg-Si alloy to GMAW. The sketch is a correlation between peak-temperature distribution around the weld and the quasi binary Al-Mg_2Si phase diagram.

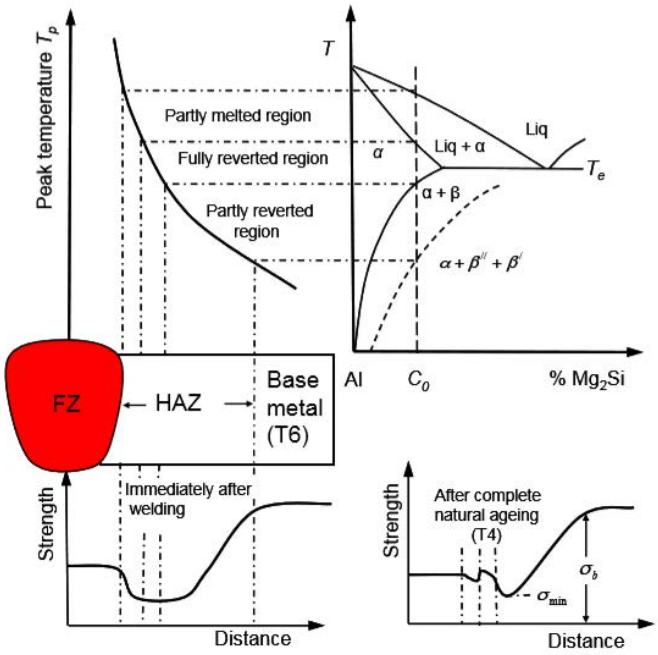

Figure 5.11: Schematic illustration of the response of a peak-aged Al-Mg-Si alloy to GMAW. [18]

During the welding, as illustrated in the previous Figure 5.11, the hardening β'' and β' precipitates present in the partly reverted region, after artificial ageing, become thermodynamically unstable and start to dissolve. This causes a strength reduction in the material close to the fusion line. This can be observed in the experimental data plotted in

Figure 5.9, at the point where the hardness drops to 58 HV. In addition. Some strength recovery may occur between the fusion line and the minimum HAZ hardness, due to following natural ageing of the material in as-welded condition. This is also observed in Figure 5.9, at the point where the hardness reaches approximately 75 HV.

Table 5.2 summarizes the base metal yield stress σ_b and the minimum HAZ yield stress σ_{min} found in the yield stress profiles and measured from the tensile testing.

Table 5.2: Summary of the yield stress calculated from the HAZ hardness profiles and measured from the tensile testing of the GMAW.

Yield strength [MPa]			
From yield stress profile		From tensile test	
σ_b	σ_{min}	σ_b	σ_{min}
266	126	317	141

From Table 5.2, it is observed that the base metal yield strength σ_b and the minimum HAZ yield strength σ_{min} calculated from the hardness profiles, are in accordance with the yield stress measured from the tensile tests. As a matter of fact, the model gives a pessimistic estimation with respect to the real results of the tests.

Table 5.3 summarizes the total strength reduction in the GMAW. The calculations are based on the yield strength found for the base metal yield strength σ_b and the minimum HAZ yield strength σ_{min} from the yield stress profiles and from the transverse tensile specimens.

Table 5.3: Strength reduction % from yield stress profile and from tensile test.

Strength reduction (%)	
From yield stress profiles	From tensile test
47	44

From Table 5.3 it is evident the great reduction in strength due to the welding. This must be considered in mechanical design. In the following subchapter an example of this consideration will be presented.

5.3 Load-bearing capacity of the GMA weldments

The following schematic Figure 5.12 shows the assumed dimensions of AA6082-T6 sheets to be tested subsequent to the welding under consideration. The figure shows the two cases of loading: perpendicular and parallel to the weld.

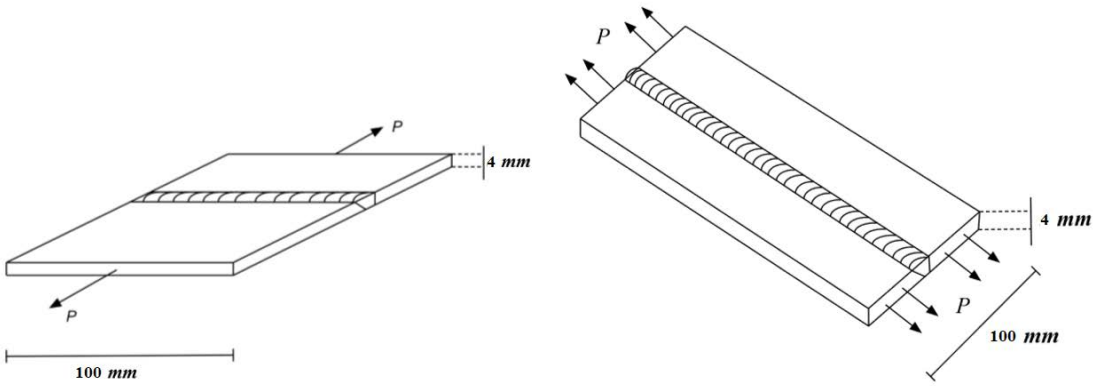

(a) Loading perpendicular to weld **(b)** Loading parallel to weld

Figure 5.12: Assumed dimensions of the AA6082 sheets subsequent to GMA and FS welding, where the loading is perpendicular and parallel to the weld, respectively.

The geometry illustrated in Figure 5.12, together with the parent material yield stress σ_b and the minimum HAZ yield stress σ_{min} from the tensile testing, are used for the calculations of load-bearing capacity and the necessary increase in cross-sectional area ΔA.

Loading perpendicular to weld

If we apply a load perpendicular to the welding, as shown in Figure 5.12 a), the load-bearing capacity can be calculated by multiply the minimum value of HAZ yield stress σ_{min} and the cross-section area (dW). Doing that calculation, the load that can be apply to the component is equal to 28 kN. Considering that result, if we do the same for the parent material, the resulting lead is equal to 63 kN.

ΔA is the necessary increase in cross-sectional area to maintain the load-bearing capacity after HAZ softening. The general expression for the load that can be apply is:

$$P = \sigma_b A \tag{15}$$

$$P = \sigma_{min}(A + \Delta A) \tag{16}$$

The first equation is for the parent material, the second is in the case of welded plate.

Solving the system, where the P is wanted to be constant, the increasing in area can be easy calculated.

$$\frac{A'}{A} = \frac{\sigma_b}{\sigma_{min}} \tag{17}$$

Where A' is the total area needed in the welding case. The result of this calculation is 2,25, which means that the cross-section area should be more than twice the one of the parent material case.

Loading parallel to weld

The loading parallel case is more complex than the previous one. A model has been done by Myhr and Grong [29] to calculate the equivalent cross section area considering the strength profile which is present in the proximity of the welding. In order to evaluate the load-bearing capacity of the joints under this condition, the equivalent reduced strength zone $2y_{red}^{eq}$ of minimum strength σ_{min} has to be calculated by solving the integral in the Equation (6); using as input the data from the yield profile previously calculated. The result of this calculation is shown in the following graph (Figure 5.13).

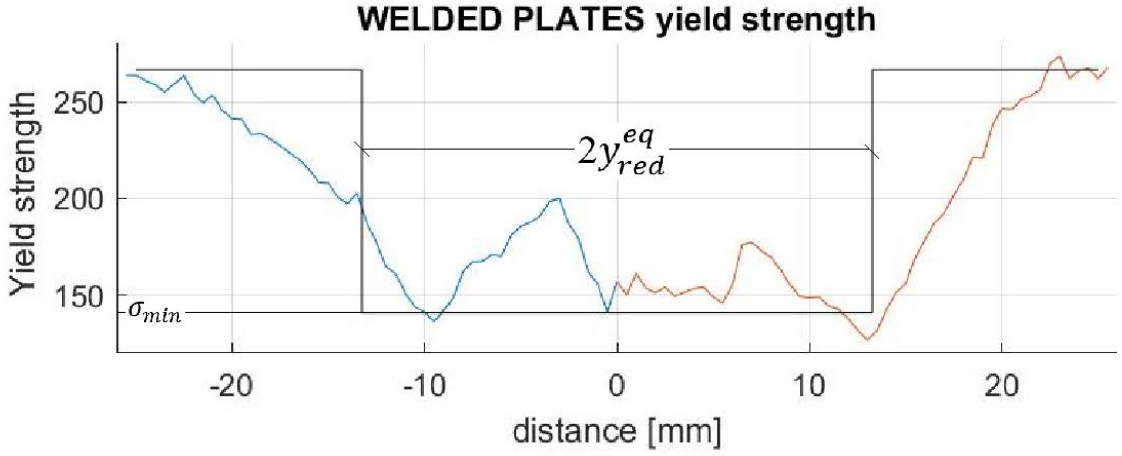

Figure 5.13 Approximate equivalent half width of reduced strength zone y_{red}^{eq} of minimum strength σ_{min}, based on the yield stress profiles of the GMAW.

Then the increase in the cross-section of the component ($\Delta A/A$) to compensate for the associated strength loss is given by the following relationship:

$$\frac{\Delta A}{A} = \frac{2y_{red}^{eq}(1 - \frac{\sigma_{min}}{\sigma_b})}{w_0} \quad (18)$$

Where w_0 is the width of the welded component (in the following assumed constant and equal to 100 mm). The necessary input data required to perform the calculations are summarized in the following Table 5.4.

Table 5.4: Summary of input data used to calculate the relative increase in the cross-sectional area $\Delta A/A$.

w_0	100 [mm]
σ_b	317 [MPa]
σ_{min}	141 [MPa]
y_{red}^{eq}	13.2 [mm]

By inserting the appropriate input data from the previous Table 5.4 into Equation (18), a necessary increase in cross-sectional area of 14% is calculated in the GMAW case under consideration. The results from all loading capacity calculations are summarized in the following Table 5.5.

Table 5.5:Summary of all results from the load-bearing capacity calculations.

y_{red}^{eq}	13 [mm]
A'/A	85 %
A	400 [mm^2]
A_{red}	341 [mm^2]
β	0,44 []
$\Delta A/A$	14 %

Where β is the ratio between σ_{min} and σ_b. From this model, it has been calculated that the equivalent cross-section area of a welded plate is equal to the 85% of the one made of parent material. Note that this data is valid considering an original cross section area of 400 mm^2.

6 Conclusions

From the analysis of the results obtained it can be concluded the following:

The hardness profile is as expected, the typical “M” shape is due to the microstructure modifications that occur because of the heat input during the fusion welding. The lower value of hardness found in the HAZ brings to a reduction in strength that has to be taken into account in the structural design. This reduction in strength has been proved also with the tensile test: all the welded specimens broke as expected in the HAZ, where the point of minimum hardness was measured.

The bend test and the metallography of the welding reveals the good quality of the GMAW studied: the specimens didn’t show the formation of cracks during the bend test, and the amount of welding defects is very low, the pores ratio is lower than the maximum value indicated in the standard for this kind of welding.

From the fatigue test it has been observed that the model provided for the study of misaligned specimens is useful and it is in accordance with the results obtained. In particular it has been seen that using the correction indicated in the standard, the S-N curve becomes similar to the standard one.

The Charpy impact test confirmed what found with the tensile test, showing how the more ductile behavior of the softened HAZ brings to a higher energy absorption capacity.

The aluminum alloy tested as parent material has a high mechanical strength: the values of yield strength and UTS are high. The results are overall in accordance to what indicated in literature for this kind of aluminum alloy.

7 Bibliography

[1] " A.R. Eivani and A. Karimi Taheri. Modeling age hardening kinetics of an al–mg– si–cu aluminum alloy. Journal of Materials Processing Technology, 205(1–3):388 – 393, 2008.".

[2] M.F. Ashby, Engineering materials 2 : an introduction to microstructures and processing, 2013.

[3] I. J.Polmear. Light Alloys - From Traditional Alloys to Nanocrystals. Elsevier, 2006.

[4] J.R. Davis, Alloying-Understanding the basics. ASM International, Materials Park, OH 2001.

[5] N.R. Mandal, Aluminum welding, Woodhead Publishing Limited, Cambridge England.

[6] "C. R. Breivik. Mechanical properties of gas metal arc and friction stir AA6082-T6 Weldments, MSc Thesis, Norwegian University of Science and Technology, Department of Materials Science and Engineering, Trondheim, Norway, June, 2013".

[7] "Leader, A. Aluminium production. [cited 2016 March]; Available from: http://www.aluminiumleader.com/production/aluminum_production/.".

[8] "AluPro, Aluminium and the Carbon Economy. 2015. p. Aluminium life cycle.".

[9] "P.Ponzi, Caratterizzazione meccanica delle saldature per attrito con utensile rotante (FSW), Tesi di dottorato, 2005".

[10] "J.V.Jakobsen. Microstructure and Mechanical Properties of Welded AA6082 Aluminium Alloys, MSc Thesis, Norwegian University of Science and Technology, Department of Materials Science and Engineering, Trondheim, Norway, June, 2016".

[11] "Kuijppers N.C.W. Kinetics of the β-AlFeSi to α-Al(FeMn)Si. Technische Universiteit Delft 2004".

[12] "C. Hsu et al. / Materials Science and Engineering A304–306 (2001) 119–124".

[13] "Mathers, Gene. (2002). Welding of Aluminium and Its Alloys - 2.2 Strengthening Mechanisms . Woodhead Publishing. Online version available at:https://app.knovel.com/hotlink/pdf/id:kt002Y8N8R/welding-aluminium-its/strengthening-mechanisms".

[14] Sun, "F. Sun, Y.F. Gu, J.B. Yan, Z.H. Zhong, M. Yuyama. Phenomenological and microstructural analysis of intermediate temperatures creep in a NieFe-based alloy for advanced ultra-supercritical fossil power plants. 2015".

[15] "Mathers, Gene. (2002). Welding of Aluminium and Its Alloys - 1.2 Characteristics of Aluminium . Woodhead Publishing. Online version available at:https://app.knovel.com/hotlink/pdf/id:kt002Y8N38/welding-aluminium-its/characteristics-aluminium".

[16] "Mathers, Gene. (2002). Welding of Aluminium and Its Alloys - 7.2 Process Principles . Woodhead Publishing. Online version available at: https://app.knovel.com/hotlink/pdf/id:kt002Y8O56/welding-aluminium-its/process-principles".

[17] "O.R. Myhr, Ø. Grong, H.G. Fjær, and C.D. Marioara. Modelling of the microstructure and strength evolution in al–mg–si alloys during multistage thermal processing. Acta Materialia, 52(17):4997 – 5008, 2004.".

[18] "C. R. Breivik. Preliminary Benchmarking of the HYB (Hybrid Metal Extrusion & Bonding) Process for Butt Welding of AA6082-T6 Plates Against FSW and GMAW.," *MSc Thesis, Norwegian University of Science and Technology, Department of Materials Science and Engineering, Trondheim, Norway, July, 2017.* .

[19] "O. R. Myhr & Ø. Grong (2009) Novel modelling approach to optimisation of welding conditions and heat treatment schedules for age hardening Al alloys, Science and Technology of Welding and Joining, 14:4, 321-332, DOI: 10.1179/136217109X425829".

[20] "Marte Brynjulfsen, Fatigue of Extruded AA6082 and AA7108, June 2015.".

[21] "Miller, Brett, ASM International, 2013".

[22] "Miller, Brett. (2013). Understanding how Components Fail (3rd Edition) - 9. Ductile Fracture. ASM International.".

[23] "Miller, Brett. (2013). Understanding how Components Fail (3rd Edition) - 8.3 Microstructural Aspects of Brittle Fracture. ASM International.".

[24] "Miller, Brett. (2013). Understanding how Components Fail (3rd Edition) - 10.2 Microscopic Characteristics of Fatigue Fracture. ASM International.".

[25] "Standard Test Methods for Vickers Hardness and Knoop Hardness of Metallic Materials. 2016, ASTM International.".

[26] "NS-EN ISO 5173:2010".

[27] "ASTM E8/E8M − 16a".

[28] "Standard Test Methods for Notched Bar Impact Testing of Metallic Materials. ASTM E23-16b.".

[29] "O. R. Myhr and Ø. Grong, Novel modelling approach to optimisation of welding conditions and heat treatment schedules for age hardening Al alloys, Science and Technology of Welding and Joining. 14(4), (2009) 321-332".

[30] "http://www.hobartbrothers.com/downloads/aluminum_selecti_1lOo.pdf".

8 Appendix

Dokument ID 754-7 bil. till 167
Utfärdad av Ulf Svensson
Giltigt from 2005-10-13
Utgåva 02

sapa:

PROVNINGSINTYG
ABNAHMEPRUFZEUGNIS
INSPECTION CERTIFICATE

Type EN 10 204 - 3.1

Blad -Sheet -Blatt Nr-No

Tjänsteställe, handläggare - Our reference - Unser Zeichen	Datum - Date	Intyg nr - Certificate No - Zeugnis Nr
Jan Wallin	2013-03-14	30212

Köpare - Customer - Käufer	SAPA ordernr/pos - SAPA order No - SAPA Order Nr/Pos
Apply Leirvik AS	2907529-2905212-2905932-2905935-2905936
	Varuslag - Material - Materialform: Profiles
	Dimension: 362667
Ordernr/ref - Order No/ref - Bestellung Nr/Ref: cert.30232	Legi/tillst - Alloy/Temper - Leg/Zust: EN AW -6082-T6
Märkn - Mark - Bezeichnung: LMT 250A	Norm - Specification

SAMMANSÄTTNING %, garantivärden -
CHEMICAL COMPOSITION %, guaranteed values - CHEMISCHE ZUSAMMENSETZUNG %, garantierte Werte — EN 573-3

Charge nr.	Si	Fe	Cu	Mn	Mg	Cr	Zn	Ti	Al
130225-2-A	0,97	0,21	0,03	0,48	0,64	0,00	0,00	0,02	Rem
130124-4-A	0,99	0,21	0,03	0,48	0,63	0,00	0,00	0,02	Rem
130125-1-A	1,00	0,21	0,03	0,47	0,64	0,00	0,00	0,02	Rem
130124-3-A	0,97	0,20	0,02	0,48	0,64	0,00	0,00	0,02	Rem
130208-3-A	1,00	0,21	0,03	0,48	0,64	0,00	0,00	0,02	Rem
130208-1-A	1,00	0,21	0,02	0,48	0,64	0,01	0,01	0,02	Rem

HÅLLFASTHET etc, provningsresultat -
MECHANICAL PROPERTIES etc, test results - FESTIGKEITSEIGENSCHAFTEN usw, Prüfresultate — EN 755-2

Prov Nr / Specimen No / Probe Nr	Rp 0,2 N/mm²	Rm N/mm²	A 50 %	A 5 %	HV 20			
1	313	335	10					
2	315	337	10					
3	316	339	10					
4	314	337	11					
5	318	341	10					
6	312	341	10					
7	320	341	10					
8	321	342	10					
9	317	346	10					
Normfordr / Spec.limits / Forderungen	250	290	6					

Anm:

Vi intygar att levererade produkter överensstämmer med bestämmelserna i beställningen
We certify that the above mentioned products comply with the terms of the order contract
Wir bestätigen, dass die Lieferung den Vereinbarungen der Bestellannahme entspricht.

Sapa Profiler AB / Quality department
Namn
Jan Wallin

Sida 1 av 1

Utskriven 2013-03-15

Figure 8.1: Parent material certificate.

APPLY LEIRVIK

PRODUCTION TEST
DATA RECORD

WPS NO		CONTR.		PROJECT	Hybond.
WELDING PROCESS DATA			TEST MATERIAL DATA		
PASS	PROCESS	CONSUMABLES	~~FLUX~~/GAS	SPEC.	
Tack	131	MigWeld 5183	Argon 4.0	Grade	6082-T6
Root	"	"	"	Thickness	4mm
Hot pass	"	MIGWELD 5183	"	Dimension	3000 mm
Fill	"	"	"	Test pos	PA
Cap				Preheat	13°C
Root/ Back				Root gap: 0 Root face: 1	Bevel V Angel: 60°
Type of test		Date start	4/11-14	Date finish	5/11-14
Welder	1160 Maj	Insp. Sign			

Pass	Elec. Dim	Amps Min-max	Volt Min-max	Travel Speed	Wire Speed	Roll	Rot	Interpass temp	Heat inp Kj/ mm	Flux flow	Gas flow Back	Gas Flow shield
1a	1,2	180	22			280	40		0,49			20 l/min
1b	"	180	22			390	35		0,43			"
1c	"	189	22,2			400	38		0,4			"
1d	"	"	22			480	41		0,43			"
1e	"	"	"			390	37		0,39			"
1f	"	"	"			405	39		0,4			"
1g	"	"	"			410	32		0,32			"
1h	"	"	"			415	40		0,4			"
2a	"	165	22,2			600	66		0,49			"
2b	"	"	"			380	32		0,3			"
2c	"	170	22			420	28		0,25			"
2d	"	"	"			410	24		0,22			"
2e	"	"	"			410	23		0,22			"
2f	"	"	"			400	21		0,22			"
2g	"	"	"			400	18?					"
3a	"	168	"			580	66		0,38			"
3b	"	"	"			800	86		0,4			"
3c	"	172	"			900	79		0,37			"
3d	"	"	"			800	76		0,36			"
4a	"	"	"			270	40		0,56 Kort reparasjon!			"

Rot løsmm

NB! →

Remarks: Wire MigWeld 5183 CH8718 Los 3814 Plate: 751627 Parcel 11

PT-Production
WPQ-Welding procedure qualification
WPT –Welders performance test
ROLL Run Out Length
ROT- Run Out Time

Figure 8.2: Welding data sheet.

MIG WELD

CERTIFICAT DE RECEPTION / ABNAHMEPRÜFZEUGNIS / INSPECTION CERTIFICATE

SUIVANT NF EN 10204 -3.1

CLIENT / CUSTOMER / KUNDE :	**NORSK SVEISETEKNIKK AS**
DIAMETRE : **1.2 MM**	DATE / DATUM : **18.09.2014**
DESIGNATION MIGWELD : **ML 5183** DESIGNATION CLIENT : **5183**	LOT / CHARGE / BATCH : **8718**

COMPOSITION CHIMIQUE LIMITE % / CHEMICAL COMPOSITION LIMITS %										UNSPECIFIED ELEMENTS	
	Si	Fe	Cu	Mn	Mg	Cr	Zn	Ti	Zr	EACH	TOTAL
maxi mini	0,40	0,40	0,10	1,00 0,50	5,20 4,30	0,25 0,05	0,25	0,15	-	0,05	0,15
Be ≤ 0.0003 - Al remainder											

ANALYSE CHIMIQUE REELLE SELON FOURNISSEUR / FURTHER SUPPLIERS ANALYSIS / NACH ANALYSE DES LIEFERANTEN											
	Si	Fe	Cu	Mn	Mg	Cr	Zn	Ti	Zr	Be	Al
	0,04	0,100	<0,01	0,62	4,800	0,080	<0,01	0,08	-	<0,0001	Solde

CARACTERISTIQUE MECANIQUE / MECHANICAL PROPERTY			
CAST (MM):	HELICE(MM):	Rm (MPa) :	

.Tests de fumée effectués lors du contrôle qualité / Smoke tests effected.

.Nous certifions que l'analyse ci-dessus est conforme aux normes suivantes:

.We hereby certify that the above chemical analysis complies with the following specifications:

.Wir bestätigen hiermit,daß die o.g.chemische Analyse mit den folgenden Normen übereinstimmt:

NF EN ISO 18273				
Al 5183 / Al Mg4,5 Mn0,7				

Etabli par :
Le :
Visa :

QUAL I 1-1 Rev0 02.06.2003

A Longvic le : 18.09.2014
D. LORDEL
Responsable Assurance Qualité

Figure 8.3: Filler material certificate

Table 8.1: Filler metals in welding of aluminum [30].

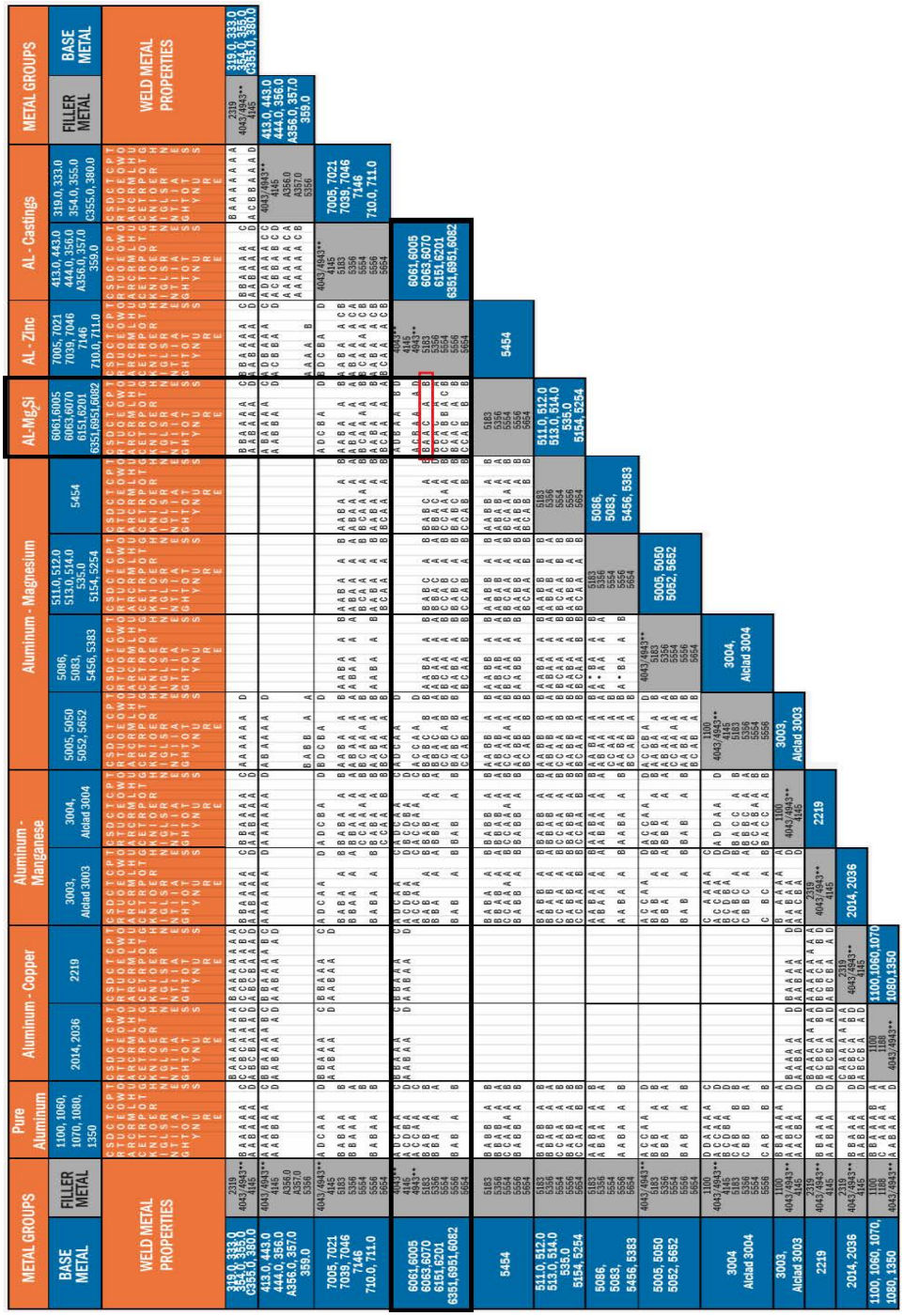

Table 8.2: Properties in welding of aluminum [30].

WELD METAL PROPERTIES	
CRACKING	**CRACK SENSITIVITY** The Probability of Hot Cracking - this rating is established through use of crack sensitivity curves (Developed by Alcoa) and the consideration of filler metal and base metal chemistry combinations. There are levels of various alloying elements within aluminum that have been identified as seriously affecting hot cracking susceptibility during weld solidification. This rating is primarily based on the probability of producing a weld outside these crack sensitive chemistry ranges.
STRENGTH	**STRENGTH** Ratings are for fillet weld and groove weld strength in the as welded condition. Groove welds – Any specified filler metal with a rating can provide minimum transverse tensile strength in groove welds that will meet the as-welded strength of the base material. Fillet welds – Ratings provided are for fillet weld shear strength.
DUCTILITY	**DUCTILITY** This characteristic of the completed weld may be of consideration if forming operations are to be used on a completed weldment during fabrication. Note: Testing procedure requirements for guided bend tests may need to be adjusted to accommodate the varying ductility of filler metals (AWS D1.2).
CORROSION	**CORROSION RESISTANCE** This variable may be a consideration for some environmental conditions. The rating is based on exposure to fresh and salt water environments and is not associated with a specific chemical exposure. It gives an indication as to the possibility of galvanic corrosion due to the difference in the electrode potential between the base metal and the filler metal. For consideration for other environmental and chemical exposures contact MAXAL.
TEMPERATURE	**ELEVATED TEMPERATURE SERVICE** This rating is based on the reaction of some filler metals when exposed to sustained elevated temperature: 150°F to 350°F (66°C to 180°C). If 5xxx series base metal or filler metal with more than 3% magnesium content are subjected to prolonged exposure to these temperatures, precipitate can form within them that is highly anodic to the aluminum-magnesium matrix. It is this continuous grain boundary network of precipitate that produces susceptibility to stress corrosion cracking (SCC) and the potential for premature component failure.
COLOR	**COLOR MATCH AFTER ANODIZING** Base metal and filler metal color match after post-weld anodizing can be of major concern in cosmetic applications. Some filler metals closely match the base metal color after anodizing and others will react to the anodizing process by changing to a color very different to that of the base metal.
PWHT	**POST WELD HEAT TREATMENT** This rating applies to the ability of a weld to respond to post-weld heat treatment in the form of solution heat treatment and artificial aging. An "A" rating indicates that the filler metal is heat treatable and will therefore respond to post weld heat treatment even without dilution of the base metal. A "B" rating indicates that the filler metal is not heat treatable. However, it may be used for applications requiring post weld heat treatment but with the understanding that the weld may or may not acquire substantial increase in strength dependent on the joint design, welding procedure, and resultant amount of dilution of base metal obtained during welding. A "C" rating requires consultation with MAXAL®. No rating indicates that the filler metal is not heat treatable and that it should not be used for applications requiring post weld heat treatment as it may result in substantial reduction in weld performance.
TOUGHNESS	**TOUGHNESS** This rating applies to the ability of an aluminum weldment to deform plastically in the presence of stress raisers without low-energy initiation and propagation of cracks. The most useful test data is from tear resistance testing expressed in unit propagation energy of measured crack lengths. In structural design, notch toughness is becoming more emphasized by designers to facilitate the ability to inspect highly stressed structures and find cracks in weldments before catastrophic failure occurs. It may also be a design consideration if fatigue and impact loading are factors directly associated with a weldment.

HARDNESS DIAGRAMS

Table 8.3: Hardess profile from the first test.

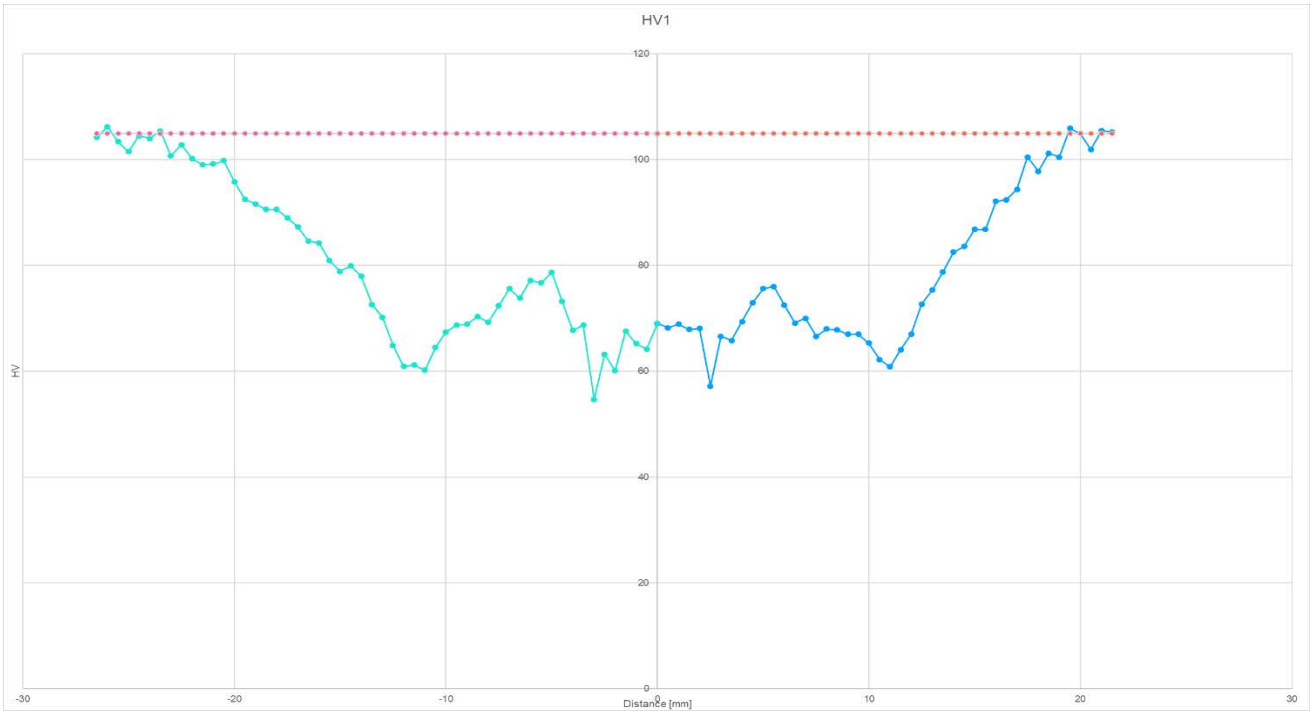

Table 8.4: Hardness profile from the second test.

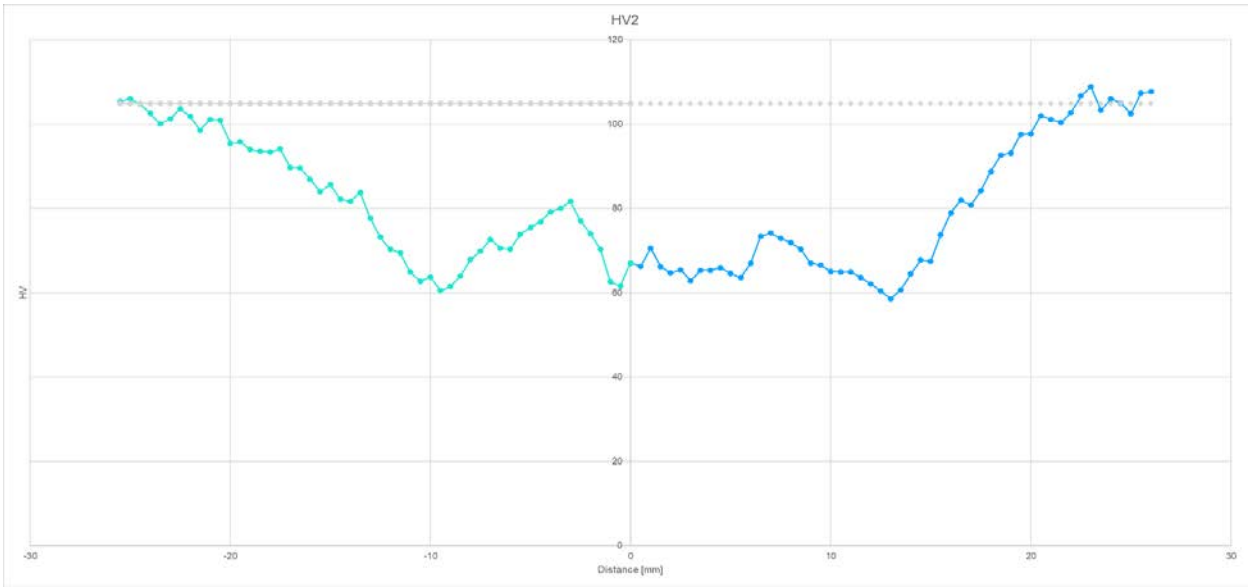

Table 8.5: Hardness profile from the third test.

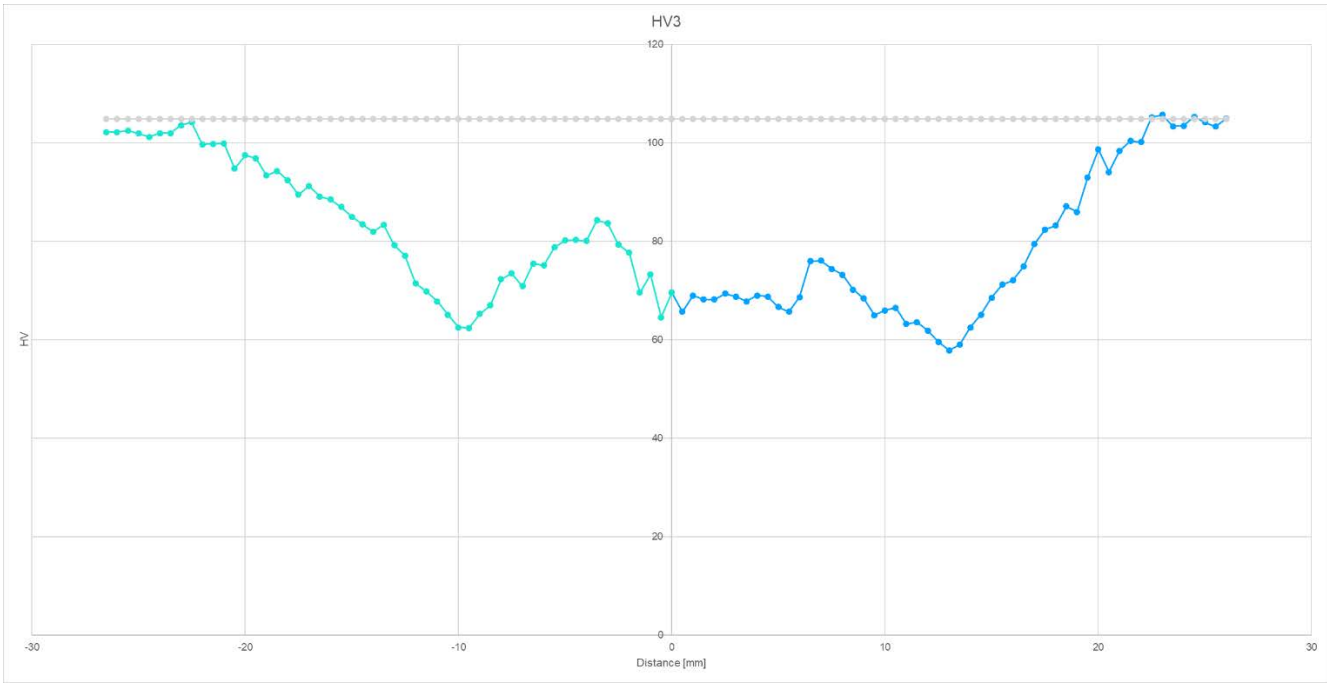

Table 8.6: Average hardness profile of the welding.

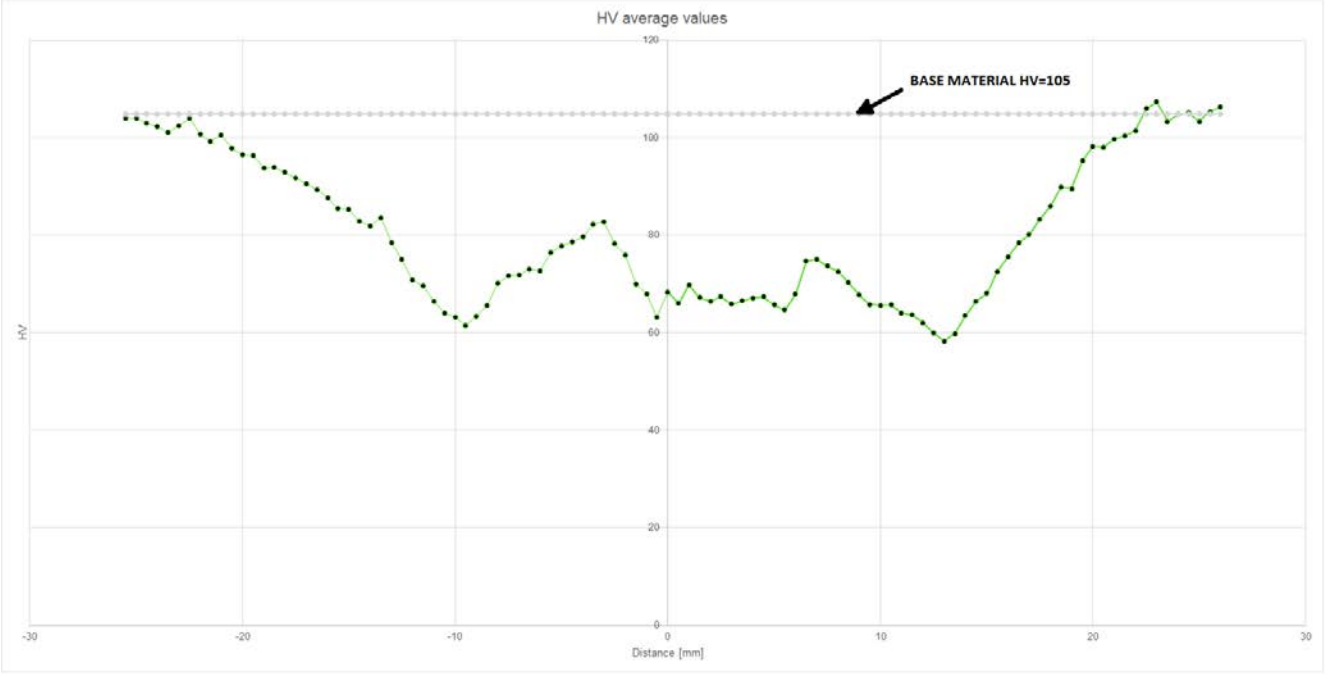

Table 8.7:HV values of parent material sample.

PARENT MATERIAL	
POINT	**HV**
0	104,9
0,5	104,2
1	102,7
1,5	105,8
2	103,1
2,5	107,4
3	108,8
3,5	105,1
4	104,3
4,5	104,3
5	102,8
5,5	104,4
6	105,2
6,5	105,5
AVERAGE	104,9
YIELD STRENGTH	267

Table 8.8: Hardness values of the welding profile.

FIRST SET				SECOND SET				THIRD SET			
Distance [mm]	**HV**	**Distance [mm]**	**HV**	**Distance [mm]**	**HV**	**Distance [mm]**	**HV**	**Distance [mm]**	**HV**	**Distance [mm]**	**HV**
0	69	0	69	0	67,1	0	67,1	0	69,6	0	69,6
0,5	68,2	-0,5	64,2	0,5	66,3	-0,5	61,6	0,5	65,7	-0,5	64,6
1	68,9	-1	65,2	1	70,6	-1	62,6	1	69	-1	73,3
1,5	67,9	-1,5	67,6	1,5	66,2	-1,5	70,4	1,5	68,2	-1,5	69,6
2	68,1	-2	60,1	2	64,7	-2	74	2	68,2	-2	77,7
2,5	57,2	-2,5	63,2	2,5	65,4	-2,5	77,1	2,5	69,4	-2,5	79,4
3	66,6	-3	54,7	3	62,9	-3	81,7	3	68,8	-3	83,7
3,5	65,8	-3,5	68,7	3,5	65,3	-3,5	80	3,5	67,8	-3,5	84,3
4	69,4	-4	67,7	4	65,3	-4	79,2	4	69	-4	80,1
4,5	72,9	-4,5	73,2	4,5	66	-4,5	76,9	4,5	68,8	-4,5	80,3
5	75,6	-5	78,7	5	64,6	-5	75,5	5	66,7	-5	80,2
5,5	76	-5,5	76,7	5,5	63,6	-5,5	73,9	5,5	65,7	-5,5	78,8
6	72,5	-6	77,2	6	67	-6	70,4	6	68,7	-6	75,1
6,5	69,1	-6,5	73,8	6,5	73,4	-6,5	70,6	6,5	76	-6,5	75,5
7	70	-7	75,6	7	74,2	-7	72,7	7	76,1	-7	70,9
7,5	66,6	-7,5	72,4	7,5	72,9	-7,5	69,9	7,5	74,4	-7,5	73,5
8	68	-8	69,3	8	71,9	-8	67,9	8	73,2	-8	72,3
8,5	67,8	-8,5	70,3	8,5	70,4	-8,5	64	8,5	70,2	-8,5	67
9	67	-9	68,9	9	67,1	-9	61,5	9	68,4	-9	65,3
9,5	67	-9,5	68,7	9,5	66,6	-9,5	60,5	9,5	65	-9,5	62,4
10	65,3	-10	67,4	10	65,1	-10	63,7	10	66	-10	62,5
10,5	62,2	-10,5	64,5	10,5	64,9	-10,5	62,8	10,5	66,5	-10,5	65,1
11	60,8	-11	60,2	11	65	-11	64,9	11	63,2	-11	67,8
11,5	64,1	-11,5	61,2	11,5	63,6	-11,5	69,5	11,5	63,6	-11,5	69,8
12	67	-12	60,9	12	62,1	-12	70,3	12	61,9	-12	71,5

12,5	72,7	-12,5	64,9	12,5	60,4	-12,5	73,2	12,5	59,6	-12,5	77,1
13	75,4	-13	70,2	13	58,6	-13	77,7	13	57,9	-13	79,2
13,5	78,8	-13,5	72,6	13,5	60,7	-13,5	83,8	13,5	59	-13,5	83,4
14	82,5	-14	78	14	64,5	-14	81,7	14	62,5	-14	81,9
14,5	83,6	-14,5	79,9	14,5	67,8	-14,5	82,2	14,5	65,1	-14,5	83,5
15	86,8	-15	78,9	15	67,5	-15	85,7	15	68,6	-15	85
15,5	86,8	-15,5	80,9	15,5	73,8	-15,5	84	15,5	71,2	-15,5	87
16	92,1	-16	84,2	16	79	-16	86,9	16	72,1	-16	88,5
16,5	92,4	-16,5	84,6	16,5	82	-16,5	89,6	16,5	74,9	-16,5	89,1
17	94,4	-17	87,3	17	80,8	-17	89,7	17	79,5	-17	91,3
17,5	100,5	-17,5	89	17,5	84,2	-17,5	94,1	17,5	82,4	-17,5	89,5
18	97,8	-18	90,6	18	88,8	-18	93,4	18	83,2	-18	92,4
18,5	101,2	-18,5	90,6	18,5	92,6	-18,5	93,6	18,5	87,1	-18,5	94,3
19	100,5	-19	91,6	19	93,2	-19	94	19	86	-19	93,4
19,5	105,9	-19,5	92,5	19,5	97,6	-19,5	95,8	19,5	93	-19,5	96,9
20	104,9	-20	95,8	20	97,7	-20	95,5	20	98,7	-20	97,5
20,5	101,9	-20,5	99,8	20,5	102	-20,5	100,9	20,5	94,1	-20,5	94,8
21	105,5	-21	99,2	21	101,1	-21	101,1	21	98,4	-21	99,9
21,5	105,2	-21,5	99	21,5	100,4	-21,5	98,6	21,5	100,4	-21,5	99,8
		-22	100,2	22	102,8	-22	101,9	22	100,2	-22	99,7
		-22,5	102,8	22,5	106,7	-22,5	103,6	22,5	105,2	-22,5	104,2
		-23	100,7	23	108,9	-23	101,3	23	105,7	-23	103,6
		-23,5	105,4	23,5	103,3	-23,5	100,1	23,5	103,4	-23,5	102
		-24	104	24	106,1	-24	102,6	24	103,5	-24	102
		-24,5	104,5	24,5	105	-24,5	104,8	24,5	105,3	-24,5	101,2
		-25	101,5	25	102,5	-25	106	25	104,2	-25	101,9
		-25,5	103,4	25,5	107,4	-25,5	105,4	25,5	103,3	-25,5	102,5
		-26	106,2	26	107,7			26	105	-26	102,2
		-26,5	104,2							-26,5	102,2

FATIGUE PARAMETERS AND RESULTS

Table 8.9: Parent material transverse fatigue parameters and results.

SPECIMEN	σ_a	N	F_{MAX}	F_{MIN}	F_M
17	93,65	52000	4800,00	480,00	2640,00
18	92,94	42000	4800,00	480,00	2640,00
19	93,89	38000	4800,00	480,00	2640,00
20	72,84	120000	3733,33	373,33	2053,33
21	73,03	140000	3733,33	373,33	2053,33
22	72,77	138000	3733,33	373,33	2053,33
23	52,03	404000	2666,67	266,67	1466,67
24	52,03	440000	2666,67	266,67	1466,67
25	52,03	360000	2666,67	266,67	1466,67
26	52,11	358000	2666,67	266,67	1466,67
27	116,43	15544	5973,33	597,33	3285,33
28	116,93	14000	5973,33	597,33	3285,33

Table 8.10: Parent material longitudinal fatigue parameters and results.

SPECIMEN	σ_a	N	F_{MAX}	F_{MIN}	F_M
30	116,54	25371	4800,00	480,00	2640,00
31	115,94	25738	4800,00	480,00	2640,00
32	93,32	68782	4800,00	480,00	2640,00
33	93,65	71264	3733,33	373,33	2053,33
34	93,17	84948	3733,33	373,33	2053,33
35	72,09	168920	3733,33	373,33	2053,33
36	72,03	157141	2666,67	266,67	1466,67
37	71,66	154912	2666,67	266,67	1466,67
38	51,71	533058	2666,67	266,67	1466,67
39	51,98	928017	2666,67	266,67	1466,67
40	51,81	455049	5973,33	597,33	3285,33
41	51,89	475557	5973,33	597,33	3285,33

Table 8.11: Welding, fused zone fatigue parameters and results.

SPECIMEN	σ_a	N	F_{MAX}	F_{MIN}	F_M	K_m	σ_{eq}
2	69,31	19247,00	3733,33	373,33	2053,33	1,70	117,65
3	69,20	12831,00	3733,33	373,33	2053,33	1,83	126,87
7	58,79	11895,00	3200,00	320,00	1760,00	1,56	91,50
8	58,40	41767,00	3200,00	320,00	1760,00	1,42	82,67
12	59,51	145845,00	3200,00	320,00	1760,00	1,00	59,51
13	48,63	144510,00	2666,67	266,67	1466,67	1,00	48,63
30	49,84	50988,00	2666,67	266,67	1466,67	1,43	71,14
31	52,30	320928,00	2666,67	266,67	1466,67	1,45	75,66
35	39,80	450412,00	2133,33	213,33	1173,33	1,58	62,69
36	39,51	233440,00	2133,33	213,33	1173,33	1,43	56,43
39	39,58	204014,00	2133,33	213,33	1173,33	1,43	56,53
40	39,10	147036,00	2133,33	213,33	1173,33	1,42	55,65

Table 8.12: Welding, heat affected zone fatigue parameters and results.

SPECIMEN	σ_a	N	F_{MAX}	F_{MIN}	F_M	K_m	σ_{eq}
4	89,8	19422,0	4800,0	480,0	2640,0	1,7	153,6
5	89,7	13246,0	4800,0	480,0	2640,0	1,7	153,6
9	60,1	46260,0	3200,0	320,0	1760,0	1,4	85,8
11	60,2	95150,0	3200,0	320,0	1760,0	1,0	60,2
14	59,9	149172,0	3200,0	320,0	1760,0	1,0	59,9
16	49,9	124749,0	2666,7	266,7	1466,7	1,4	71,3
32	52,4	189581,0	2666,7	266,7	1466,7	1,6	83,6
33	52,3	256512,0	2666,7	266,7	1466,7	1,6	83,4
37	39,7	594803,0	2133,3	213,3	1173,3	1,6	62,3
38	40,0	212535,0	2133,3	213,3	1173,3	1,4	57,2
41	38,9	198451,0	2133,3	213,3	1173,3	1,3	49,7
42	40,1	390200,0	2133,3	213,3	1173,3	1,3	51,6

Table 8.13: Stress-strain curve from the tensile test of the Parent material, transverse to the extrusion direction, specimen code 5.

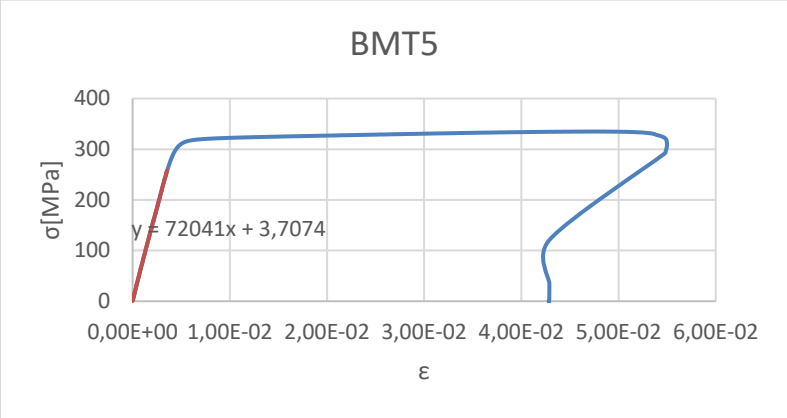

Table 8.14:Stress-strain curve from the tensile test of the Parent material, transverse to the extrusion direction, specimen code 6.

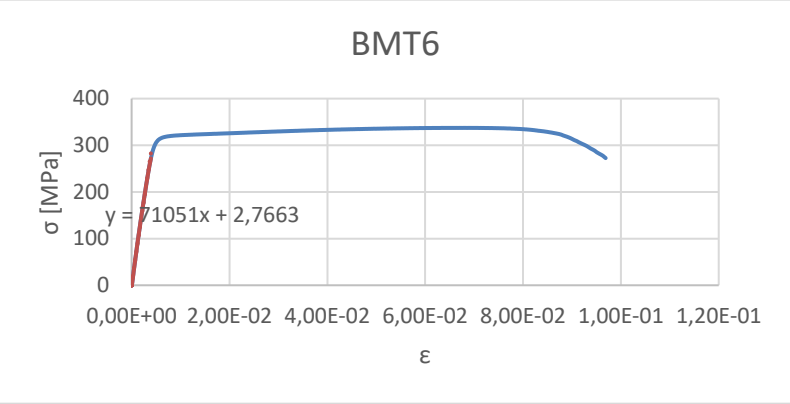

Table 8.15:Stress-strain curve from the tensile test of the Parent material, transverse to the extrusion direction, specimen code 7.

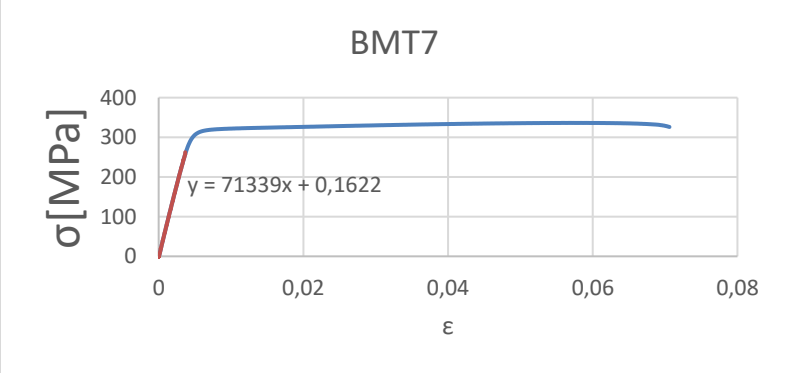

Table 8.16:Stress-strain curve from the tensile test of the Parent material, longitudinal to the extrusion direction, specimen code 8.

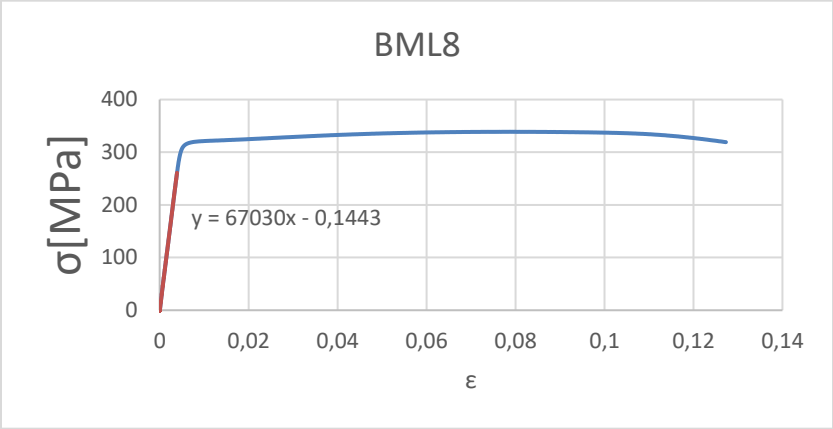

Table 8.17: Stress-strain curve from the tensile test of the Parent material, longitudinal to the extrusion direction, specimen code 9.

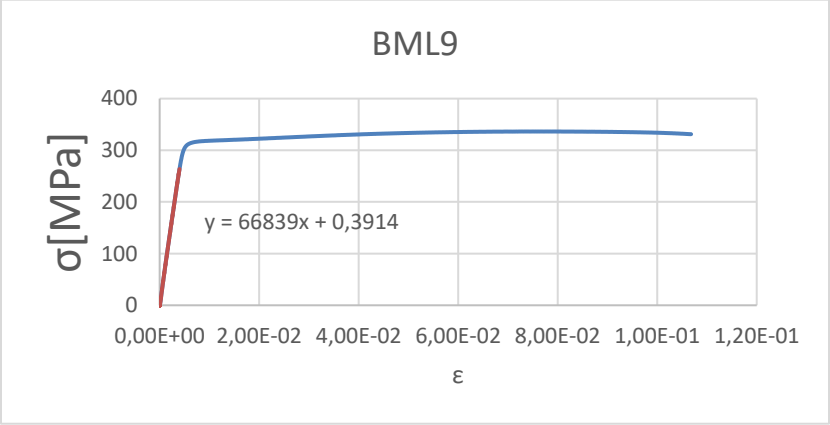

Table 8.18:Stress-strain curve from the tensile test of the Parent material, longitudinal to the extrusion direction, specimen code 10.

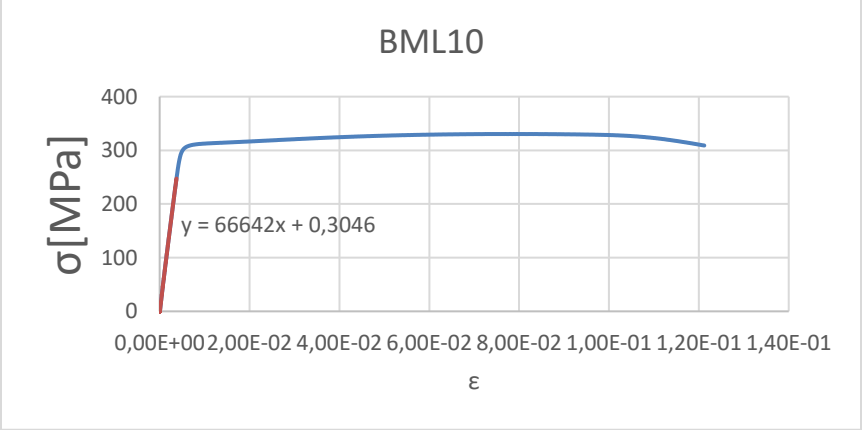

Table 8.19:Stress-strain curve from the tensile test of the Filler material in the fused zone, specimen code FZL9.

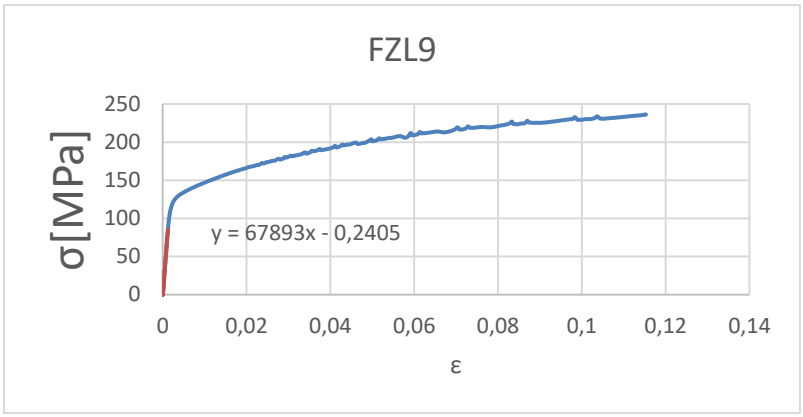

Table 8.20:Stress-strain curve from the tensile test of the Filler material in the fused zone, specimen code FZL29.1.

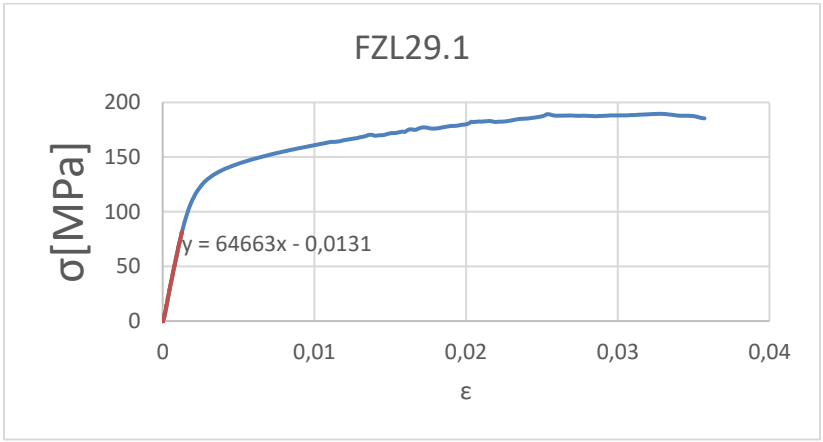

Table 8.21:Stress-strain curve from the tensile test of the Filler material in the fused zone, specimen code FZL29.2.

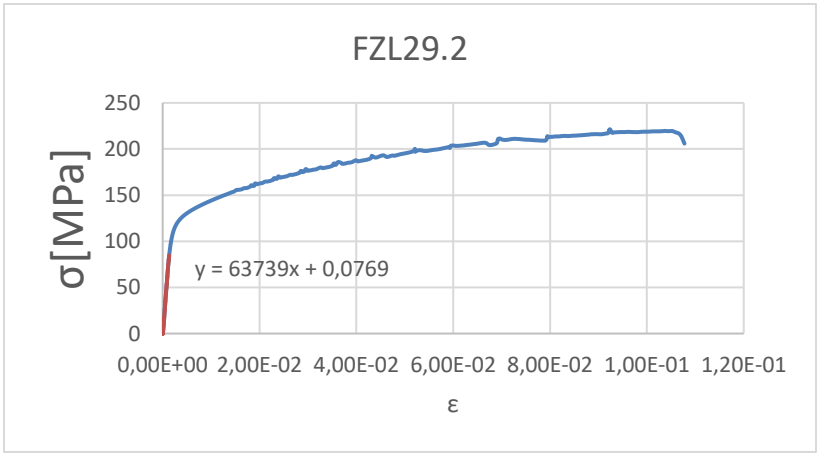

Table 8.22: Stress-strain curve from the tensile test of the heat affected zone longitudinal, specimen code HAZL10.

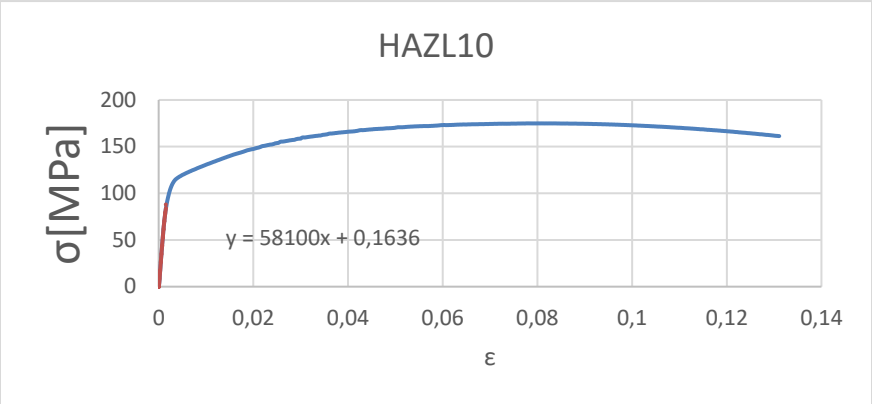

Table 8.23:Stress-strain curve from the tensile test of the heat affected zone longitudinal, specimen code HAZL24.

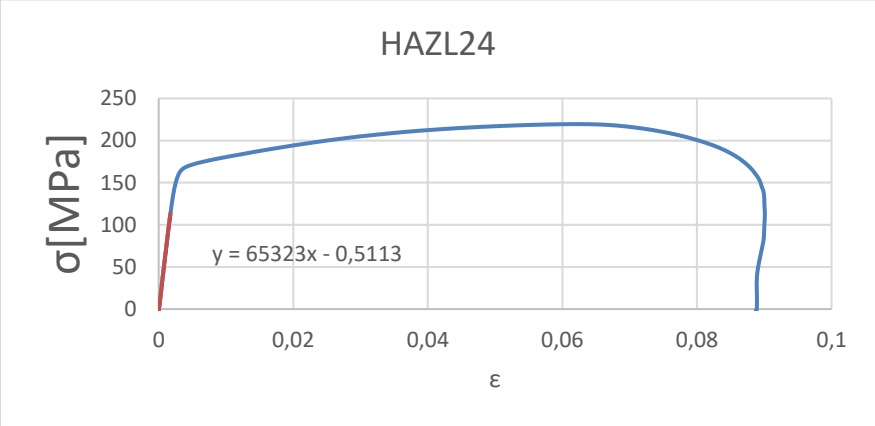

Table 8.24: Stress-strain curve from the tensile test of the heat affected zone longitudinal, specimen code HAZL34.

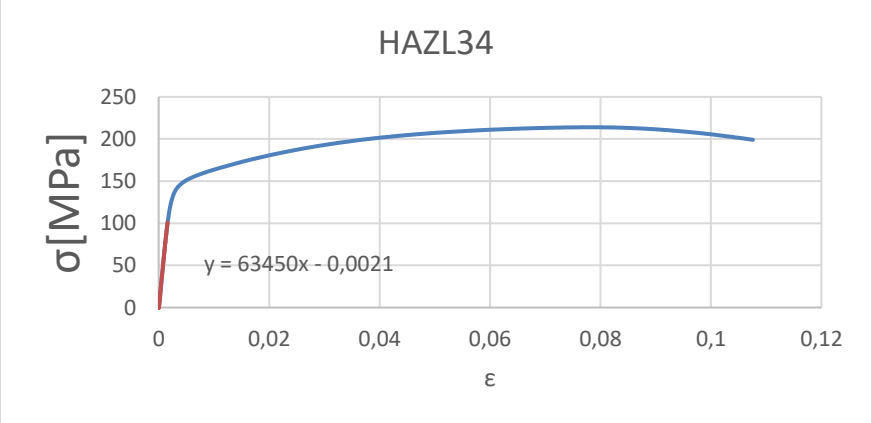

Table 8.25: Stress-strain curve from the tensile test of the fused zone, the reinforcement is machined. Specimen code 15.1.

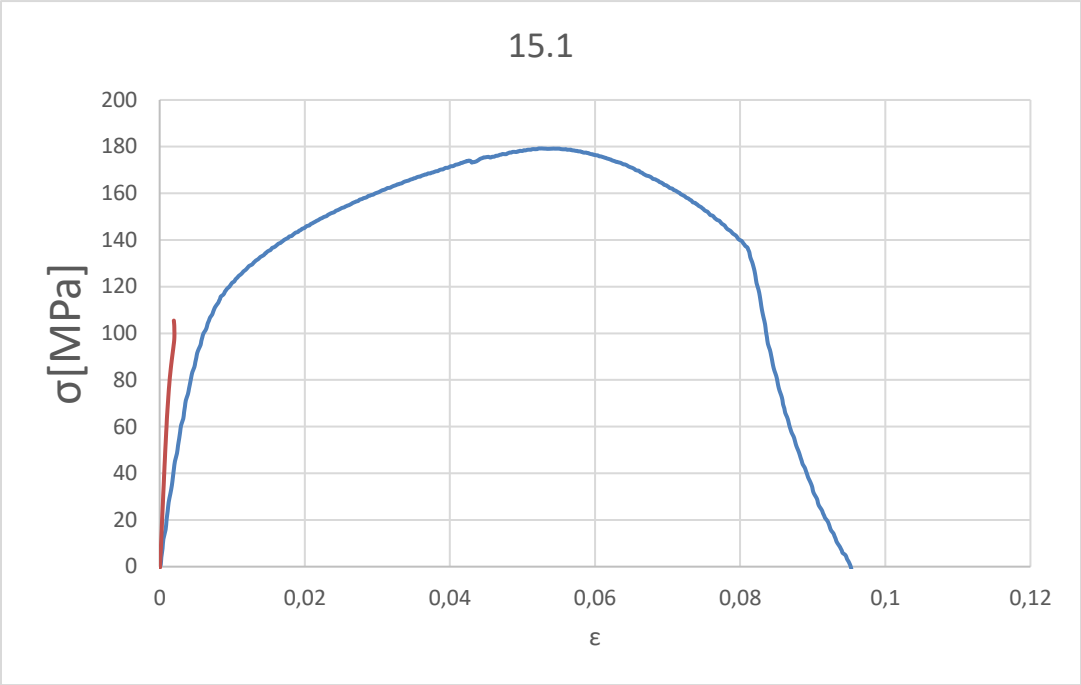

Table 8.26:Stress-strain curve from the tensile test of the fused zone, the reinforcement is machined. Specimen code 15.3.

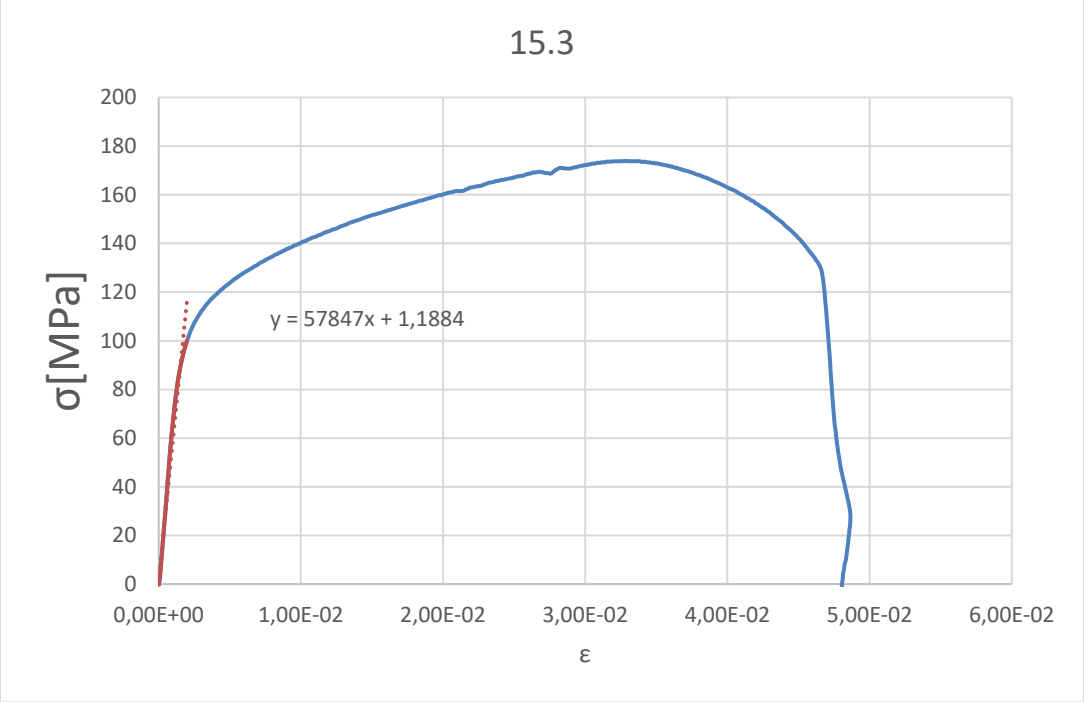

Table 8.27:Stress-strain curve from the tensile test of the heat affected zone, the reinforcement is machined. Specimen code 15.4.

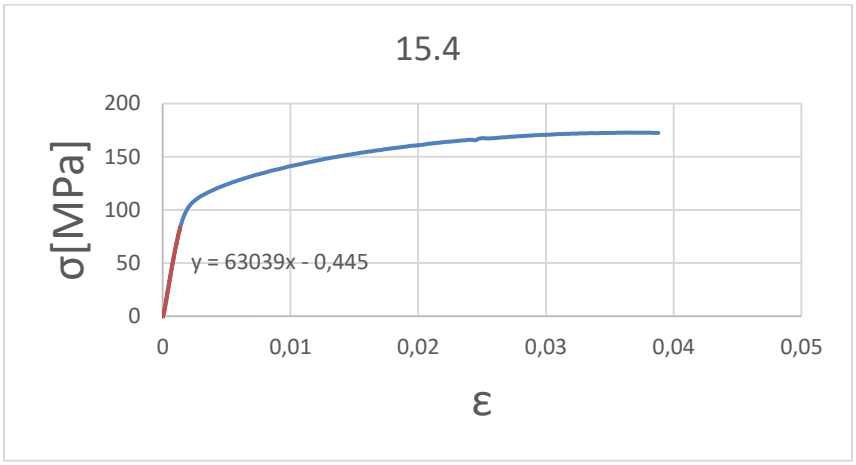

Table 8.28:Stress-strain curve from the tensile test of the heat affected zone, the reinforcement is machined. Specimen code 15.5.

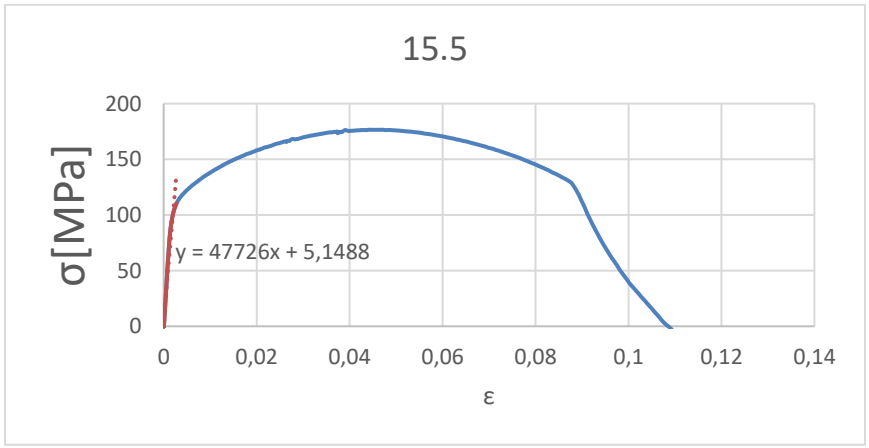

Table 8.29:Stress-strain curve from the tensile test of the heat affected zone, the reinforcement is machined. Specimen code 15.6.

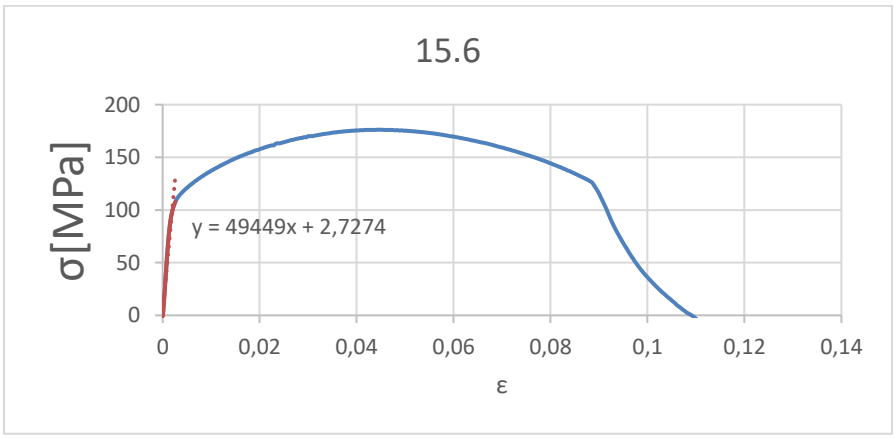

Table 8.30:Stress-strain curve from the tensile test of the fused zone, centered in the FZ but broken in the HAZ. Specimen code FZ22.

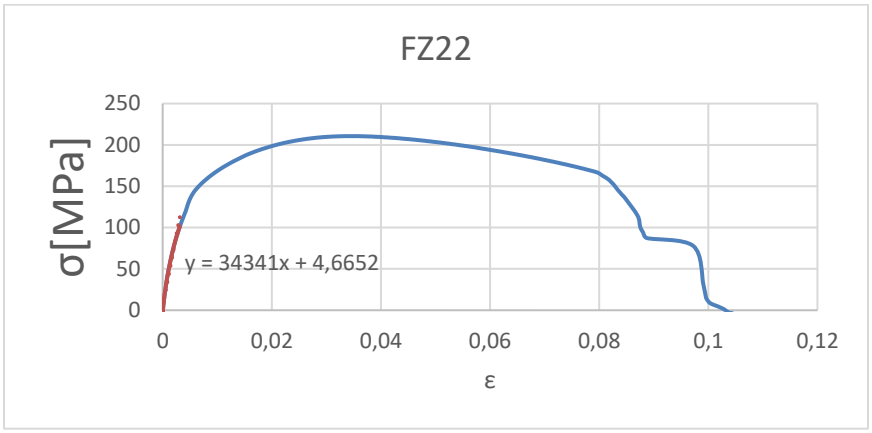

Table 8.31:Stress-strain curve from the tensile test of the fused zone, centered in the FZ but broken in the HAZ. Specimen code FZ23.

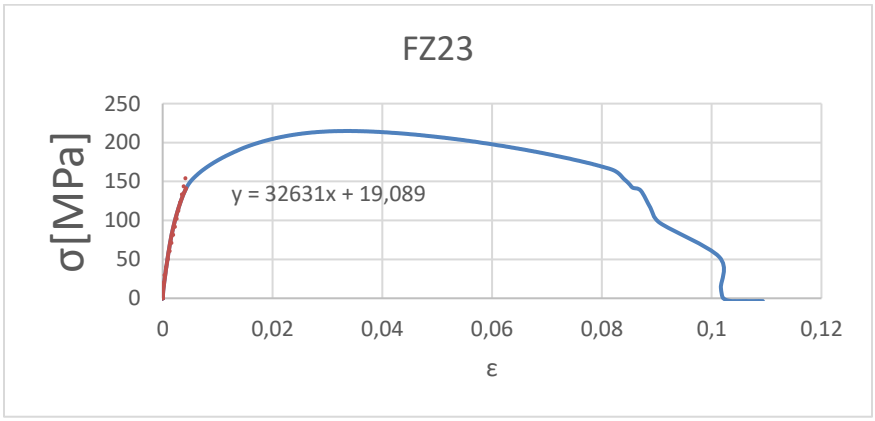

Table 8.32:Stress-strain curve from the tensile test of the fused zone, centered in the FZ but broken in the HAZ. Specimen code FZ25.

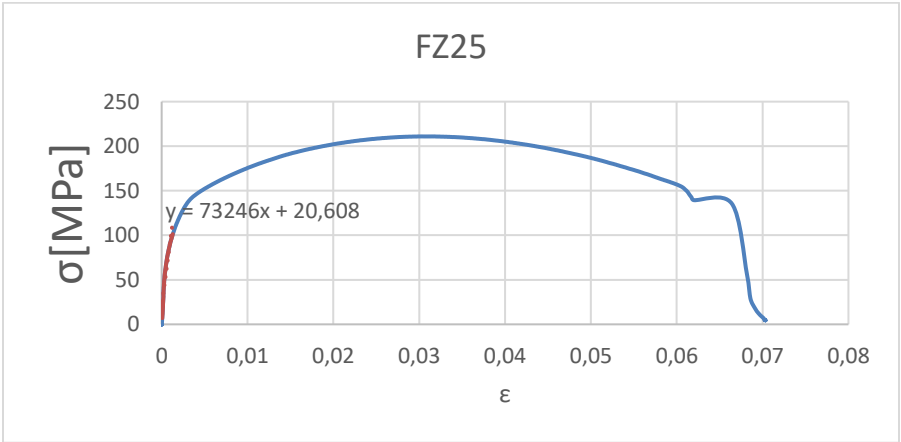

Table 8.33:Stress-strain curve from the tensile test of the heat affected zone, centered in the HAZ and broken in the HAZ. Specimen code HAZ26.

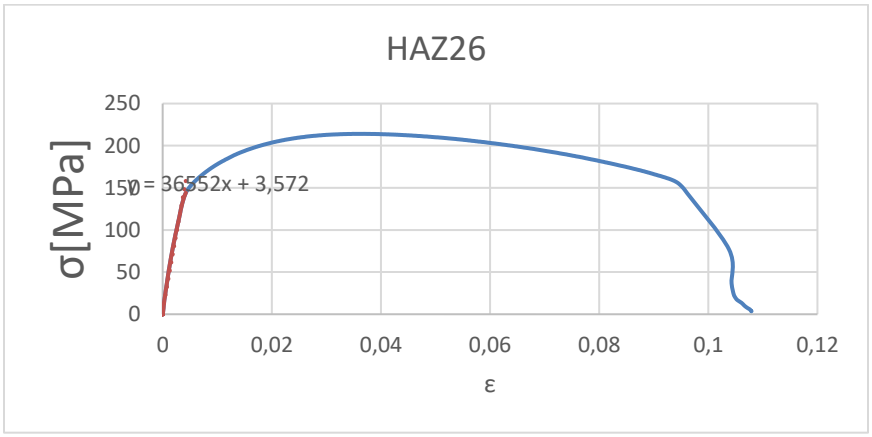

Table 8.34:Stress-strain curve from the tensile test of the heat affected zone, centered in the HAZ and broken in the HAZ. Specimen code HAZ27.

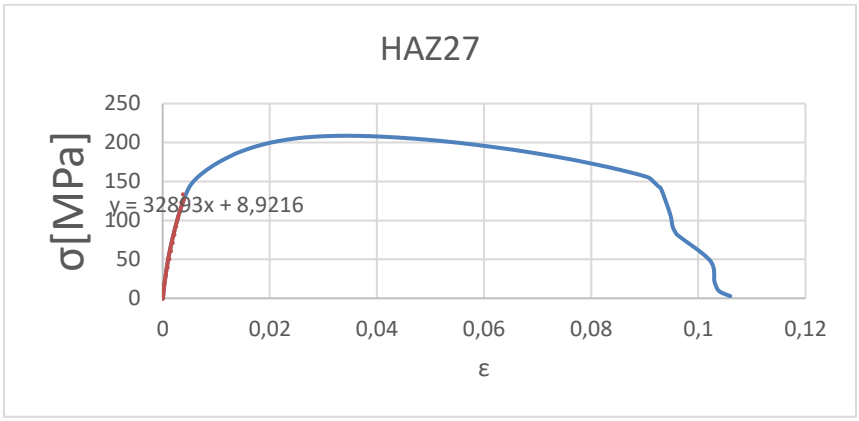

Table 8.35:Stress-strain curve from the tensile test of the heat affected zone, centered in the HAZ and broken in the HAZ. Specimen code HAZ28.

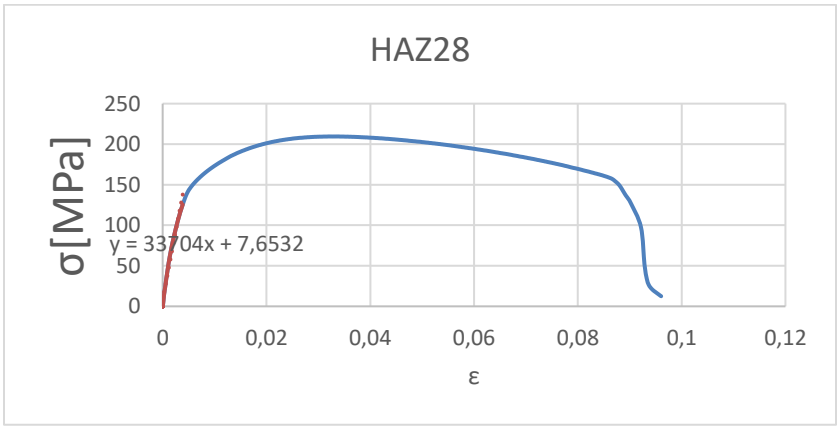

Table 8.36: tensile test specimens codes and geometrical measures.

	CODE	N	NTOT	SPECIMEN CODE	W [mm]	T[mm]	AREA [mm^2]	Misalignment	180-angle
tensile machined	FZ machined	1	1	15.01	5,97	1,95	11,641	178	2
		2	2	15.02	5,98	1,97	11,780	179	1
		3	3	15.03	5,98	1,97	11,780	179	1
	HAZ machined	4	4	15.04	5,97	1,96	11,701	178	2
		5	5	15.05	5,97	1,98	11,820	178	2
		6	6	15.06	5,96	1,95	11,622	178	2
tensile	FZ	7	7	22	5,95	4,03	23,978	173	7
		8	8	23	5,92	4,03	23,857	172	8
		9	9	25	5,94	4,03	23,938	172	8
	HAZ	10	10	26	5,95	4	23,800	172	8
		11	11	27	5,96	4,02	23,959	172	8
		12	12	28	5,94	4	23,760	173	7
	BMT	13	13	5	5,95	3,9	23,205	180	0
		14	14	6	5,94	3,87	22,987	180	0
		15	15	7	5,94	3,86	22,928	180	0
	BML	16	16	8	5,95	3,94	23,443	180	0
		17	17	9	5,94	3,91	23,225	180	0
		18	18	10	5,94	3,9	23,166	180	0
	FZL	19	19	9	5,97	3,98	23,760	180	0
		20	20	29.1	5,96	3,95	23,542	180	0
		21	21	29.2	5,95	4,08	24,276	180	0
	HAZL	22	22	10	5,95	4,03	23,978	180	0
		23	23	24	5,96	4,05	24,138	180	0
		24	24	34	5,96	4,04	24,078	180	0

Table 8.37: Fatigue test specimens codes and geometrical measures.

		CODE	W [mm]	T [mm]	Area [mm^2]	ANGLE [°]	β	K_m
FATIGUE	BM, T	17	5,96	3,87	23,06	0	0,778	1
		18	5,99	3,88	23,24	0	0,776	1
		19	5,96	3,86	23,00	0	0,780	1
		20	5,96	3,87	23,06	0	0,778	1
		21	5,96	3,86	23,00	0	0,780	1
		22	5,95	3,88	23,08	0	0,776	1
		23	5,96	3,87	23,06	0	0,778	1
		24	5,96	3,87	23,06	0	0,7781	1
		25	5,96	3,87	23,06	0	0,7781	1
		26	5,95	3,87	23,02	0	0,7781	1
		27	5,95	3,88	23,08	0	0,7761	1
		28	5,94	3,87	22,98	0	0,7781	1
	BM, L	30	5,95	3,89	23,14	0	0,7741	1
		31	5,96	3,87	23,06	0	0,7781	1
		32	5,96	3,89	23,18	0	0,7741	1
		33	5,96	3,91	23,30	0	0,7701	1
		34	5,95	3,92	23,32	0	0,768	1
		35	5,95	3,94	23,44	0	0,7643	1
		36	5,95	3,9	23,20	0	0,7721	1
		37	5,95	3,88	23,08	0	0,7761	1
		38	5,97	3,88	23,16	0	0,7761	1
		39	5,96	3,88	23,12	0	0,7761	1
		40	5,96	3,87	23,06	0	0,7781	1
		41	5,96	3,89	23,18	0	0,7741	1
	P2b HAZ	4	5,94	4,05	24,0	5	0,7435	1,71
		5	5,96	4,04	24,0	5	0,7453	1,71
		9	5,95	4,03	23,9	3	0,7472	1,42
		11	5,95	4,02	23,9	0	0,7491	1
		14	5,95	4,04	24,0	0	0,7453	1
		16	5,95	4,04	24,0	3	0,7453	1,42
		32	5,95	3,85	22,9	4	0,7821	1,59
		33	5,96	3,85	22,9	4	0,7821	1,59
		37	5,95	4,06	24,1	4	0,7417	1,56
		38	5,95	4,03	23,9	3	0,7472	1,42
		41	5,95	4,15	24,6	2	0,7256	1,27
		42	5,97	4,01	23,9	2	0,7509	1,28
	FZ	2	5,97	4,06	24,2	5	0,8776	1,69
		3	5,95	4,08	24,2	6	0,8733	1,833
		7	5,96	4,11	24,4	4	0,8026	1,55

		8	5,97	4,13	24,6	3	0,7987	1,41
		12	5,96	4,06	24,1	0	0,8125	1
		13	5,96	4,14	24,6	0	0,7273	1
		30	5,96	4,04	24,0	3	0,7453	1,42
		31	5,96	3,85	22,9	3	0,7821	1,44
		35	5,97	4,04	24,1	4	0,6667	1,57
		36	5,97	4,07	24,2	3	0,6617	1,42
		39	5,96	4,07	24,2	3	0,6617	1,42
		40	5,96	4,12	24,5	3	0,6537	1,42

Table 8.38:Charpy test specimens codes and geometrical measures.

		n	**CODE**	**W [mm]**	**T [mm]**	**AREA [mm^2]**
CHARPY	**BMT**	1	11	9,93	2,54	25,222
		2	12	10,11	2,63	26,589
		3	13	9,96	2,56	25,497
	BML	4	14	10,05	2,44	24,522
		5	15	10,02	2,51	25,150
		6	16	10,01	2,55	25,525
	HAZT	7	15,9	10,08	2,6	26,208
		8	15.10	10,04	2,54	25,501
		9	18	9,92	2,6	25,792
	HAZL	10	3	10,14	2,58	26,161
		11	4	9,99	2,55	25,474
		12	7	10,09	2,5	25,225
		13	8	9,91	2,58	25,567
	FZT	14	15,7	9,82	2,58	25,335
		15	15,8	10	2,53	25,300
		16	17	10,14	2,51	25,451
	FZL	17	2	10,01	2,58	25,825
		18	6	9,98	2,56	25,548
		19	10	10,09	2,64	26,637

Table 8.39: Ratio between the area covered by pores and the total area of fused zone.

	A	%
$Area_{PORES}$ [μm^2]	355.187	0,47
$Area_{tot}$ [μm^2]	75.953.184	100
$Area_{tot}$[mm^2]	75,95318389	100

Additional fracture surface images

Tensile test specimens

Heat affected zone machined

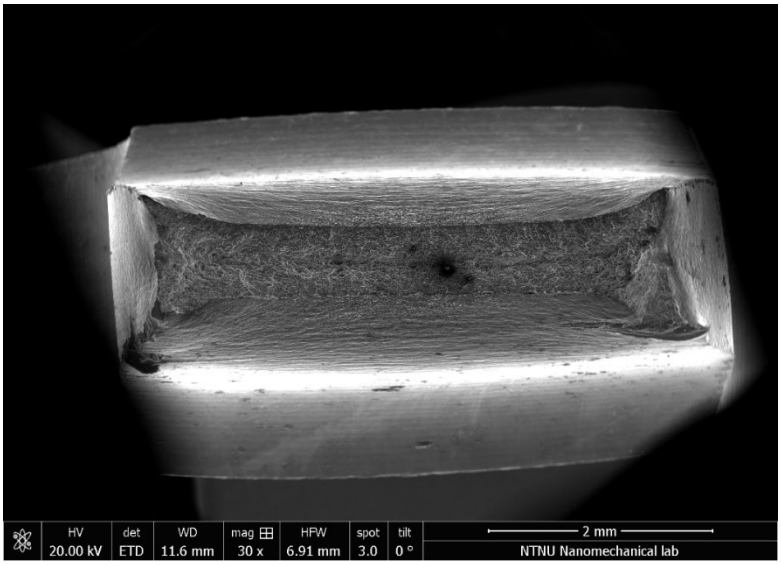

Figure 8.4:Additional SEM image of the fracture surfaces at low magnification for a selected tensile test specimen. Specimen code: 15.3. Magnification 30x.

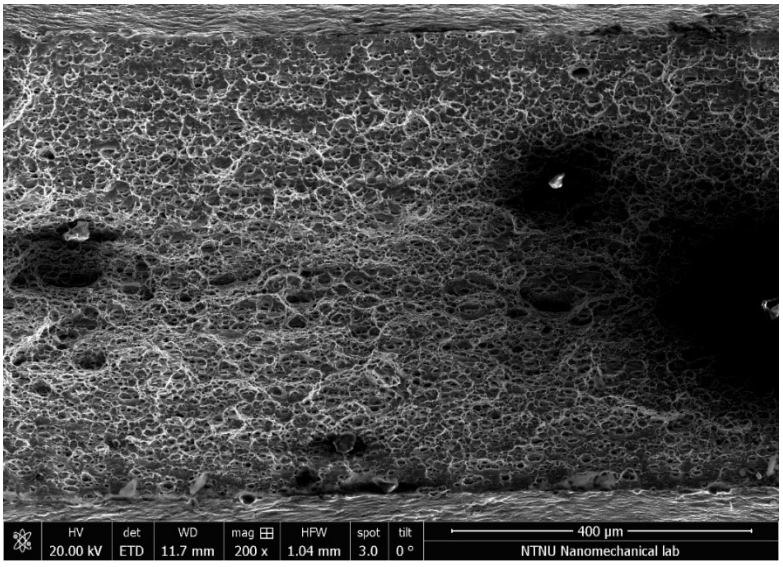

Figure 8.5: Additional SEM image of the fracture surfaces at low magnification for a selected tensile test specimen. Specimen code: 15.3. Magnification 200x.

.

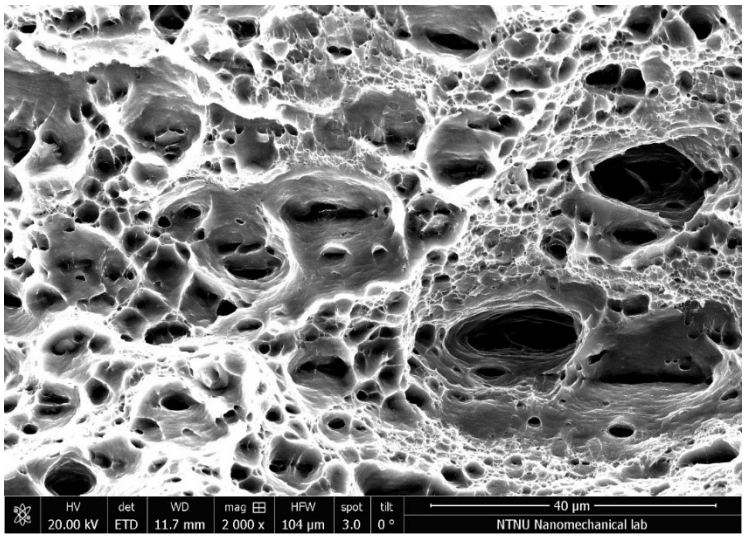

Figure 8.6: Additional SEM image of the fracture surfaces at low magnification for a selected tensile test specimen. Specimen code: 15.3. Magnification 2000x.

Parent material transverse

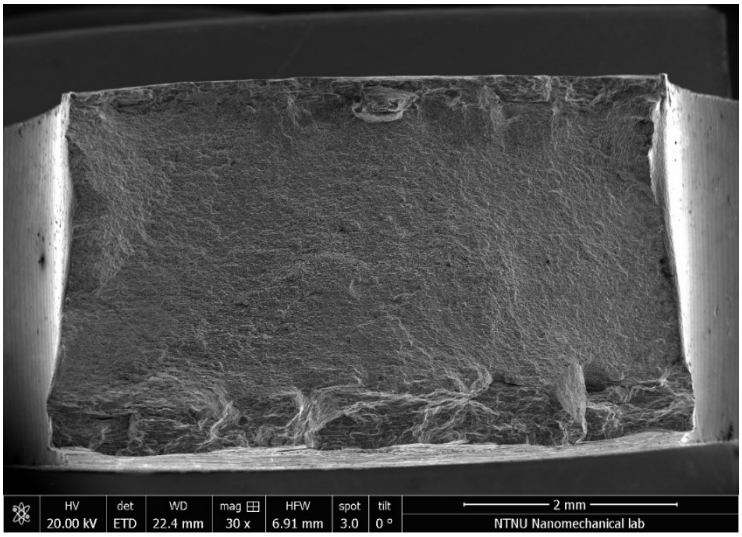

Figure 8.7:Additional SEM image of the fracture surfaces at low magnification for a selected tensile test specimen. Specimen code: BMT5. Magnification 30x.

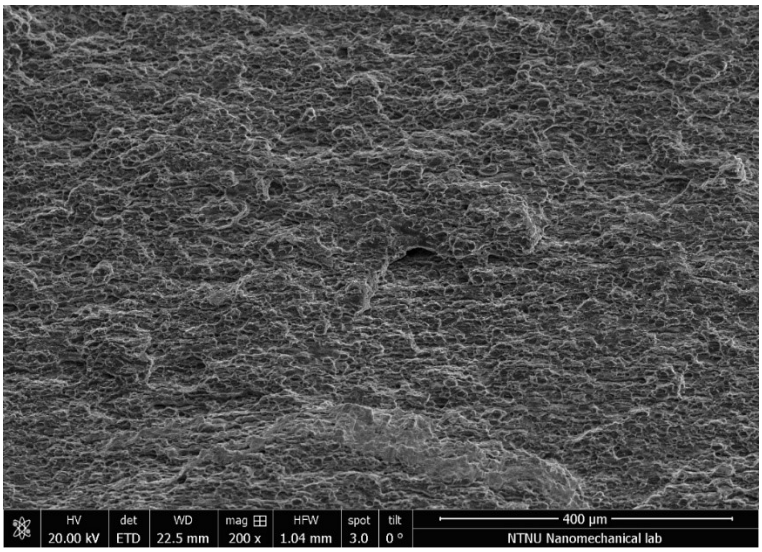

Figure 8.8:Additional SEM image of the fracture surfaces at low magnification for a selected tensile test specimen. Specimen code: BMT5. Magnification 200x.

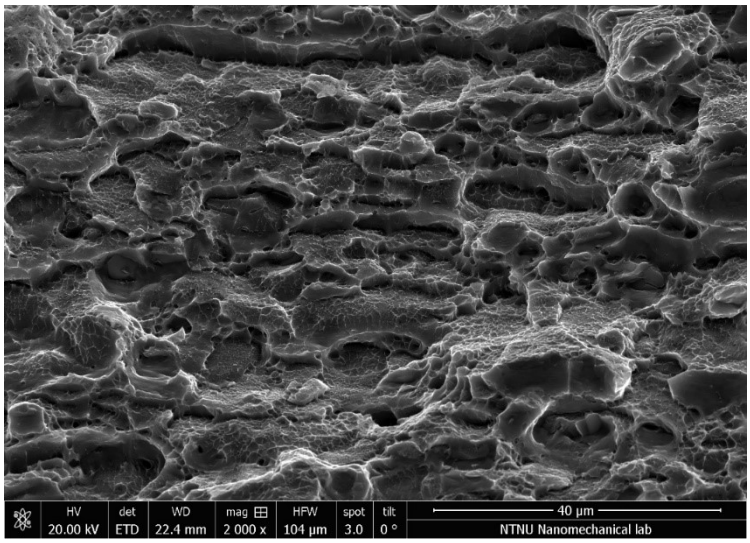

Figure 8.9: Additional SEM image of the fracture surfaces at low magnification for a selected tensile test specimen. Specimen code: BMT5. Magnification 2000x.

Heat affected zone

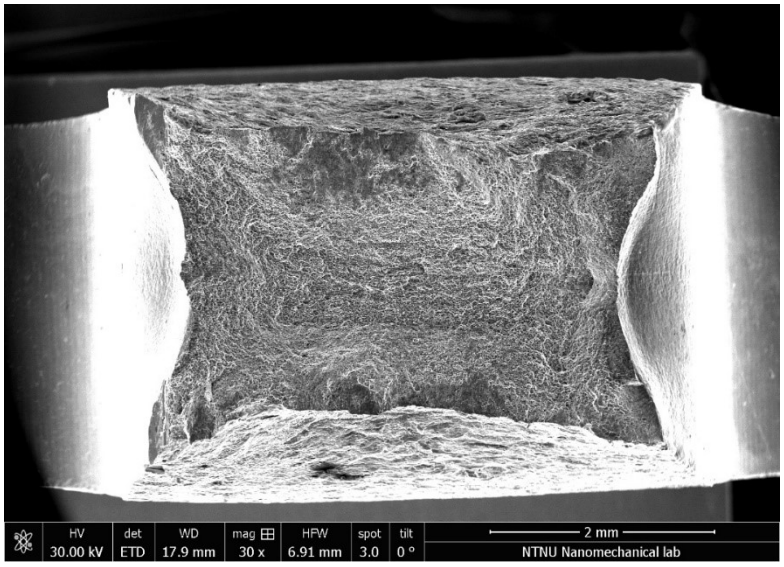

Figure 8.10: Additional SEM image of the fracture surfaces at low magnification for a selected tensile test specimen. Specimen code: FZ25. Magnification 30x.

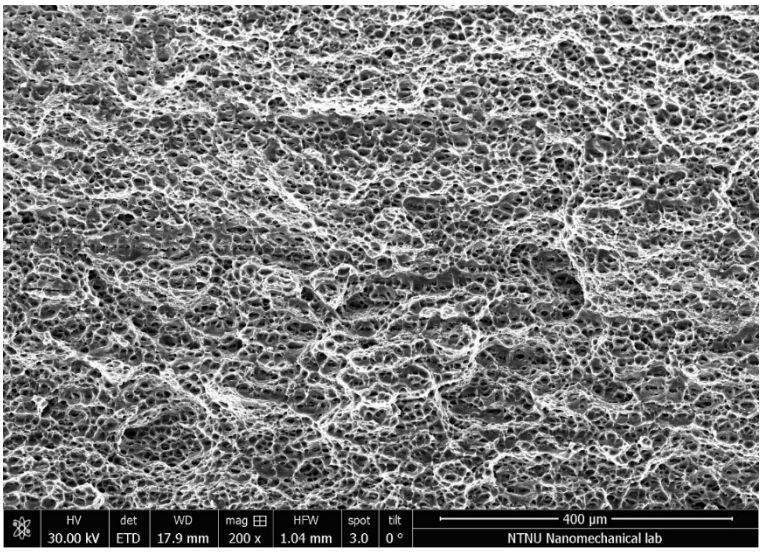

Figure 8.11: Additional SEM image of the fracture surfaces at low magnification for a selected tensile test specimen. Specimen code: FZ25. Magnification 200x.

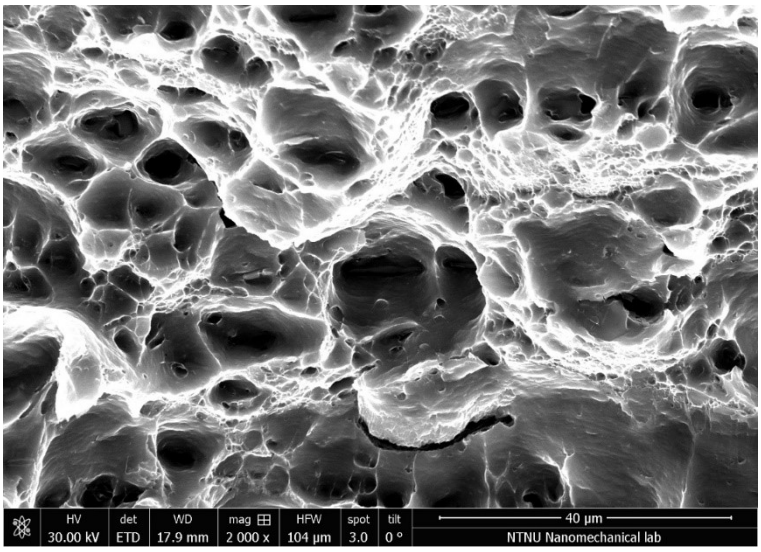

Figure 8.12: Additional SEM image of the fracture surfaces at low magnification for a selected tensile test specimen. Specimen code: FZ25. Magnification 2000x.

Fused zone longitudinal

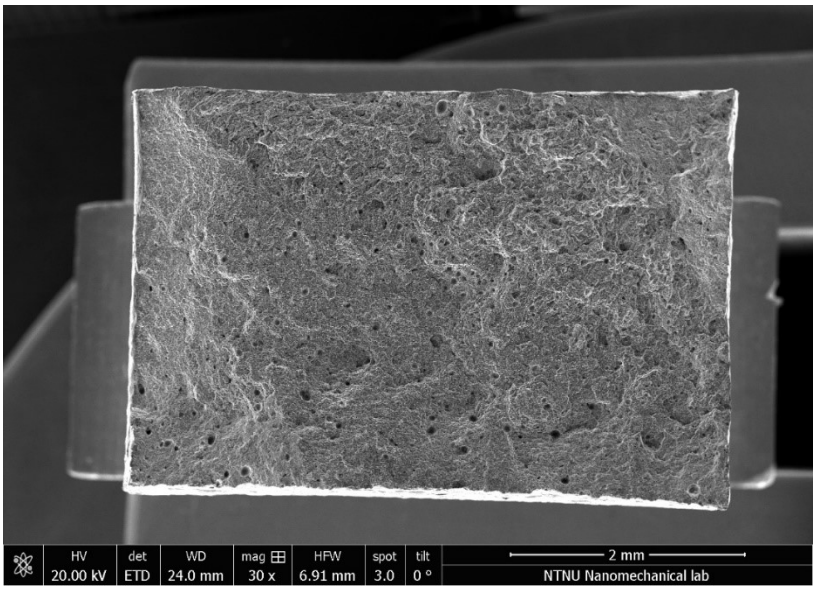

Figure 8.13: Additional SEM image of the fracture surfaces at low magnification for a selected tensile test specimen. Specimen code: FZL9. Magnification 30x.

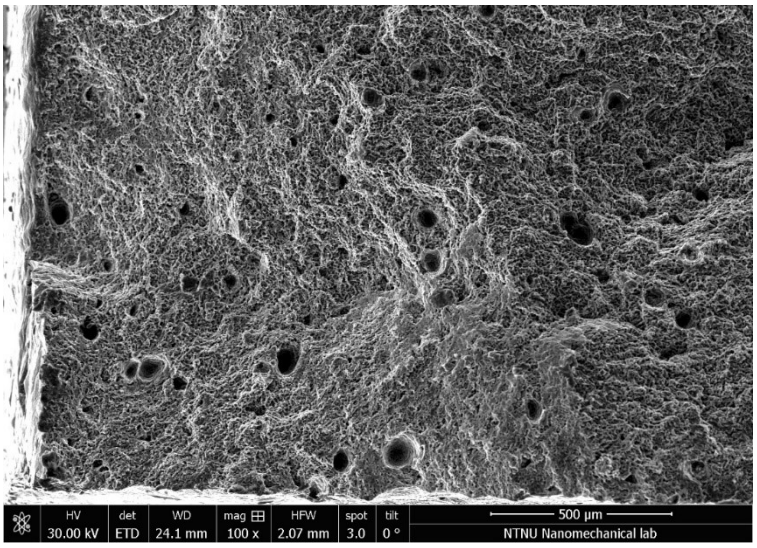

Figure 8.14: Additional SEM image of the fracture surfaces at low magnification for a selected tensile test specimen. Specimen code: FZL9. Magnification 100x.

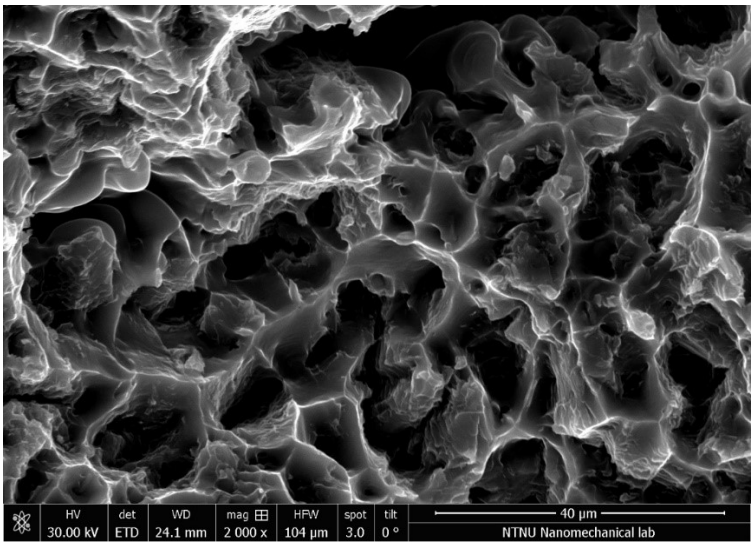

Figure 8.15: Additional SEM image of the fracture surfaces at low magnification for a selected tensile test specimen. Specimen code: FZL9. Magnification 2000x.

FATIGUE

Parent material

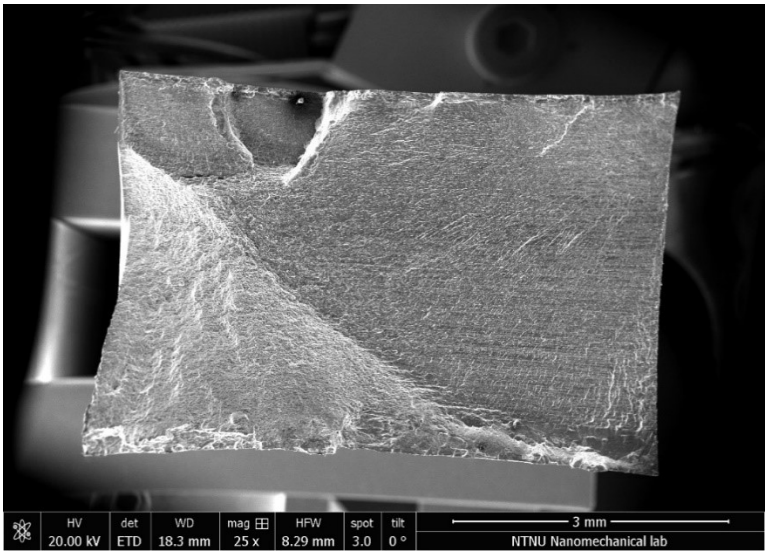

Figure 8.16: Additional SEM image of the fracture surfaces at low magnification for a selected fatigue test specimen. Specimen code: BMT26. Magnification 25x. Zone: overview.

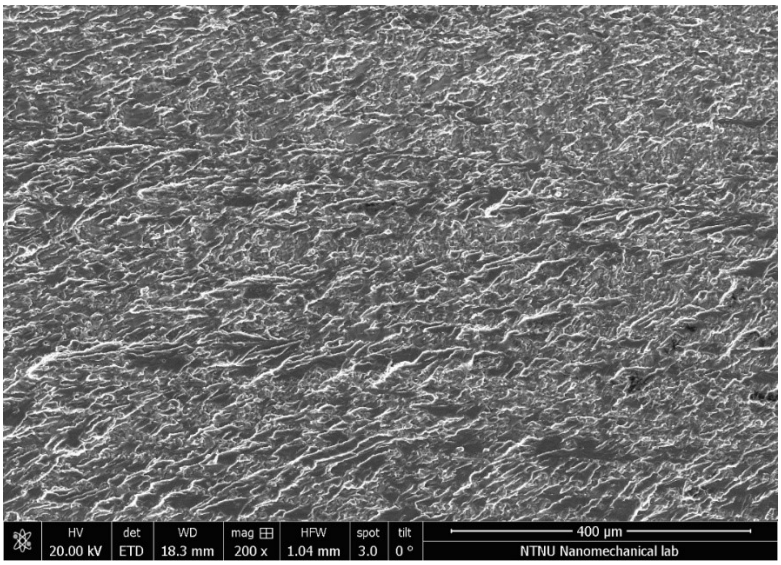

Figure 8.17: Additional SEM image of the fracture surfaces at low magnification for a selected fatigue test specimen. Specimen code: BMT26. Magnification 200x. Zone: crack propagation.

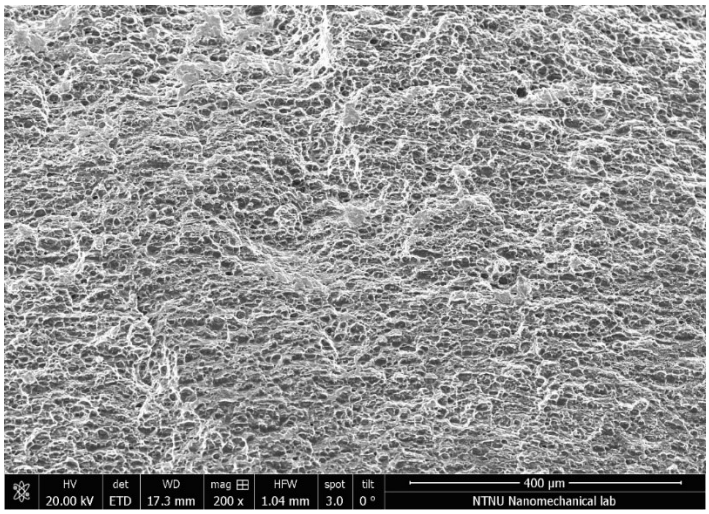

Figure 8.18: Additional SEM image of the fracture surfaces at low magnification for a selected fatigue test specimen. Specimen code: BMT26. Magnification 200x. Zone: final rupture.

Welded specimen

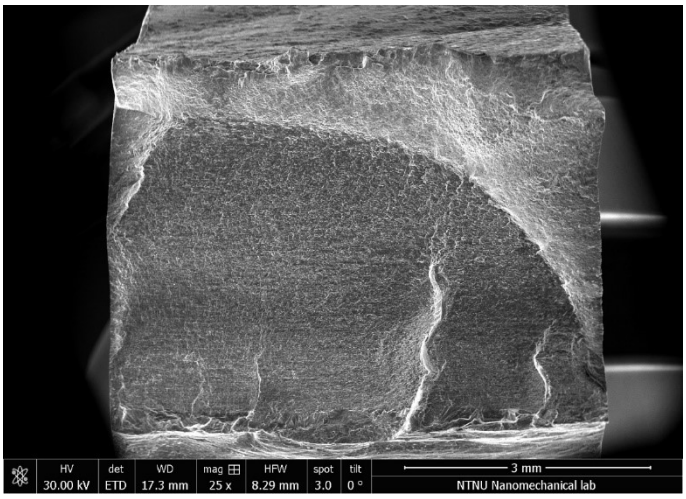

Figure 8.19: Additional SEM image of the fracture surfaces at low magnification for a selected fatigue test specimen. Specimen code: FZ35. Magnification 25x. Zone: Overview.

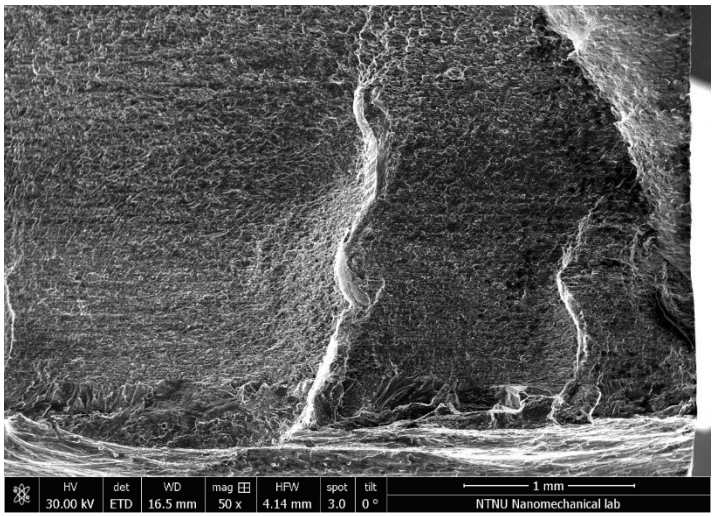

Figure 8.20Additional SEM image of the fracture surfaces at low magnification for a selected fatigue test specimen. Specimen code: FZ35. Magnification 50x. Zone: crack propagation.